



UNIVERSITÀ DEGLI STUDI DI MILANO

Facoltà di Scienze Matematiche, Fisiche e Naturali

Laurea Magistrale in Fisica

Structural and Magnetic Properties of *sp*-Hybridized Carbon

Advisor: Dott. Nicola Manini

Co-Advisor: Prof. Giovanni Onida

Ivano Eligio Castelli

Matricola n° 735774

A.A. 2008/2009

Codice PACS: 61.46.w

Structural and Magnetic Properties of sp -Hybridized Carbon

Ivano Eligio Castelli

Dipartimento di Fisica, Università degli Studi di Milano,
Via Celoria 16, 20133 Milano, Italia

April 9, 2010

Abstract

We perform extended calculations of the electronic structure and geometrical optimization of composed carbon structures where carbon acquires its sp (carbynes) or sp^2 (graphene and aromatic components) hybrid character. We evaluate the electronic structure within the Density Functional Theory (DFT) in the Local Spin Density Approximation (LSDA), which provides a reliable estimate of the total adiabatic energy. We minimize the latter to obtain the locally stable structures and binding energies. We also evaluate magnetic structures, and, by density functional perturbation theory, vibrational properties (frequencies plus infrared and Raman intensities). We find that carbyne linear chains bind strongly to graphene and aromatic structures, usually acquiring a markedly polyynic character (large bond length alternation of single-triple bonds).

Advisor: *Dr. Nicola Manini*

Co-Advisor: *Prof. Giovanni Onida*

Contents

Chapter 1. Introduction	7
1.1. Polyynes vs Cumulenes	8
1.2. Different Terminations	11
Chapter 2. The Naphthyl Termination	13
2.1. Structural Properties	14
2.2. Magnetic Properties	18
2.3. Electronic Properties	20
2.4. Vibrational Properties	24
2.4.1. The Even- n Carbynes	24
2.4.2. The Odd- n Carbynes	31
Chapter 3. The Graphene Termination	35
3.1. A Chain on a Complete Layer	35
3.2. The Nanohole	38
3.3. A Carbyne Binding to a Nanohole	40
3.4. Magnetic Properties	45
3.5. Electronic Properties	54
3.6. Vibrational Properties	57
Chapter 4. Discussion and Conclusions	63
Appendix A. Theory and Implementation	65
A.1. The Density Functional Theory	65
A.1.1. The Hohenberg-Kohn Theorem	65
A.1.2. The Kohn-Sham Equations	65
A.1.3. The Local Density Approximation	68
A.1.4. The Local Spin Density Approximation	68
A.1.5. The Plane-Wave Basis Set	69
A.1.6. The Pseudopotentials	70
A.1.7. The Success and Failures of DFT	70
A.2. The Application of DFT in the Present Work	71
A.2.1. The Naphthyl Termination	72

A.2.2. The Graphene Termination	72
Appendix B. The Magnetization of Carbynes with Other Terminations	77
Bibliography	83
Ringraziamenti	85

CHAPTER 1

Introduction

The rich chemistry of carbon may be interpreted as being due to carbon's capability of adjusting its electronic configuration to different bonding situation. This ability arises from the comparably small energy difference of atomic $2s$ and $2p$ functions (8.2 eV in density-functional calculations, 7.1 eV from the NIST Atomic Spectra Database [1]). The element carbon can realize three main hybridization schemes of the valence atomic orbitals: sp^3 , sp^2 , and sp hybridization. Three-dimensional carbon networks due to the sp^3 bonding form diamond and related amorphous structures. Two-dimensional networks are due to the sp^2 hybridized orbitals and form graphite, graphene, and its amorphous counterpart. sp hybridized atomic orbitals form linear chains, discovered in nature as late as in 1968 [2], called *carbynes*. Carbynes are interesting not only for their properties, but also for the fact that in the phase diagram of carbon, their field of existence coincide with that of fullerenes [3]. Indeed, carbynes are part of the clouds present in interstellar regions of space together with fullerenes [4, 5], amorphous carbon dust, cyanopolyynes, and oligopolyynes. These clouds were formed with the explosions of carbon stars, novae and supernovae.

In the labs, one of the methods for the synthesis of a mixture of carbynes of different lengths is using an electric arc between graphite electrodes [6]. That is also one of the methods for the bulk production of fullerenes and carbon nanotubes. By an electric arc between two graphite electrodes submerged in a solvent like decalin or acetonitrile, one can produce a range of even-length carbon chains (4 to 16 atoms), terminated by one hydrogen at each end. Such solution is stable in air over a week time scale. Jin *et al.* [7], have introduced a new approach to realize carbon chains by stretching and thinning a graphene nanoribbon from its two open ends by removing carbon rows until the number of rows becomes one or two. These chains show a good stability under Transmission Electron Microscopy (TEM) and lengths up to few nanometers. Matsuda *et al.* [8] and Kudryavtsev [9] have shown the possibility of synthesizing carbyne by oxidative dehydropolycondensation of acetylene: carbyne powder was obtained by passing acetylene through an aqueous ammoniacal solution of a copper salt. Cataldo and Capitani [10], have revealed that the carbonaceous matter obtained is rich in carbynoid structures but also consist of sp^2 - and sp^3 -carbon atoms. Polyynes in solution generated by laser ablation of graphite or fullerenes particles suspended in an organic solvent, was the method used by Tsuji [11]. Carbyne can be produced from carbon by dynamic pressure (Yamada *et al.* [12], Kleiman *et al.* [13]): the method was

based on the pressure-temperature phase and transformation diagram of carbon; the critical point, which has been estimated for transformations from graphite to other solid phases (carbyne), is 0.2 GPa/6800 K [3]. Ravagnan *et al.*, have shown the possibility of growing a pure carbon amorphous solid containing a significant amount of carbynoid structures (sp^2 and sp hybridized) by supersonic carbon cluster beam deposition at room temperature and in an ultra-high vacuum [14]. Carbon film with carbynoid structures were synthesized by Donnet *et al.* [15] by a combustion reaction between oxygen and acetylene. Kavan [13] and Kijima *et al.* [16] have used the electro-chemical method to synthesize carbyne: the charge transfer reaction occurs at interface of a metal electrode and liquid electrolyte solution. The advantage of this technique is the synthesis of a carbyne at room temperature. Carbyne or carbynoid material resulting from the synthesis contained up to 300 carbon atoms, so this technique is a promising strategy towards molecular engineering of sp -carbon structures. Examples of this method are Ohmura *et al.* [17], oxidized acetylene in dimethylformamide electrolyte solution containing CuCl catalyst, and Kijima *et al.* [18], reduced diiodoacetylide to carbon at a platinum electrode in dimethylformamide media. This method has been used by F. Cataldo to synthesize the molecule analyzed in Chap. 2.

Ab-initio methods based on Density-Functional Theory (DFT) are by now common and well established tools for studying structural and vibrational properties of materials on realistic grounds. The plane-wave pseudopotential method and the Local Spin-Density Approximation (LSDA) to DFT have provided a simple framework whose accuracy have been demonstrated in a variety of systems [19]. The computational methods used in the present work are described in Appendix A.

1.1. Polyynes vs Cumulene

We can recognize two different limiting structures of carbynes: chain of alternate single and triple bonds ($[-C \equiv C - C \equiv C-]_m$) called *polyynes* or α -carbyne, contrasted to an equally-spaced based on carbon-carbon double bonds ($[=C=C=C=C=]_m$) called *cumulene* or β -carbyne. Typical bond lengths are 138, 129, and 123 pm for single, double, and triple bonds, respectively [13]. A simple quantity to characterize the degree of polyynicity of the chain is the Bond-Length Alternation (BLA). The BLA measures the degree of dimerization and, excluding terminal bonds, can be defined as:

$$(1) \quad BLA = \frac{1}{2} \left[\sum_{j=1}^{n_e} d_{2j-1} + d_{n-(2j-1)} / n_e - \sum_{j=1}^{n_o} d_{2j} + d_{n-2j} / n_o \right],$$

with $d_i = |\vec{r}_i - \vec{r}_{i+1}|$, $n_e = (n + 2) / 4$, and $n_o = n / 4$ (integer part). Figure 1.1 shows the difference between the all-equal bonds b_0 of the cumulenic chain (in red) and the alternation of single and triple bonds (b_1 and b_3 , respectively) of the polyynic chain. The BLA is twice the difference between b_1 and b_0 . Panels (a) and (b) of Fig. 1.2 display the total energy per atom for an infinite linear carbon chain as a function of the average C - C bond length. For

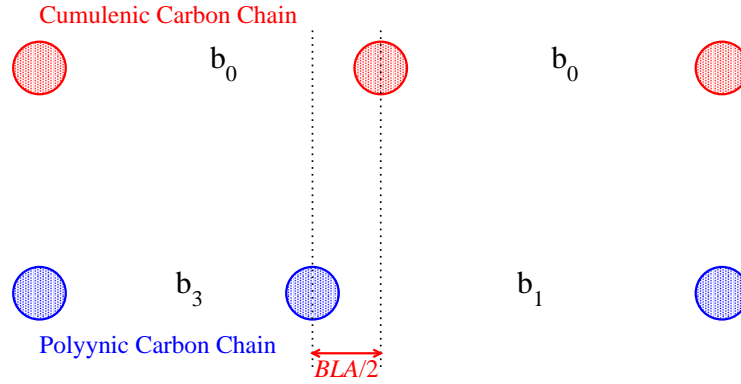


Figure 1.1: In a cumulenic chain (in red) the distances between atoms are all equal (b_0); in a polyynic one (in blue) the distances are different ($b_1 \neq b_3$) for single/triple bonds. The BLA, defined in Eq. 1, measures the degree of dimerization.

the cumulenic chain, we consider a unit cell with one carbon atom and for each value of the cell length, we realize a self-consistent evaluation of the DFT-LSDA total energy; for the polyynic chain, we consider a unit cell composed of two atoms and relax the atomic positions for each cell size. Within DFT-LSDA the minimum of the total energy is obtained for the a chain with a polyynic character ($BLA \simeq 7$ pm): the difference in binding energy between the two types of chains is small, less than 0.1% for $\overline{C-C} \leq 130$ pm, where the difference between the two bonds is lower than 7 pm; the BLA increases for $\overline{C-C} > 130$ pm, where the most stable configuration is the polyynic chain. A BLA equals to 5.5 pm is obtained making a relaxing calculation in which we also relax the dimension of the cell along the chain axis besides the atomic positions. As shown in Fig. 1.2(c), when $\overline{C-C} > 130$ pm the length of the triple bond stabilizes near 130 pm while the length of the other (the single bond) increases with increasing unit cell. Figure 1.3(a) shows the binding energy per atom for a linear polyynic chain with a unit-cell kept fixed at 260 pm (the cell that shows the minimum value of the total energy in Fig. 1.2) as a function of the BLA (in pm). We consider structures with two atoms per unit cell and gradually move every second atom away from midpoint of the cell. The total energy varies very little upon the bond-length difference and the most stable configuration has a BLA $\simeq 7$ pm; in respect to the value obtained by M. Springborg reported in Ref. [13], our BLA is lower: in fact their calculations suggest that the most

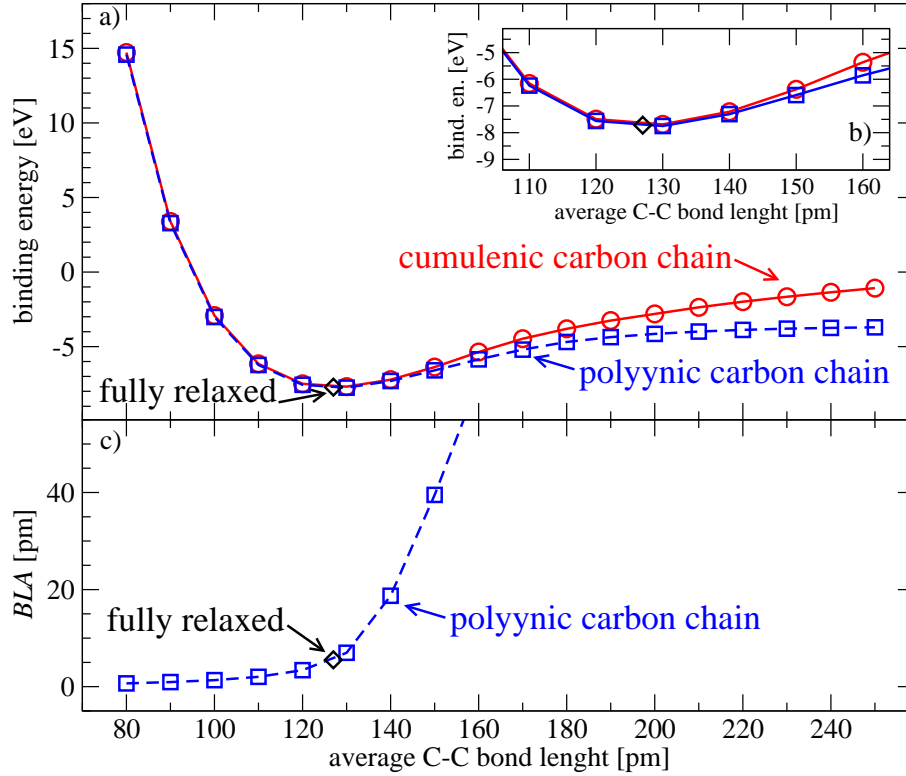


Figure 1.2: Panel (a): Binding energy per atom for an infinite cumulenic chain (in solid red) and for an infinite polyynic chain (in dashed blue) as a function of the mean C – C bond length $\overline{C-C}$. Fully relaxed (in black) indicates the binding energy obtained for a relaxing calculation in which we also relax the cell that contains the chain. Inset (b): Enlargement of panel (a) near the region of minimum energy. Panel (c): BLA value for an infinite polyynic chain as a function of $\overline{C-C}$: for a value of $\overline{C-C}$ lower or equal than 110 pm the BLA is very small ($BLA < 2$ pm, i.e. the chain exhibits a cumulenic character); for $\overline{C-C}$ greater than 110 pm the BLA increases linearly with $\overline{C-C}$ (i.e. the chain becomes more and more dimerized with the alternation single/triple bonds, typical of the polyynic chain).

stable configuration has a $BLA \simeq 15$. Despite this fact our calculations are in accordance with what was predicted by Peierls [20]: the most stable configuration has a polyynic character. But in accordance with the Peierls' distortion, it should display clearly the lower energy for a chain with polyynic character and not as it happens in our calculations, where the energy difference between the two types is not significant. In the fully relaxing calculation (black

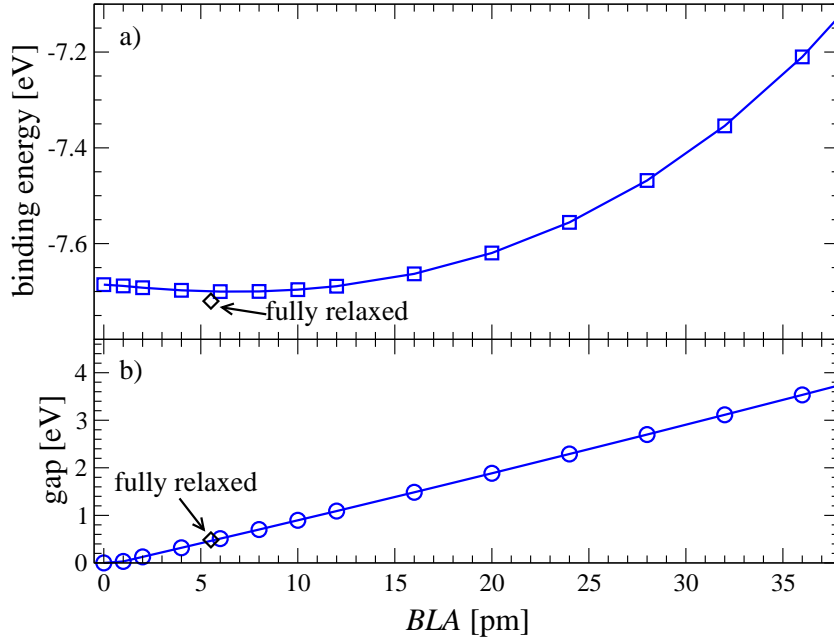


Figure 1.3: Binding energy per carbon atom (a) and energy gap (b) as a function of the BLA (in pm) for an infinite polyynes with a unit cell of 260 pm with 2 atoms per cell. The black diamond indicates the value of the binding energy or that of the energy gap obtained making a fully relaxing calculation, in which we also relax the dimension of the cell along the chain axis.

diamond) in which we relax both the positions of the carbon atoms and the size of the cell, the BLA equals 5.5 pm.

The non-zero BLA is accompanied by the opening of a gap at the Fermi level, as shown in Fig. 1.3(b): for a BLA $\simeq 6$ pm, the chain shows a gap of about 0.7 eV. Figure 1.4 [13] shows the electronic orbitals that split into two energetically deep-lying σ bands and into two π bands around the Fermi level; the π bands of the cumulenic chain cross at Fermi level ϵ_F , so that the chain has a 1D metallic behavior, while the corresponding bands of the polyynic chain show a gap of about 2 eV so that the carbyne behaves as a semiconductor.

1.2. Different Terminations

As shown by Ravagnan *et al.* [21], the structural vibrational and electronic properties of carbon chains are affected by the nature and geometry in the terminations. Weimer *et al.* [22] analyze how end groups and bond lengths influence the gap between the highest occupied and the lowest unoccupied molecular orbital (HOMO and LUMO respectively):

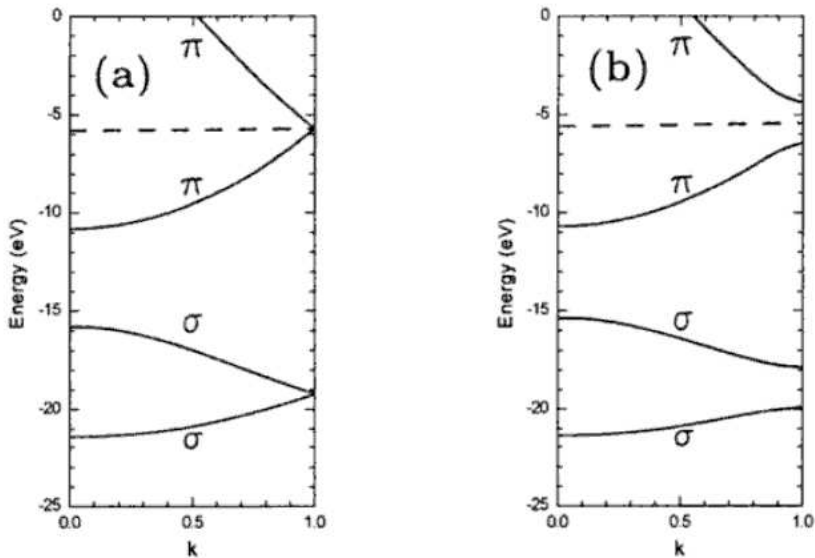


Figure 1.4: Band structures for an infinite carbyne for a structure with (a) constant and (b) alternating bond length. The values $k = 0$ and $k = 1$ correspond to the center and the edge of the Brillouin zone for a 1D repeated cell containing two atoms, respectively. The dashed line marks the Fermi level [13]. A gap of about 2 eV opens in the π bands of the polyynic chain.

for short chains ($n = 4$) the gaps of carbines with different single-bonds end groups (such as CN, F, NH_2 , and NO_2) ranges between 2.4 and 5.7 eV. In long chains ($n = 28$) the gap decreases to 0.7 and 1.6 eV. Kijima *et al.* in Ref. [15], studied synthesis, properties, and possible applications of polyynes with different ligands.

In the present thesis, motivated by experimental work carried out at our Department, we consider carbon chains in two main different binding environments for carbynes: (i) gas-phase molecules composed by linear chains terminated by a naphthalene group at each end (Chap. 2); (ii) carbynes bound to a hole in a infinite graphene sheet (Chap. 3).

CHAPTER 2

The Naphthyl Termination

In this chapter, we investigate structural, vibrational, and electronic properties of *carbynes* terminated with two naphthyl groups, called **dinaphthyl-carbyne**. This class of molecule was first synthesized by F. Cataldo using the Cadiot-Chodkiewicz reaction [23] in which two copper naphthyl-acetylide bind to one or more diiodoacetylene, as shown in Fig. 2.1.

Due to the synthesizing process, the resulting carbon chains is composed by an even- n number of atoms. Using High Pressure Liquid Chromatography (HPLC), F. Cataldo was able to estimate the relative molar concentration of the dinaphthyl-polyynes with different

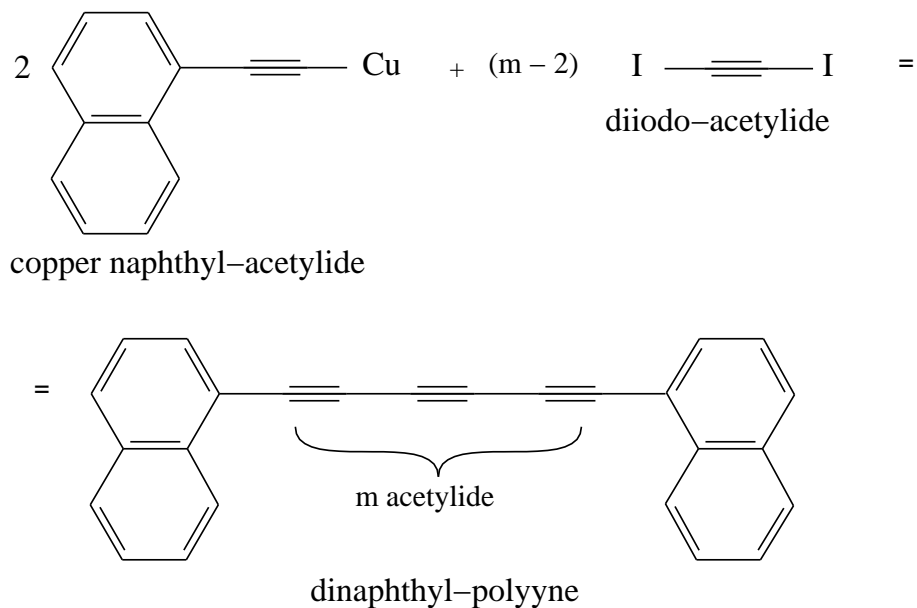


Figure 2.1: Chemical structure of the Cadiot-Chodkiewicz reaction used to produce a dinaphthyl-polyyne: 2 copper naphthyl-acetylide react with $m - 2$ diiodoacetylides with the result of a dinaphthyl-polyyne molecule composed of m acetylide groups.

Chemical formula	Concentration [mol]
NaphC ₂ H	39.5%
Naph ₂ C ₄	22.9%
Naph ₂ C ₆	25.9%
Naph ₂ C ₈	9.1%
Naph ₂ C ₁₀	2.4%
Naph ₂ C ₁₂	0.1%
Naph ₂ C ₁₄	<i>trace</i>
Naph ₂ C ₁₆	<i>trace</i>

Table 2.1: Relative molar concentration of the dinaphthyl-polyynes as a function of the atoms that forms the carbyne obtained by F. Cataldo, in Ref. [24], using HPLC.

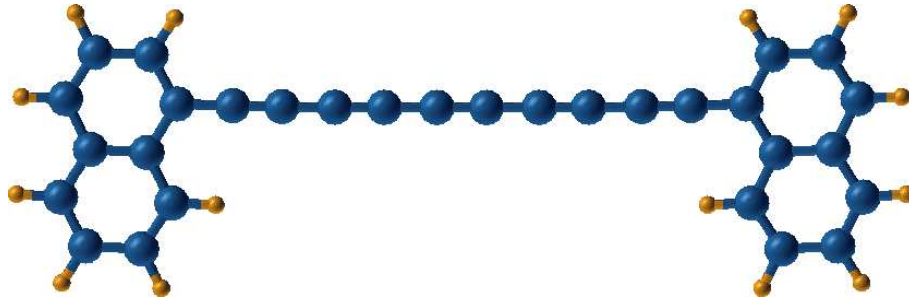
length (i.e. as a function of the atoms that forms the carbyne), as reported in Table 2.1. The symbol Naph₂C_{*n*} is a shorthand for a dinaphthyl-polyyne with a carbyne of *n* atoms.

In our simulations, we consider molecules containing C_{*n*} chains with both even and odd *n*, ranging from 4 to 16. The computational details are described in Appendix A.2.1.

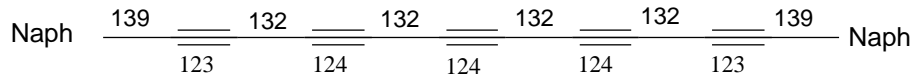
2.1. Structural Properties

Our initial computational investigation focuses on the even-*n* carbon chains, for which experimental data are obtained in our laboratory, using the samples synthesized by F. Cataldo. Using structural optimization, we first of all compute fully relaxed molecular structures. An example is shown in Fig. 2.2. Figure 2.2(b) reports the chemical structure of Naph₂C₁₀ with the final relaxed bond lengths of the polyyne part: triple bonds are visibly shorter than single bonds. Indeed, the single bond to the naphthyl group induces a dimerization very much alike to the one that a termination with hydrogen would induce. Each atom of the carbynic chain is *sp*-hybridized and carries two unhybridized *p* orbitals perpendicular to the chain axis, plus two *sp*-hybrid orbitals aligned along the chain axis. The overlap of *sp* orbital from each atom forms one *sp* – *sp* σ bond. The remaining *p_x* and *p_y* orbitals can combine with the respective *p_x* and *p_y* orbitals of either the same on both adjacent atoms forming two π bonds. In the first case, the one representing the polyynic compounds, the bonds are alternately single and triple and the structure is dimerized. In the opposite case, realized in e.g. CH₂-C_{*n*}-CH₂ cumulenes, the bonds are all double and the BLA is minimal.

The BLA, evaluated for the relaxed geometry of each compound according to Eq. (1), decreases slightly as the chain length increases, as shown in Fig. 2.3. The BLA of long carbynes tends to approach a value of $\simeq 6$ pm. The BLA evolves from 12 to 7 pm showing



(a) Molecular structure



(b) Chemical structure

Figure 2.2: Fully relaxed molecular structure (a) and chemical formula (b), with bond lengths in pm, of a 10-atom sp -bonded carbon chain terminated on sp^2 polycyclic hydrocarbon (naphthyl group). Carbon atoms are in blue, hydrogen ones in yellow. The exact chemical name of the molecule is 1,10-(1,1') dinaphthyl-decapentayne.

Chemical formula	C-C Bond Lengths [pm]									BLA [pm]
	BL0	BL1	BL2	BL3	BL4	BL5	BL6	BL7	BL8	
Naph ₂ C ₄	140	122	134							11.4
Naph ₂ C ₆	139	123	133	123						10.0
Naph ₂ C ₈	139	123	133	124	132					9.1
Naph ₂ C ₁₀	139	123	132	124	132	124				8.3
Naph ₂ C ₁₂	139	123	132	124	131	124	131			7.8
Naph ₂ C ₁₄	139	123	132	124	131	124	131	125		7.5
Naph ₂ C ₁₆	139	123	132	124	131	124	131	125	131	7.1

Table 2.2: C-C bond lengths of the first half of the chain (the second half can be reconstructed using symmetry) and BLA both in pm for the even- n chains. The bond length between the terminations and the chain is not influenced by the length of the carbyne; the polyyne character of the carbyne is marked by the values of BLA and by the alternation in bonds length. The character becomes more cumulenic with the increasing of the length of chain.

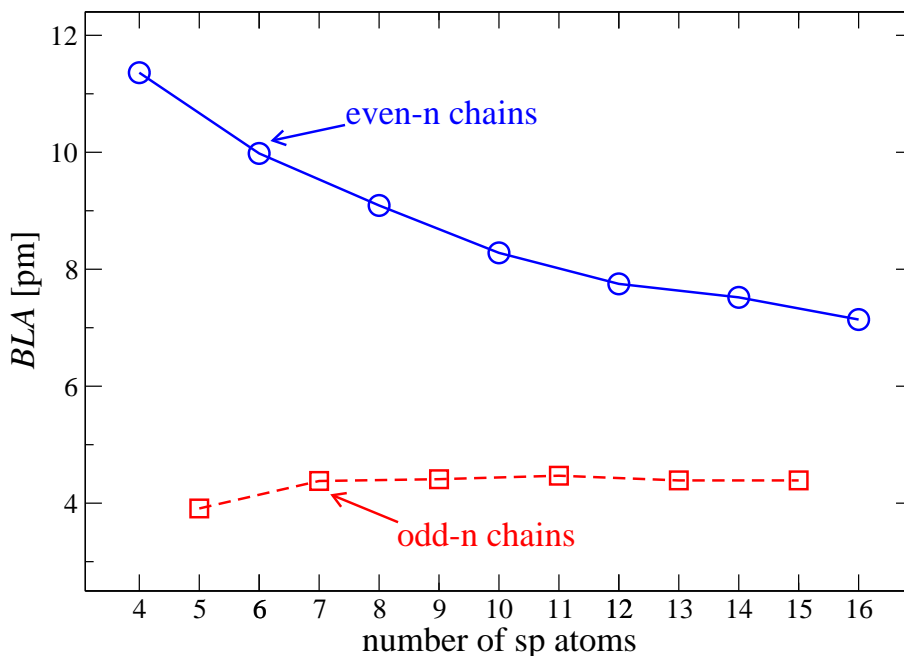
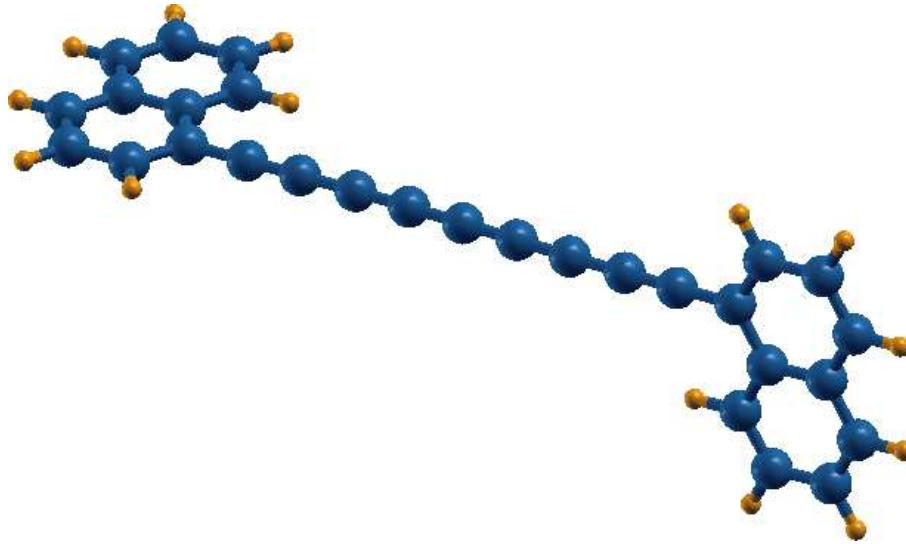


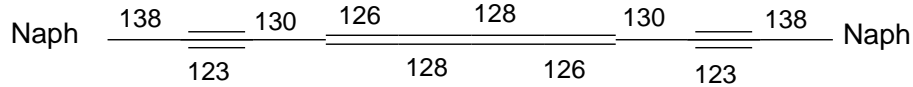
Figure 2.3: Bond-length alternation (BLA) as a function of the number n of atoms in the carbynic chain Naph-C $_n$ -Naph for the even- n chains (in solid blue) and for the odd- n chains (in dashed red).

a polyynic behavior (more evident for the short chains) despite the chains being bonded to sp^2 sites: comparing this BLA with the one computed for the different chains, investigated in Ref. [21], dinaphthyl-polyynes have a BLA closer to the sp^3 terminated chains (e.g. -H or -C $_{20}$ terminated) than to sp^2 terminated ones (-CH $_2$ or graphene terminated ones).

The length of the bond between the first atom of the sp chain and the C atom of the terminating group (BL0 \simeq 139 pm) reported in Table 2.2, appears only weakly affected by the chain length and is determined primarily by the typology of the ligand. The longer is this first C-ligand bond, the more polyynic is the ensuing chain character; in fact, the length of the first bond relates to bond order of the C-ligand bond: the two extreme cases are -CH $_2$ terminated chains (double bond, of length 126 pm) and -C $_{20}$ terminations (with a purely σ bond of length equal to 142 pm). C-graphene bonds are examples of intermediate bond order, with the π bond only partially populated, and as a consequence intermediate bond length. BL0 is then an indicator of what fraction of π electron the terminating C-ligand bond devotes to this terminal bond, rather than to the polyyne. This fraction is essentially 0% for -C $_{20}$ and practically 100% for -CH $_2$ terminations). This quantity, appearing almost independent from the chain length, is then the main parameter that determines the properties of the even- n chains.



(a) Molecular structure



(b) Chemical structure

Figure 2.4: Molecular (a) and chemical structure (b), with bond lengths in pm, of a 9-atom sp -bonded carbon naphthyl-terminated chain. The total energy is essentially independent of the rotation of one naphthyl group relative to the other one around the chain axis.

The naphthyl termination proves a stable structure, with a gain between 5.5 and 7 eV per bond between the carbyne and the naphthyl group. The end groups are almost completely free to rotate around their axis: for a molecule with one of the naphthalenes rotated by 90° respect to the geometry shown in Fig. 2.2(a), the total energy is only slightly higher (by $\simeq 20$ meV, nearing to the resolution of these DFT calculations) than the total energy computed for the planar molecule. When the naphthyl group is rotated by 180° to the planar configuration, no evidence of variation in total energy is detected. So we can consider the terminations as essentially free to rotate independently around the carbyne axis.

The situation is different in odd- n carbyne: these molecules, at least at the moment, to our knowledge, have not yet been synthesized. BL0 are typical of polyyne chain, like for even chains, but frustration of the single-triple bond alternation reduces drastically the BLA near the middle of the chain where eventually double bonds occur (the C-C bond lengths are reported in Table 2.3). The missing bond alternation at the middle of the chain

Chemical formula	C-C Bond Lengths [pm]								BLA [pm]
	BL0	BL1	BL2	BL3	BL4	BL5	BL6	BL7	
Naph ₂ C ₅	138	125	129						3.9
Naph ₂ C ₇	138	124	130	127					4.3
Naph ₂ C ₉	138	124	130	126	128				4.4
Naph ₂ C ₁₁	138	123	130	126	128	126			4.4
Naph ₂ C ₁₃	139	123	130	125	129	126	128		4.4
Naph ₂ C ₁₅	139	123	131	125	129	126	128	127	4.4

Table 2.3: C-C bond lengths of the first half of the chain (the second half can be reconstructed using symmetry) and BLA both in pm for the odd- n chains. The bond length between the terminations and the chain is not influenced by the length of the carbyne; the polyynic character of the carbyne is marked by the values of BLA and by the alternation in bonds length. The character becomes more cumulenic with the increasing of the length of chain.

leads to a BLA with values more characteristic of a cumulenic chain ($\simeq 4.5$ pm) almost independent of the length of the chain, as shown in Fig. 2.3. Also for the odd- n chains, the naphthyl groups are almost free to rotate: in fact the total energy of the twisted molecule, shown in Fig. 2.4(a), is slightly smaller ($\simeq 10$ meV) than that calculated for the planar molecule. Tables B.1 and B.2 show the comparison of the total energy for planar and twisted configuration of both cumulenic and polyynic chains terminated by $-H$, $-H_2$ and by a phenyl group.

In the next sections, we will investigate electric, magnetic and vibrational properties of even-carbyne planar-molecules and odd-carbyne twisted-ones (in which the two naphthyl groups are rotated by 90° each other); in fact, some tests show us no significant dependence of these physical properties on the orientation of a naphthyl group with respect to the other.

2.2. Magnetic Properties

For each fully relaxed structure, we have carried out LSDA calculations. The magnetic behavior of odd- n chains is quite different with respect to that of even- n chains. All even- n chains remain spin-*unpolarized* in both the planar and the twisted configuration; as remarked above, from the electronic point of view, one could substitute the two naphthyl ligands with two hydrogens with little change in the electronic levels, and indeed the $C_{2m}H_2$ polyynes are not magnetic.

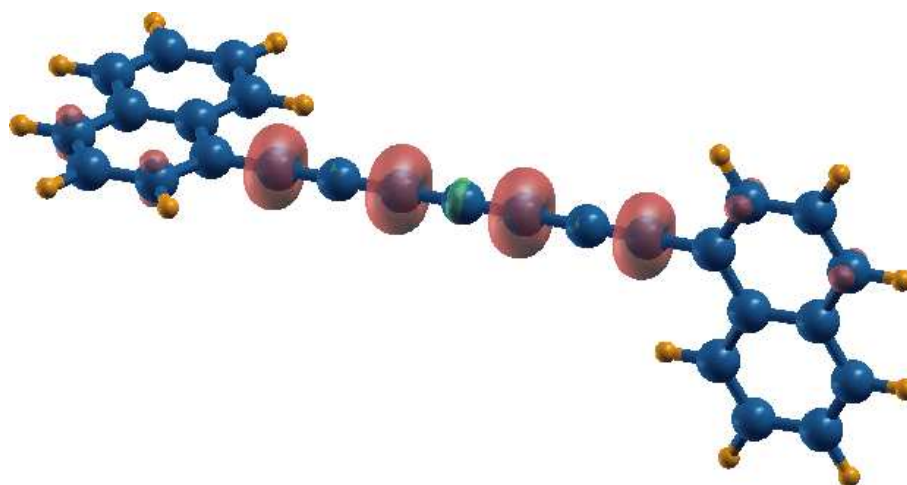
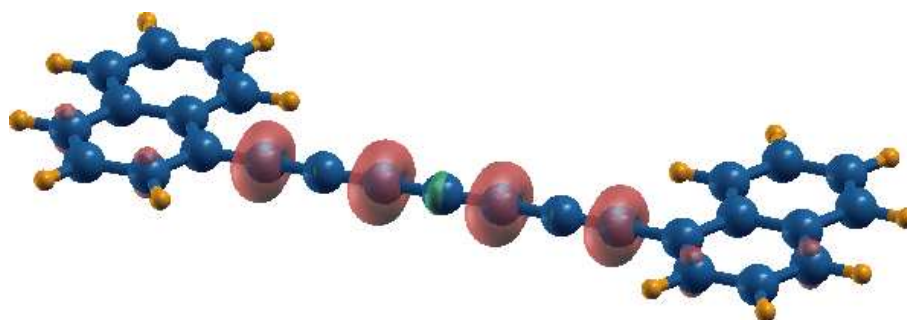
(a) Rotated geometry of Naph_2C_7 (b) Planar configuration of Naph_2C_7

Figure 2.5: Magnetization isosurfaces of Naph_2C_7 with the two naphthalenes rotated by 90° each other (Fig. 2.5(a)) and in planar configuration (Fig. 2.5(b)). The positive magnetization are in red, and the negative component of the magnetization is in green. The total magnetization equals 2 Bohr magnetons, indicating a $S = 1$ state.

On the other hand, odd- n chains are spin-*polarized*, independently of twisting (Fig 2.5); likewise, the $\text{C}_{2m+1}\text{H}_2$ molecules are magnetic. In Appendix B, we report the magnetic properties of even and odd carbynes, planar and twisted, terminated by $-\text{H}$, $-\text{H}_2$, by a phenyl group, and by a phenyl with an extra H atom (protonated phenyl) in order to break the π conjugation. The magnetization is the result of a different electronic structure between even and odd chains: in odd- n chains, two extra majority electrons occupy two more π levels than the minority spin component; this does not occur in even- n chains for which the same number of levels are occupied for both the spins. The total magnetization per

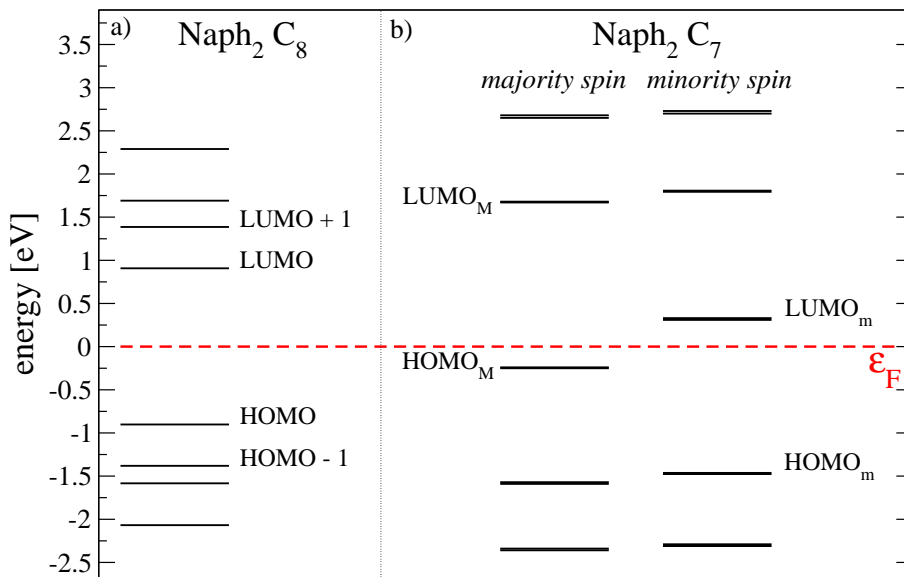


Figure 2.6: Energy levels for the Naph₂C₈ (a) and for the Naph₂C₇ (b) molecule. In the Naph₂C₇, we distinguish between the majority and minority spin (Sect. 2.2). Fermi energy is taken as reference energy (dashed).

molecule equals 2 Bohr magnetons, indicating a $S = 1$ state. Figure 2.5 shows the magnetic isosurface for the two configurations, planar and twisted, of the Naph₂C₇ molecule: the red isosurface marks the positive (majority) magnetization equal to 2.33 Bohr magnetons/ a_0^3 , the green isosurface the negative (minority) value equal to -0.33 Bohr magnetons/ a_0^3 . In all configurations of all considered molecules, a positive magnetization is localized on the odd-atoms of the carbyne, the negative magnetization localizes on the even-atoms.

2.3. Electronic Properties

Figure 2.6 reports the molecular levels of the Naph₂C₈ molecule around the Fermi energy. The evolution of the gap between the lowest unoccupied molecular orbital (LUMO) and the highest occupied molecular orbital (HOMO) is shown in Fig. 2.7: this gap decreases following the increase of the chain length. As shown in Fig. 2.8(a), the gap, in eV, is wider for the even- n carbyne and it is equal to $\simeq 1.5$ eV for the longer chains. In the odd- n chains, the gap is narrower ($\simeq 0.5$ eV almost independently from the length of the chain). The gap of the isolated naphthalene ($\simeq 3.5$ eV) is on the extension of the even- n line due to the stronger overlap between the electron density of the carbyne and of the ligand for the shorter chain with respect to the longer one (Figs. 2.9 and 2.10). Figure 2.8(b) shows the

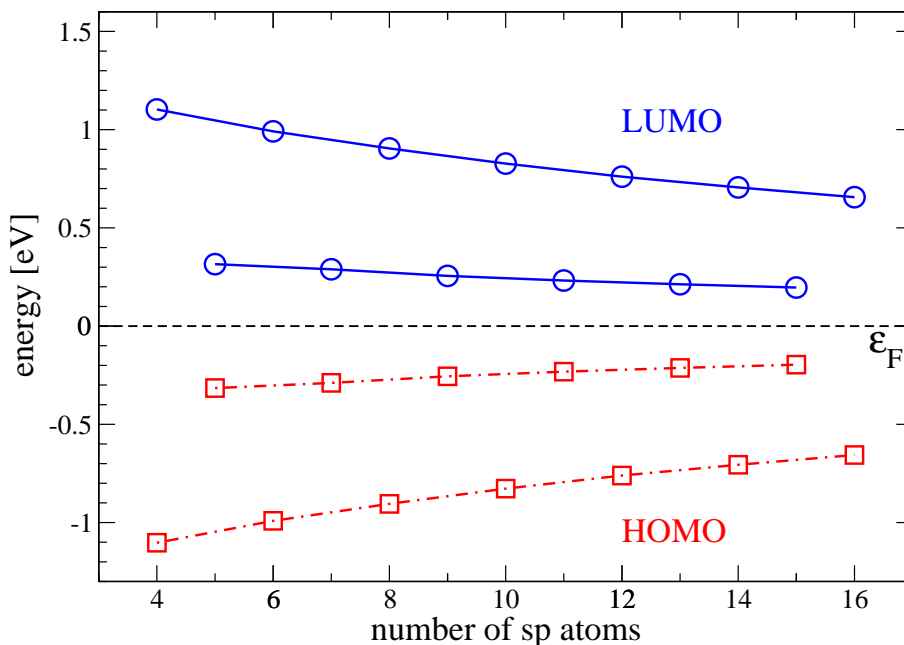


Figure 2.7: HOMO (in solid blue) and LUMO (in dot-dashed red) energies as a function of the number of atoms that compose the carbyne.

same gaps of Fig. 2.8(a) in nm instead of eV. The nature of the HOMO-LUMO gap of the odd- n chains is completely different from the one of the even- n molecules. This gap involves two states which are orbitally equivalent, but different only relatively to spin. It is clearly a spin gap based on the LSDA estimation of exchange. Accordingly, the evolution of the gap amplitude of odd- n chains is significantly different from the even- n ones. The analogous of the even- n chains gap for the odd- n ones is the optical gap of Fig. 2.8(a) calculated as the average between the majority spin and the minority spin gaps: the evolution of the gap amplitude of both even- n and odd- n chains indicates that the nature of these gaps is similar.

For even- n , Figure 2.9 reports the isovalues of the contribution of the electronic density of a few relevant electronic states around the Fermi energy, similar to Fig. 2.6. The HOMO (Fig. 2.9(b)) and LUMO (Fig. 2.9(c)) states of the carbyne are located in the plane orthogonal to the plane of the chain: the occupied π bonds are evident in the HOMO states, while the unoccupied ones are evident in the LUMO states. The HOMO-1 (Fig. 2.9(a)) and the LUMO+1 (Fig. 2.9(d)) states are located in the same plane of the terminations and in correspondence of the triple and single bonds, respectively. The isosurfaces show a non-zero overlap between the HOMO and LUMO and between the HOMO-1 and LUMO+1 states. Figure 2.10 shows the electronic density of relevant levels around the Fermi energy

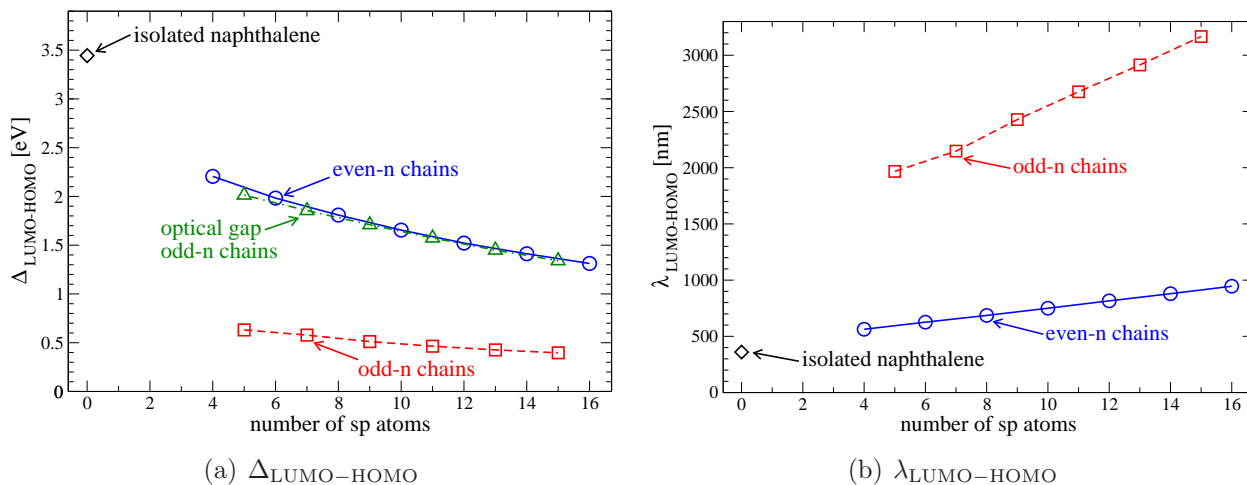


Figure 2.8: Difference in energy 2.8(a) and in wavelength 2.8(b) as a function of the number of atoms that compose the carbyne for the even- n chains (in solid blue) and for the odd- n chains (in dashed red). The optical gap (in dot-dashed green) of the odd- n chains is similar to the even- n gap. The value of this difference for the isolated naphthalene is reported in black.

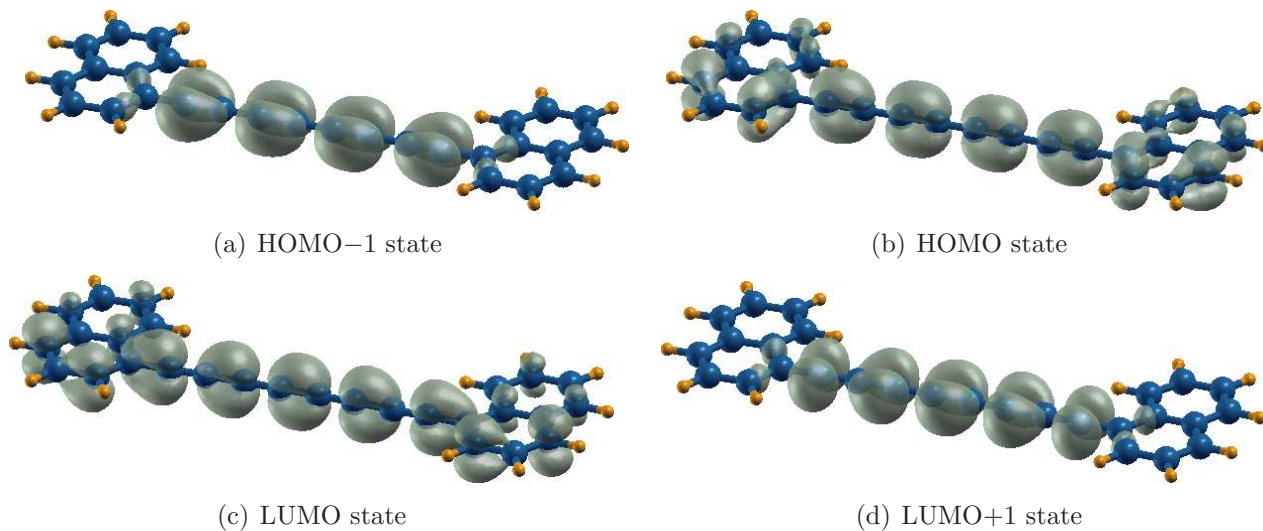


Figure 2.9: Electron density of 4 orbitals near the Fermi level for Naph_2C_8 . The isosurface plotted has value of $0.001 a_0^{-3}$.

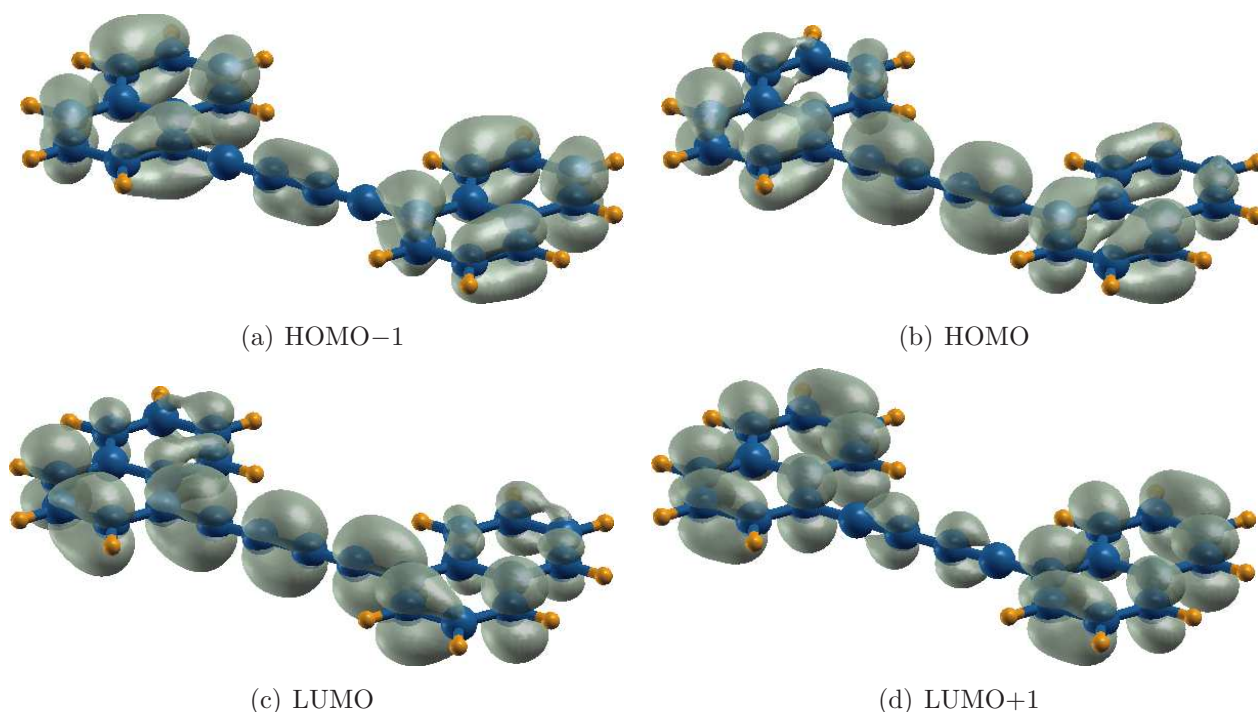


Figure 2.10: Electron density of 4 orbitals near the Fermi level for Naph_2C_4 . The isosurface plotted has value of $0.001 a_0^{-3}$.

for Naph_2C_4 : the HOMO (Fig. 2.10(b)) and LUMO (Fig. 2.10(c)) are similar to those of Naph_2C_8 . The HOMO-1 and LUMO+1 (Figs. 2.10(a) and 2.10(d)) are oriented in the plane perpendicular to the molecule, the former located in correspondence of the single bond, the latter of the triple ones. The overlap between the states of the chain and the states of the ligands is larger for Naph_2C_4 than for Naph_2C_8 . For longer chains the contribution of the ligands to the HOMO and LUMO is even smaller. All the molecules with a carbyne composed of at least 6 carbon atoms show similar patterns for the orbitals as in Fig. 2.9.

For the odd- n chain molecule, we need to consider the HOMO and LUMO for both the majority and the minority electron spin. The majority HOMO (HOMO_M) and the minority LUMO (LUMO_m) are of course essentially the same orbital, with the same shape (Figs. 2.11(b) and 2.11(c), respectively). These orbitals are localized on the odd-atoms of the carbyne, those characterized by a positive magnetization, shown in Fig. 2.5. Due to the twisted configuration of the molecule, the carbyne isosurfaces of the HOMO_m and LUMO_M states are alternatively in the same plane of the ligand and in the perpendicular one. They show a strong overlap among them and also with the electronic states of the terminations. In contrast the HOMO_M and LUMO_m have little overlap with the ligands. Each contour

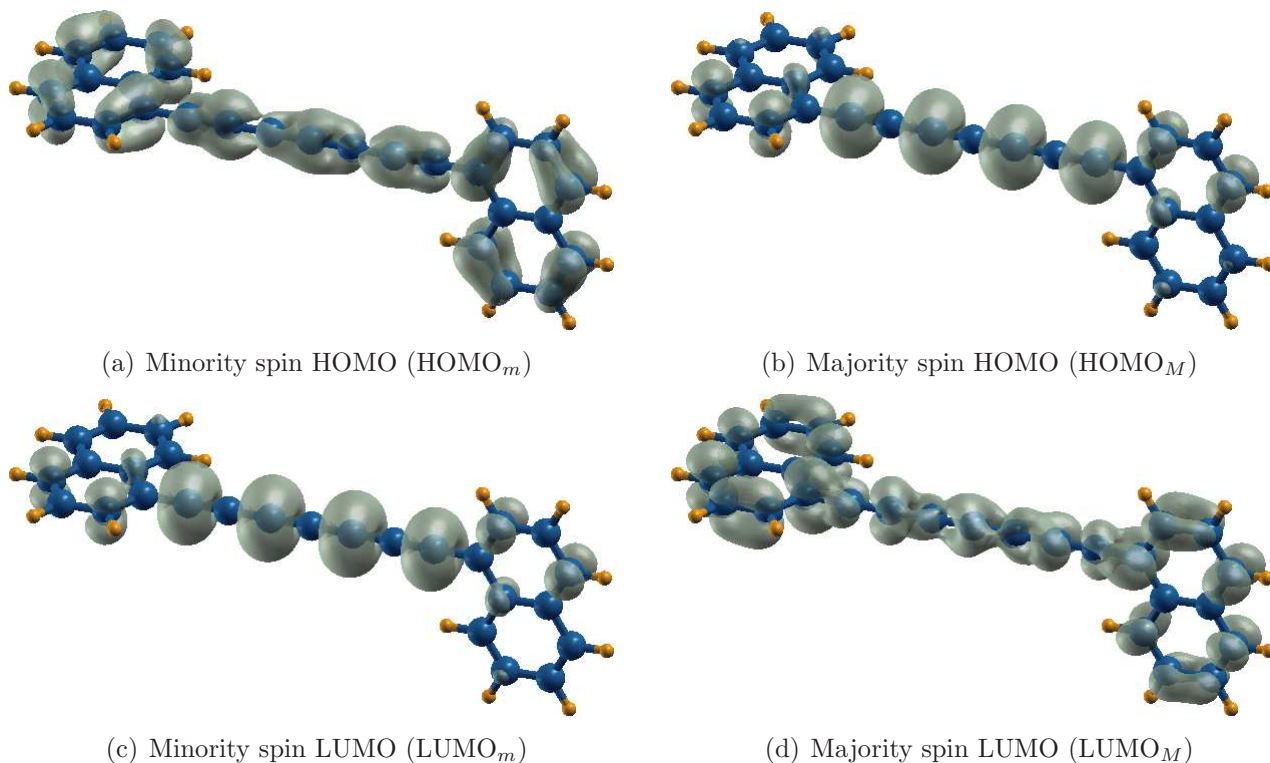


Figure 2.11: Electron densities of the majority and minority HOMO and LUMO of the Naph₂C₇ molecule. The majority HOMO and the minority LUMO are orbitally essentially equivalent. The isosurface plotted has value of $0.001 a_0^{-3}$.

plot is the result of the sum of the contributions of two levels split by a gap of less than 30 meV.

2.4. Vibrational Properties

2.4.1. The Even-*n* Carbynes. Ravagnan *et al.*, in Ref. [14, 25], reported the production and characterization of amorphous *sp* – *sp*² carbon films where the dominant *sp* species are cumulenes. This is obtained by supersonic cluster beam deposition on a substrate kept at a temperature of 150 K. By raising the film temperature to 325 K cumulenes undergo a reorganization inducing the formation of nanometric graphitic islands in the amorphous *sp*² matrix, while the amount of polyynes remained substantially constant in the investigated temperature range. The typical Raman spectrum of the film, thus obtained, shows two prominent features in the $1200 \div 1700 \text{ cm}^{-1}$ and $1900 \div 2300 \text{ cm}^{-1}$ spectral regions. The former region is typical of amorphous *sp*² carbon and is related to vibrational modes

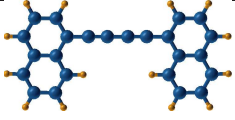
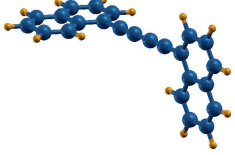
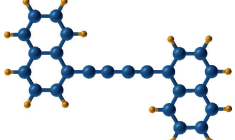
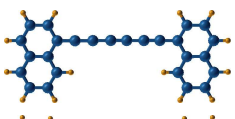
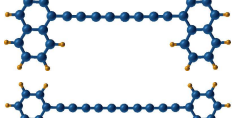
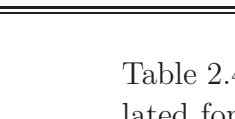
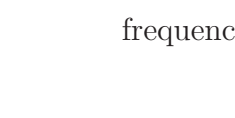
Molecular structure	Molecule nickname	Raman frequencies [cm ⁻¹]	IR frequencies [cm ⁻¹]
	Naph ₂ C ₄	2249	2175
	Naph ₂ C ₄ – 90°	2256	2175
	Naph ₂ C ₄ – 180°	2249	2175
	Naph ₂ C ₆	2119, 2204	2241
	Naph ₂ C ₈	2142 , 2209	2086, 2248
	Naph ₂ C ₁₀	2066, 2107 , 2252	2182, 2242
	Naph ₂ C ₁₂	2057 , 2155, 2257	2048, 2209 , 2233
	Naph ₂ C ₁₄	1999 , 2024, 2193, 2236	2117, 2168 , 2238
	Naph ₂ C ₁₆	1965 , 2104, 2225, 2230	2012, 2142 , 2179, 2249

Table 2.4: Wavenumber of Raman and IR carbyne-frequencies calculated for the Naph₂C_{2m} molecules. The most intense Raman and IR frequencies are in **bold**.

of sp^2 -hybridized sites [26]; the latter is associated to stretching modes of linear sp hybridized carbon structures. Traditionally, the two components peaked at 1980 and 2100 cm^{-1} are attributed generically to cumulenes and polyynes, respectively. The peak intensity at around 2100 cm^{-1} decreases in intensity when the sample is warmed up, while the intensity of the sp^2 peak around 1500 cm^{-1} increases in intensity, due to the reorganization of the sp -hybridized carbons into sp^2 -hybridized ones. The same characteristic spectrum was shown in linear carbon chains in the solid phase prepared using the dehydrochloridation

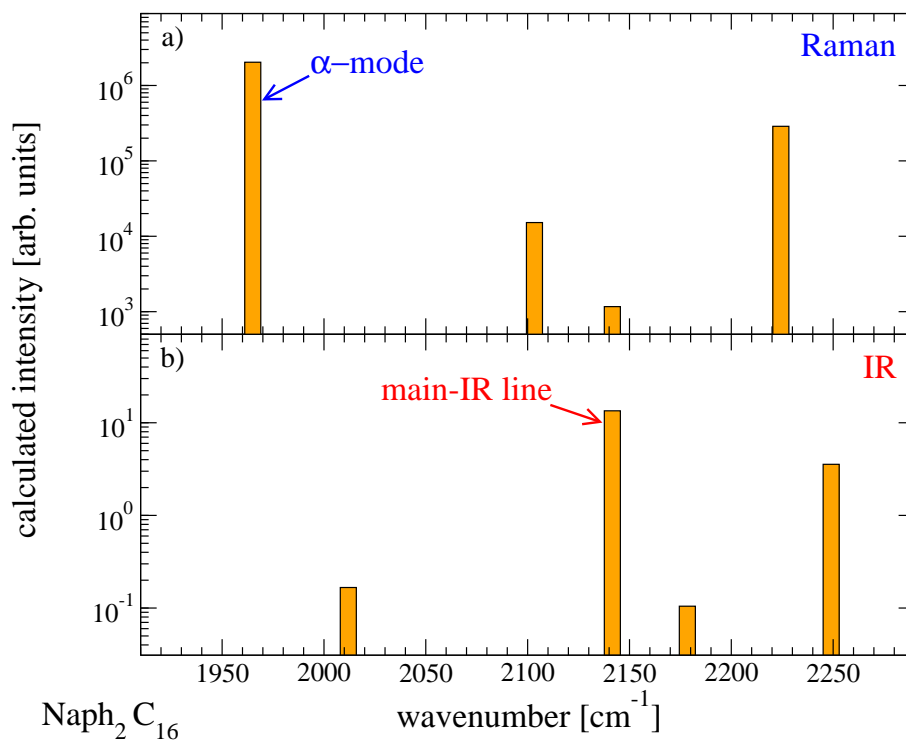


Figure 2.12: Calculated intensity of Raman (a) and IR (b) frequencies for the $\text{Naph}_2\text{C}_{16}$ molecule.

of either polyvinylchloride [27] or chlorinated polyacetylene [28] using organic strong base. In Ref. [29], Kinoshita *et al.* presented the synthesis and characterizations of a conjugated butatriene polymer having dodecyloxy side chains: these molecules show the characteristic Raman peak at 2035 and 2045 cm^{-1} .

Starting from the relaxed position of Sect. 2.1, we calculate the vibrational modes and frequencies of the Naph_2C_n molecules. According to our calculations, also the Naph_2C_n molecules display a characteristic Raman-active stretching modes in the range $1950 \div 2300 \text{ cm}^{-1}$ (Table 2.4), typical of polyynic chain. Figure 2.12 shows the intensities (in arbitrary units and in logarithmic scale) of all the frequencies computed for $\text{Naph}_2\text{C}_{16}$: the most intense Raman and IR frequencies, called Raman- α and main-IR, are almost one order of magnitude more intense than the most intense other Raman or IR mode.

In Fig. 2.13, we plot the most intense Raman and IR frequencies as a function of the *sp*-atoms in the even-*n* carbyne: the most intense Raman frequency decrease by about 50 cm^{-1} for each increase of 2 atoms in the carbyne. The frequency of the most intense IR mode changes much less than the frequency of the Raman- α , but is found in the same frequency range as the Raman-active modes. A rotation by 90° or 180° between the two naphthalenes

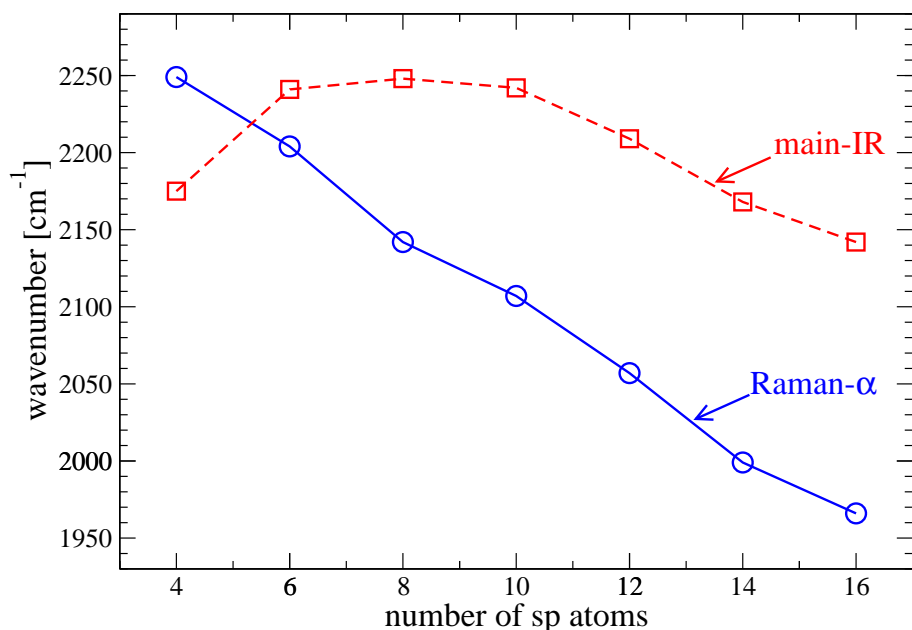


Figure 2.13: Wavenumber of the Raman (solid blue) and IR (dashed red) most intense frequencies, reported in **bold** in Table 2.4, as a function of the number of atoms composing the carbynic section of dinaphthyl-polyynes.

induces a 7 cm^{-1} shift in the Raman mode of the $\text{Naph}_2\text{C}_4 - 90^\circ$. All the other frequencies remain the same regardless of twist.

Figure 2.14 shows the intensities of the vibrational modes plotted as a function of the sp carbon atoms: either the Raman or the IR most intense mode shows a rapid increase with the number of atoms in the carbyne. According to the values of the molar concentration, reported in Table 2.1 as a function of the number of atoms of the carbyne, of the sample produced by F. Cataldo, using the method described at the beginning of this chapter, a shorter chain is more concentrate in the experimental solution than a longer one. On the other hand, our calculations suggest that a longer chain has a Raman- α and a main-IR mode more intense than the Raman- α and main-IR frequency of a shorter chain.

Both the frequency and the intensity of the Raman- α line show a sort of zig-zag as a function of the length of the molecule depending on the multiplicity of the number of carbon atoms: indeed if the number of sp atoms is an integer multiple of 4 the central bond is a single bond, while it is a triple bond in the other case (Table 2.2). The same oscillation occurs for the main-IR line.

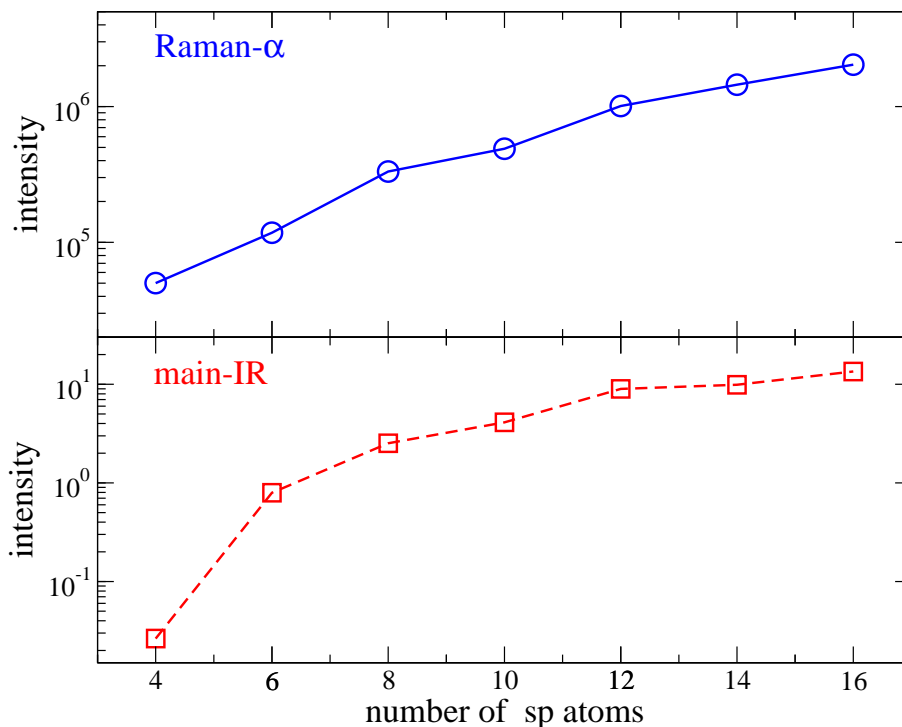


Figure 2.14: Intensity (in arbitrary units and in logarithmic scale) of the Raman (solid blue) and IR (dashed red) most intense frequencies as a function of the number of the sp atoms.

According to Ref. [30], the most intense Raman mode shows a common displacement pattern of the C-C stretching of the carbyne: in Fig. 2.15 are shown the patterns of the two most intense different frequencies for the Raman and IR modes of the $\text{Naph}_2\text{C}_{16}$. As shown in Fig. 2.12, the considered frequencies are 1965 and 2224 cm^{-1} for the Raman modes and 2141 and 2249 cm^{-1} for the IR ones. The bars of Fig. 2.15 represent the displacement of each atom with respect to its equilibrium position. The vibrational patterns displayed in the panels on the left correspond to the Raman modes, on the right to the IR ones. In the Raman- α mode all triple bonds expand and all single bonds shrink in phase and the maximum displacement is shown for the atoms at the center of the chain and decrease moving towards the ends of the carbyne. In the IR most intense mode the central bond suffers from a translation, in the first half of the chain the triple bonds shrink and the single ones expand and vice versa in the second half. The result is a pattern with two maxima set at 1/4 and 3/4 of the carbyne. The vibrational patterns of the other modes are somewhat complicated.

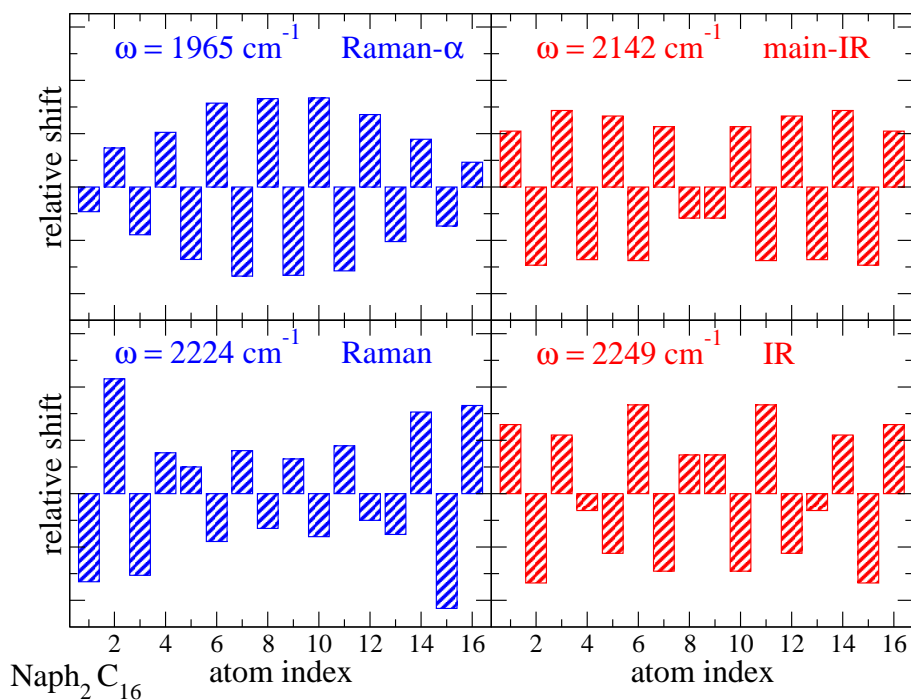


Figure 2.15: Absolute displacement patterns (arbitrary units) of the most intense (see Fig. 2.12) C-C stretching vibrational modes obtained for the $\text{Naph}_2\text{C}_{16}$ molecule, which vibrate at the indicated frequencies. The left-hand panels show two Raman modes and the right-hand panels show two IR modes. The bars represent the displacement of each atom with respect to its equilibrium position.

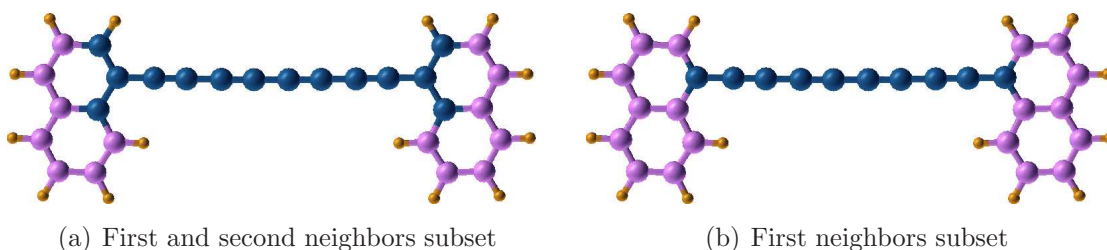


Figure 2.16: Subset (dark/blue) of atoms used in the linear response calculation for calculate phonon frequencies. Left: the subset includes the carbyne plus its first and second neighbors. Right: subset composed of the carbyne-atoms plus its first neighbors only.

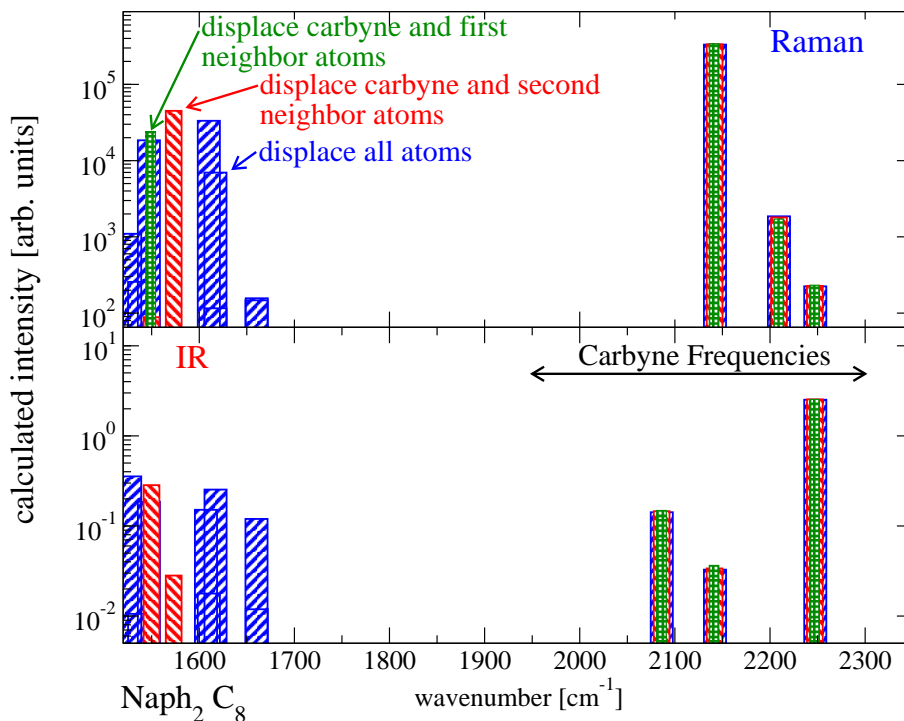


Figure 2.17: Comparison of three different calculations of the phonon frequencies and intensities of Naph_2C_8 . In the carbyne frequency range ($1950 - 2300 \text{ cm}^{-1}$), there is no significant change of intensity or shift in frequency in the calculations based on the two different subset of atoms with respect to the complete calculation.

All the calculations presented until now included the displacement of all atoms in the phonon calculation in order to obtain the wavenumbers and the intensities of the vibrational modes. As we are interested in the polyynes stretching modes only, we could attempt calculations where we keep a subset of the atoms in the linear response calculation. This method has the result of reducing the computational time on one side and of losing accuracy on the other. As we are interested only in the modes of the carbyne, we can choose between two subset of atoms: in a more conservative one, we compute the dynamical matrix for the atoms of the carbyne plus its first and second neighbors (Fig. 2.16(a)) and in the other, we use the atoms of the carbyne plus its first neighbors only (Fig. 2.16(b)). Figure 2.17 shows that both choices of the subsets reliable valid in order to obtain the wavenumbers and their intensities for different stretching modes, when compared to those obtained by computing the linear response for all atoms, at least in the range of frequencies typical of carbyne modes. The computational time of the phonon modes parallel calculation of the Naph_2C_8 performed on

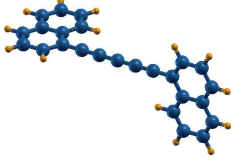
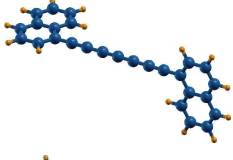
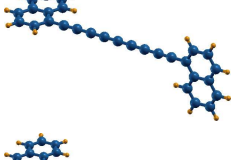
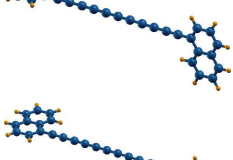
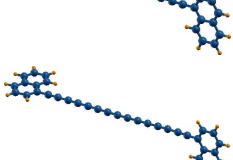
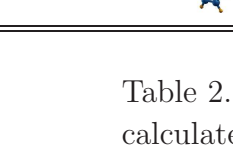
Molecular structure	Molecule nickname	Raman frequencies [cm^{-1}]	IR frequencies [cm^{-1}]
	Naph ₂ C ₅	2079	1770, 1923
	Naph ₂ C ₇	1782, 2119	1854, 2081
	Naph ₂ C ₉	2061, 2112	1775, 1800, 2148
	Naph ₂ C ₁₁	1794, 2087, 2139	1726, 2043, 2166
	Naph ₂ C ₁₃	2022, 2057, 2174	1670, 1796, 2122, 2165
	Naph ₂ C ₁₅	1796, 2017, 2100, 2182	2003, 2148, 2161

Table 2.5: Wavenumber of Raman and IR carbyne stretching modes calculated for the Naph₂C_{2n+1} molecules.

a parallel computer with 24 processors (Intel(R) Xeon(R) CPU X5460 @ 3.16 GHz) is about 50 hours for the full calculation including all displacements, 20 hours for the more conservative subset of Fig. 2.16(a) and 15 hours for the subset of Fig. 2.16(b). This technique will be used in the following part of this section to compute the vibrational properties of odd- n chains and also in Sect. 3.6 for the carbyne-graphene composed systems.

2.4.2. The Odd- n Carbynes. As shown in Sect. 2.2, the odd- n carbyne molecules are magnetic; technically this feature prevents us to compute the Raman tensor which is not implemented in the Quantum Espresso code for system where metallic occupancies need to be considered.

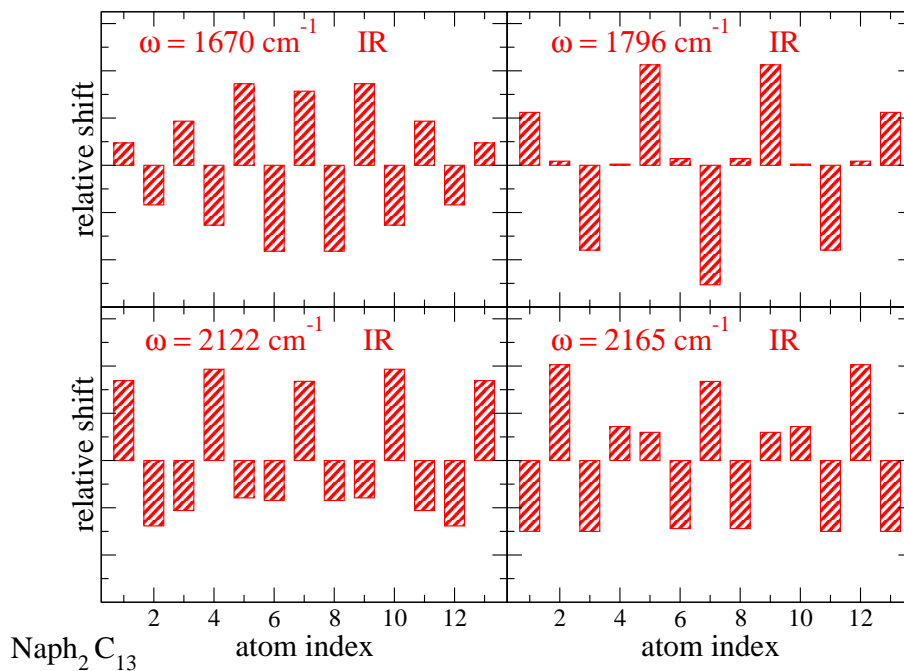


Figure 2.18: Absolute displacement patterns (arbitrary units) of the IR C-C stretching vibrational modes obtained for $\text{Naph}_2\text{C}_{13}$ (see Table 2.5), which vibrate at the indicated frequencies. The bars represent the displacement of each atom with respect to its equilibrium position.

The behavior of the calculated Raman and IR frequencies, shown in Table 2.5, is quite different from that discovered for the even- n chains: the frequencies range between 1750 and 2200 cm^{-1} , with a minimum value about 200 cm^{-1} lower than the corresponding even- n carbon chain (i.e. 1900 cm^{-1}), similar to those found by Fan *et al.* in Ref. [31] for the C_{2m} and C_{2m+1} chains.

The absolute displacement patterns of the IR and Raman frequencies of the $\text{Naph}_2\text{C}_{13}$ are shown in Figs. 2.18 and 2.19, respectively. These patterns are sufficiently different from those obtained for the even- n chains. This fact prevent us to make a prevision on the most intense Raman and IR modes without direct calculation.

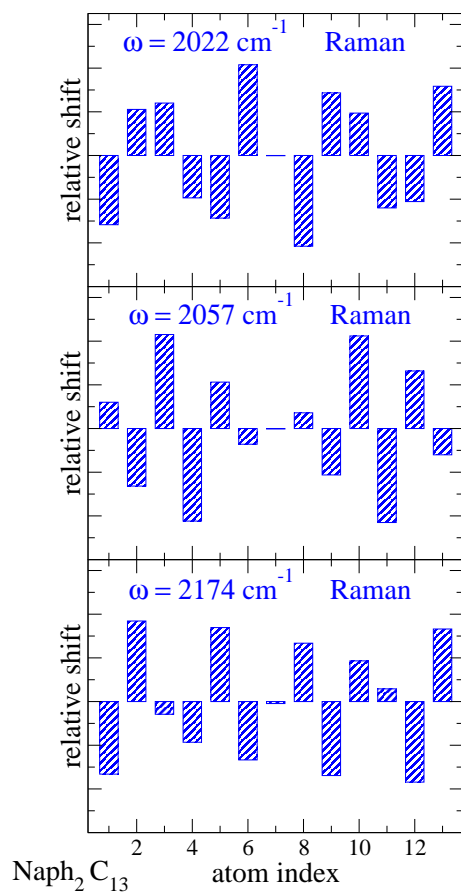


Figure 2.19: Absolute displacement patterns (arbitrary units) of the Raman C-C stretching vibrational modes obtained for Naph₂C₁₃ (see Table 2.5), which vibrate at the indicated frequencies. The bars represent the displacement of each atom with respect to its equilibrium position.

CHAPTER 3

The Graphene Termination

The present chapter deals mainly with the structural, vibrational, and electronic properties of different sp -bonded carbon chains inserted into a hole defect of a graphene layer. In Appendix A.2.2, we describe the computational choices made for the simulations of this chapter.

3.1. A Chain on a Complete Layer

We start off by analyzing the reactivity of a linear (Fig. 3.1(c)) or curved (Fig. 3.1(d)) carbyne interacting with an infinite graphene layer. We analyze the energies as a function of the distance and position of the carbyne with respect to the graphene surface, which we initially take as flat. The bonding energy (E_{bond}) is defined as the difference between the total energy of the system including the graphene sheet near to the carbyne (E_{g+c}), and the

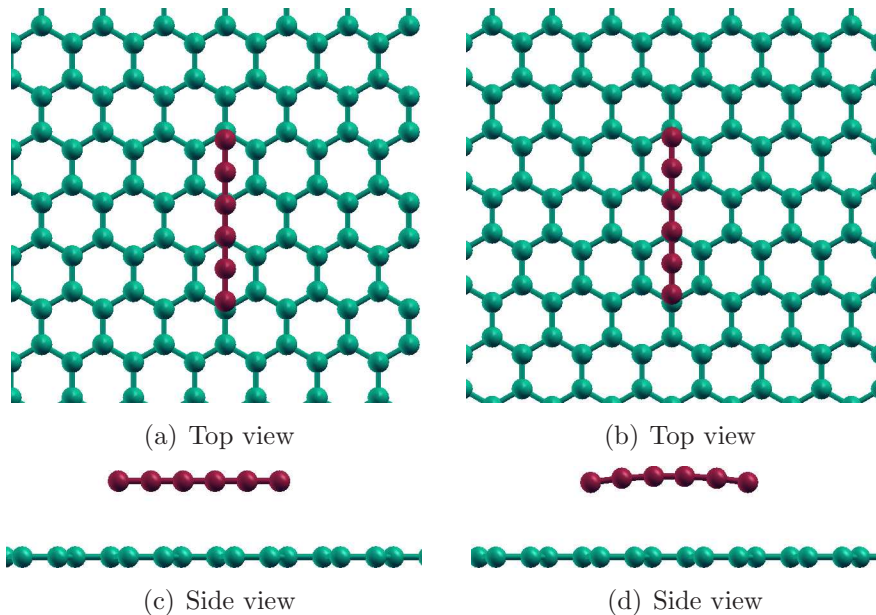


Figure 3.1: Positions of the superlattice and carbyne atoms. Different color as a function of the z -coordinate of the position.

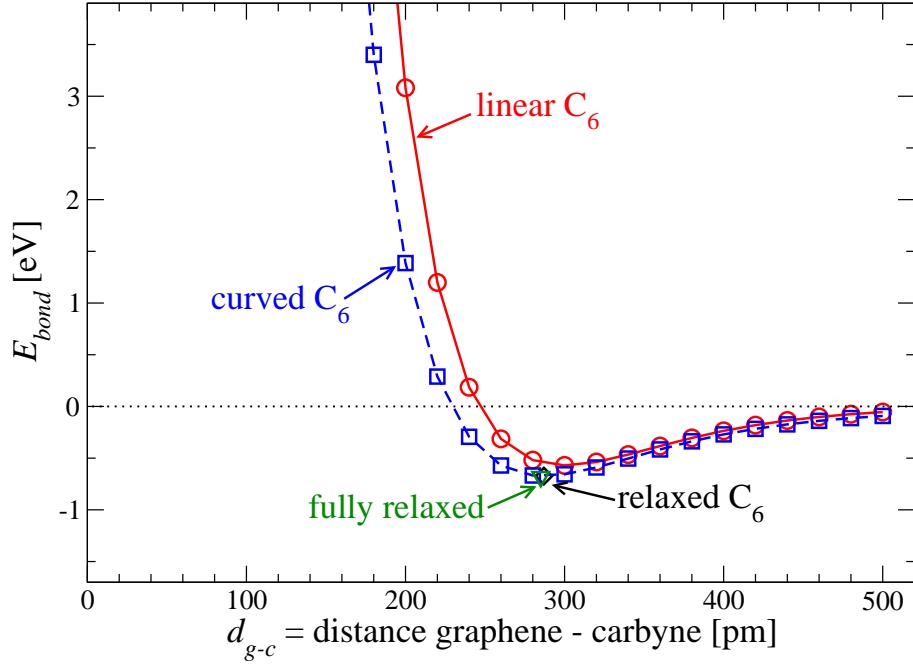


Figure 3.2: Bonding energy of a rigid graphene lattice with a rigid linear (red circles) and a rigid curved (blue squares) C_6 carbyne. The distance (d_{g-c}) is calculated between the graphene sheet and the nearest atoms in the chain, along the normal vector to the surface. The black diamond reports the value of E_{bond} and of d_{g-c} of a fully relaxed carbyne, 6 atoms long, on a fixed-positions graphene sheet. The green triangle reports the value of E_{bond} and of d_{g-c} obtained relaxing the system in full.

sum of the energies of the separated graphene sheet (E_g) and the carbyne (E_c):

$$(2) \quad E_{bond} = E_{g+c} - (E_g + E_c) .$$

We perform total energy calculations, at fixed atoms positions: these positions are initialized starting from the fully relaxed positions calculated separately for the graphene sheet and for the $n = 6$ atoms carbyne for the linear chain; for the curved chain configuration, the positions of the atoms of the carbyne are initialized starting from the fully relaxed positions computed for a chain on a frozen graphene sheet, as shown in Fig. 3.3. As shown in Fig. 3.2, for $d_{g-c} \lesssim 220$ pm the graphene and the carbyne repel each other, and $E_{bond} > 0$ eV; for $d_{g-c} \gtrsim 220$ pm a weak attraction is observed. This result remains qualitatively the same for all reciprocal positions of the graphene and the chain, both in the linear and the curved geometry: the equilibrium distance is near 280 pm. Considering carbynes of the same shape,

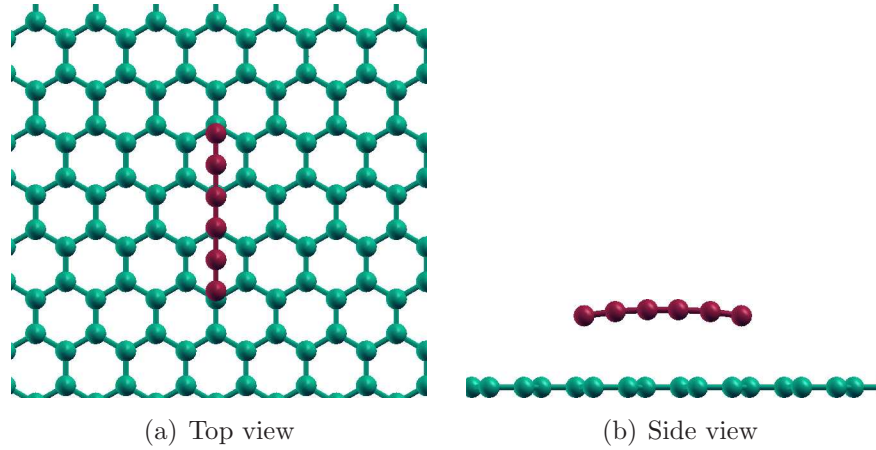


Figure 3.3: Positions of the superlattice and carbyne atoms. The carbyne is relaxed on a graphene sheet of fixed positions. Different color as a function of the z -coordinate of the position.

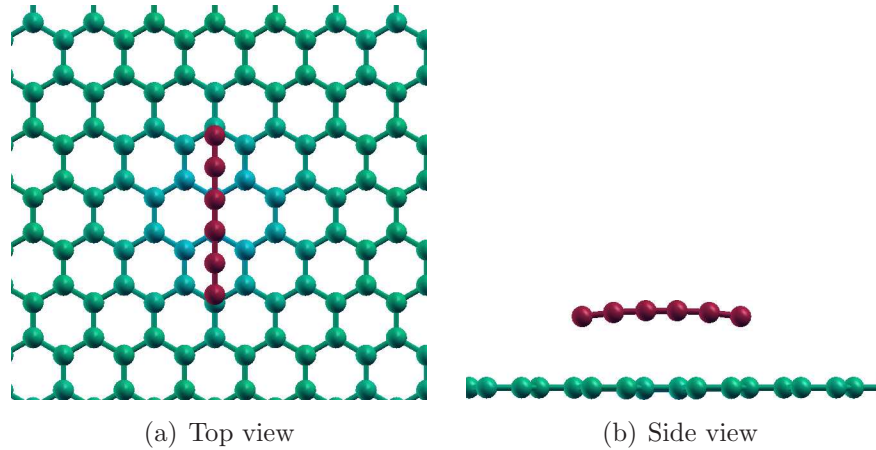


Figure 3.4: Positions of the superlattice and carbyne atoms. The positions of the atoms either of the graphene foil or the chains are fully relaxed. Different color as a function of the z -coordinate of the position.

only in the strongly repulsive region (for $d_{g-c} < 160$ pm), we observe a significant difference in the value of E_{bond} for different relative chain-graphene locations.

We also consider the possibility of fully relaxing the C_6 carbyne near a frozen graphene sheet (Fig. 3.3): the values of E_{bond} and of the distance between the chain and the foil is

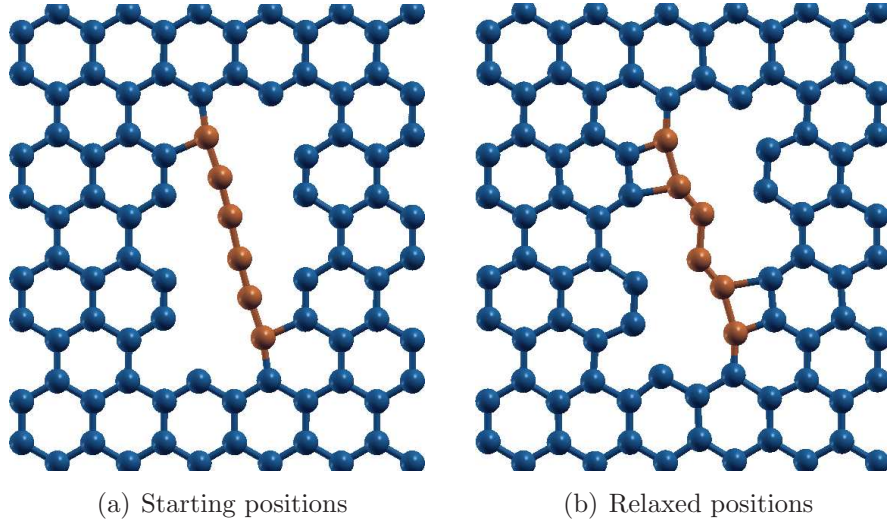


Figure 3.5: Starting and relaxed positions of the system nanohole-carbyne: the lateral dimension of the nh is too small and the atoms of the carbyne (in maroon) interact with the two armchair edges that reconstruct.

reported in Fig. 3.2. $E_{bond} = -0.7$ eV and the overall distance of the chain from the graphene sheet (nearest atom) is 287 pm.

Figure 3.4 shows the positions of the graphene sheet and of the chains obtained relaxing the system in full. The reciprocal interaction between the foil and the chain has the effect of a weak lowering the graphene atoms just under the carbyne. The value of E_{bond} is lower of 7 meV with respect to the value computed for the configuration of a carbyne relaxed on a frozen graphene sheet and the overall distance of the chain from the graphene foil is 285 pm.

3.2. The Nanohole

Starting from the perfect graphene foil of Fig. A.3, we remove some atoms in order to form a nanohole (nh). Our purpose is to understand how various properties of the system are influenced by different kinks of carbynes bonded to the edge of this hole. The size of the nh should be such that inserted carbyne chains fit and only bind at their ends. If we create a too small nh, then chain carbon atoms would reconstruct the edges of the hole. As an example of a small nh, Figure 3.5 shows a carbyne (6 atoms long, in maroon) bonded to the zig-zag edges that, after being fully relaxed, becomes a 2-atoms long chain: in fact, due to the interaction between the *sp*-chain and the armchair edges, a few carbyne atoms are captured by these edges forming extra bonds with the nh. A nh of this shape/dimension is therefore useless for the purpose of investigating end-binded carbynes in the nh. Also in a nh

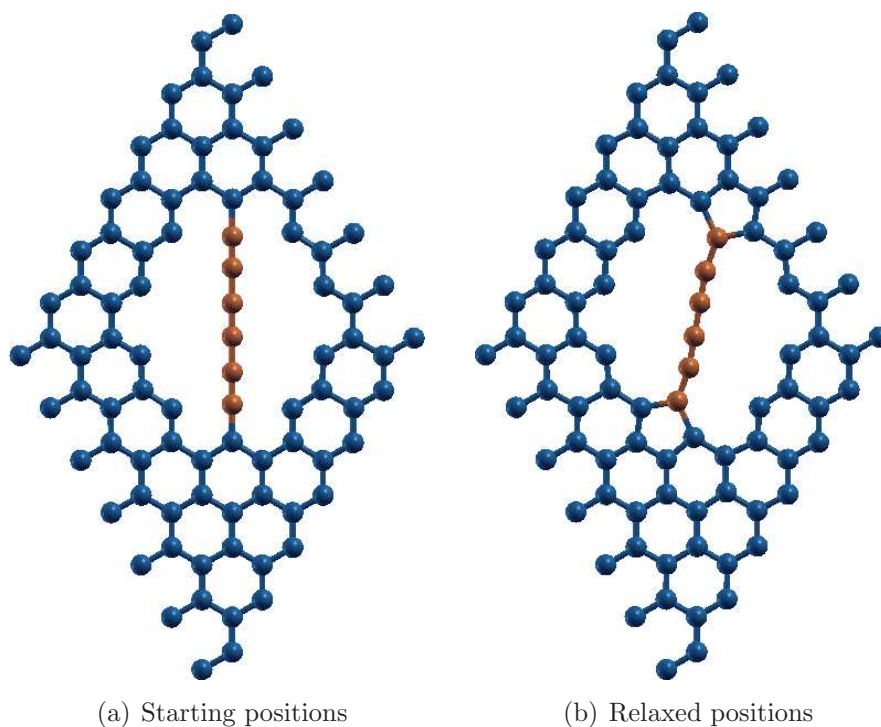


Figure 3.6: Starting and relaxed positions of the system nanohole-carbyne in a hexagonal cell: the carbyne is too near to the edges of the nh that reconstructs.

built in a hexagonal cell (Fig. 3.6), the distances between the carbyne and the nh edges are too small, with the result that a few atoms of the chain interact with the nh and reconstruct its edge by forming two additional pentagons.

We must therefore consider a sufficiently big nh: we need a distance of at least 300 pm between the chain and the edges in order to avoid this sort of reactions. The nh that we consider optimal for our purposes is shown in Fig. 3.7. Starting from the perfect graphene of Fig. A.3, the nh is obtained by removing 28 atoms forming a rectangular hole of size 975 pm \times 985 pm with edges composed of 3 zig-zags and 2 armchairs. The size of the nh permits us to insert several carbynes, from 5 to 8 atoms long, and in various positions relative to the hole. We study most extensively a symmetric configuration with a chain bonded at the middle of one zig-zag edge to the opposite zig-zag edge, but we consider also a configuration of carbynes bonded to the armchair edges.

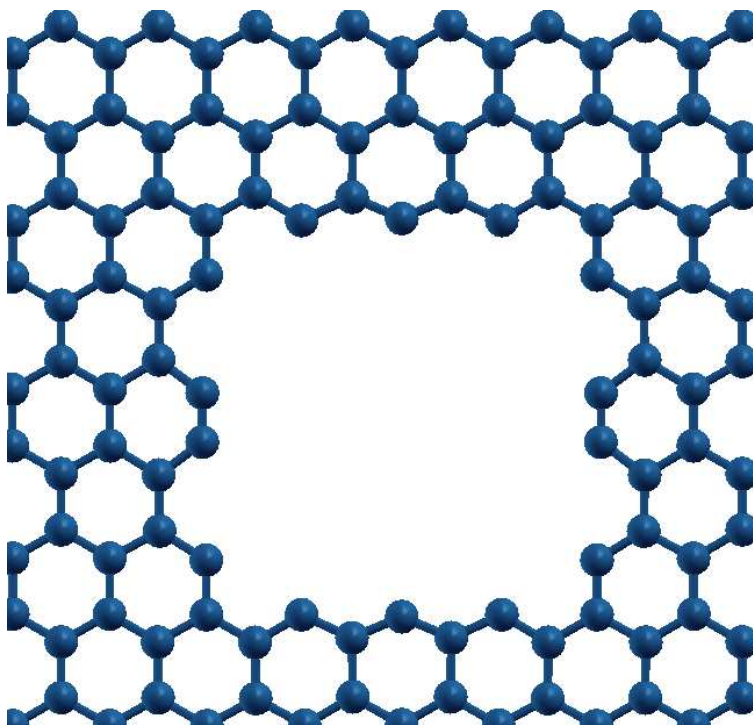


Figure 3.7: Relaxed positions in the nanohole superlattice: removing 28 atoms from the perfect graphene of Fig. A.3, we obtain a rectangular hole of dimension of $975 \text{ pm} \times 985 \text{ pm}$ with edges composed of 3 zig-zags and 2 armchairs.

3.3. A Carbyne Binding to a Nanohole

Our initial purpose is to investigate the properties of a nh in a system composed of several layers of graphene (like in graphite). This configuration is more realistic with respect to a single free-standing mono-layer of graphene although in cluster assembled $sp - sp^2$ carbon films one must expect that defective single graphene layers are relatively abundant. Consider a system of one layer of perfect graphene and a layer with a nh, such as that described at the end of Sect. 3.2. Figure 3.8 shows this configuration with the insertion of 6 atom long linear chain. This configuration is fully relaxed, relatively to the upper graphene layer and the carbyne atoms, while the lower layer is kept frozen in ideal graphitic positions. The distance between the two layers is very close to the typical distance between the layers of graphite and equals 332 pm .

A system composed of over 200 atoms is computationally very expensive; in fact a parallel calculation performed of 32 processors took more than two weeks to obtain a fully relaxed configuration. On the other hand, the properties of this two-layer configuration

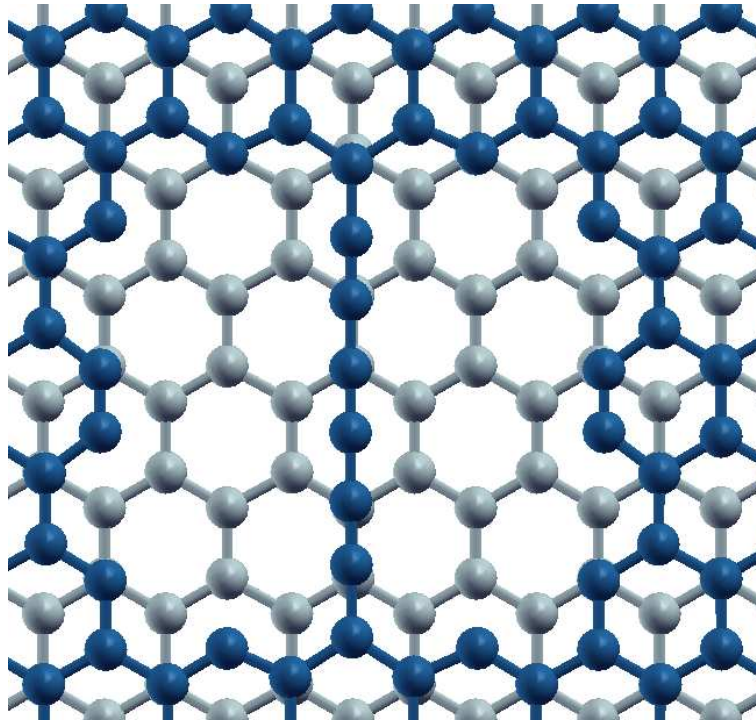


Figure 3.8: System composed of a perfect graphene foil and a nh sheet stacked in the standard AB arrangement of graphite. A 6-atom long carbon chain is bonded to the graphene inside the nh. The distance between the two layers equals 332 pm. The lower sheet atoms are in pale blue, the upper ones in dark blue.

do not change significantly by considering the same system without the perfect graphene sheet. Indeed the forces between the two layers are weak long-range forces whose action is very small with respect to the intra-layer forces. The DFT-LSDA estimation of such weak dispersion forces is unreliable anyway. These observations convinced us that it makes good sense to consider a system composed of a single layer, the one containing the nh, plus the C_6 carbyne inserted into it. The relaxation of the positions, performed in the same conditions as above, took about one week only in this simpler configuration involving 90 C atoms in total.

In our calculations, we consider different chains, from 5 to 8 atoms long, in different reciprocal positions relative to the hole. Table 3.1 summarizes the structural properties of the configurations considered with their BLAs and bonding energies. The value of the BLA is strongly influenced by the length of the carbyne inserted into the hole: a stretched configuration leads to a enhanced BLA typical of polyynic chain (such as nh- C_6 *arm*, whose

Name	Description	BLA [pm]	E_{bond} [eV]
nh-C ₅ (Fig. 3.9(a))	C ₅ chain laying in the same plane of the graphene. The carbyne is stretched, the first and the last carbon of the chain are weakly bonded to the edge of the nh (bond lengths of 170 pm).	7	4.2
nh-C ₅ 1b (Fig. 3.9(b))	C ₅ chain laying in the same plane of the graphene. The chain is bonded to the nanohole only on one side; the bond lengths of the carbyne atoms are similar to those of a cumulenic chain (127 pm).	1	6.2
nh-C ₆ zig (Fig. 3.9(c))	C ₆ chain laying in the same plane of the graphene. The weakly stretched chain is bonded to the zig-zag edge.	10	12.9
nh-C ₆ arm (Fig. 3.9(d))	C ₆ chain laying in the same plane of the graphene and joins opposite armchair edges at an sp^2 atom. This configuration has only two symmetry planes.	12	8.2
nh-C ₇ curved (Fig. 3.9(g));	C ₇ carbyne squeezed in the nh with various binding shapes, all joining the two zig-zag edges (Fig. 3.9(e)): the curved carbyne, in which the chain is bent out of the graphene plane (the maximum height of the chain equals 120 pm); the s-curved chain, with the atom at the center of the chain in the same plane of the graphene and the bending in opposite directions relative to the sheet; the straight carbyne, in which the chain is compressed into the graphene plane.	3	12.0
nh-C ₇ s-curved (Fig. 3.9(h));		3	11.9
nh-C ₇ straight (Fig. 3.9(i))		2	11.8
nh-C ₈ (Figs. 3.9(f), 3.9(j))	A C ₈ curved carbyne. The maximum height of the chain equals 297 pm.	6	12.5
wnh-2C ₆ (Fig. 3.10)	Two C ₆ carbynes inserted in the same plane of a wider hole (the edges are composed of 5 zig-zag and 2 armchair structures) and join the zig-zag edges. The horizontal distance between the chains equals 491 pm.	11 for each chain	N.C.

Table 3.1: Summary of the different configuration considered for the system carbyne and nh with BLA and total bonding energy E_{bond} , corresponding to the formation of the usually two bonds.

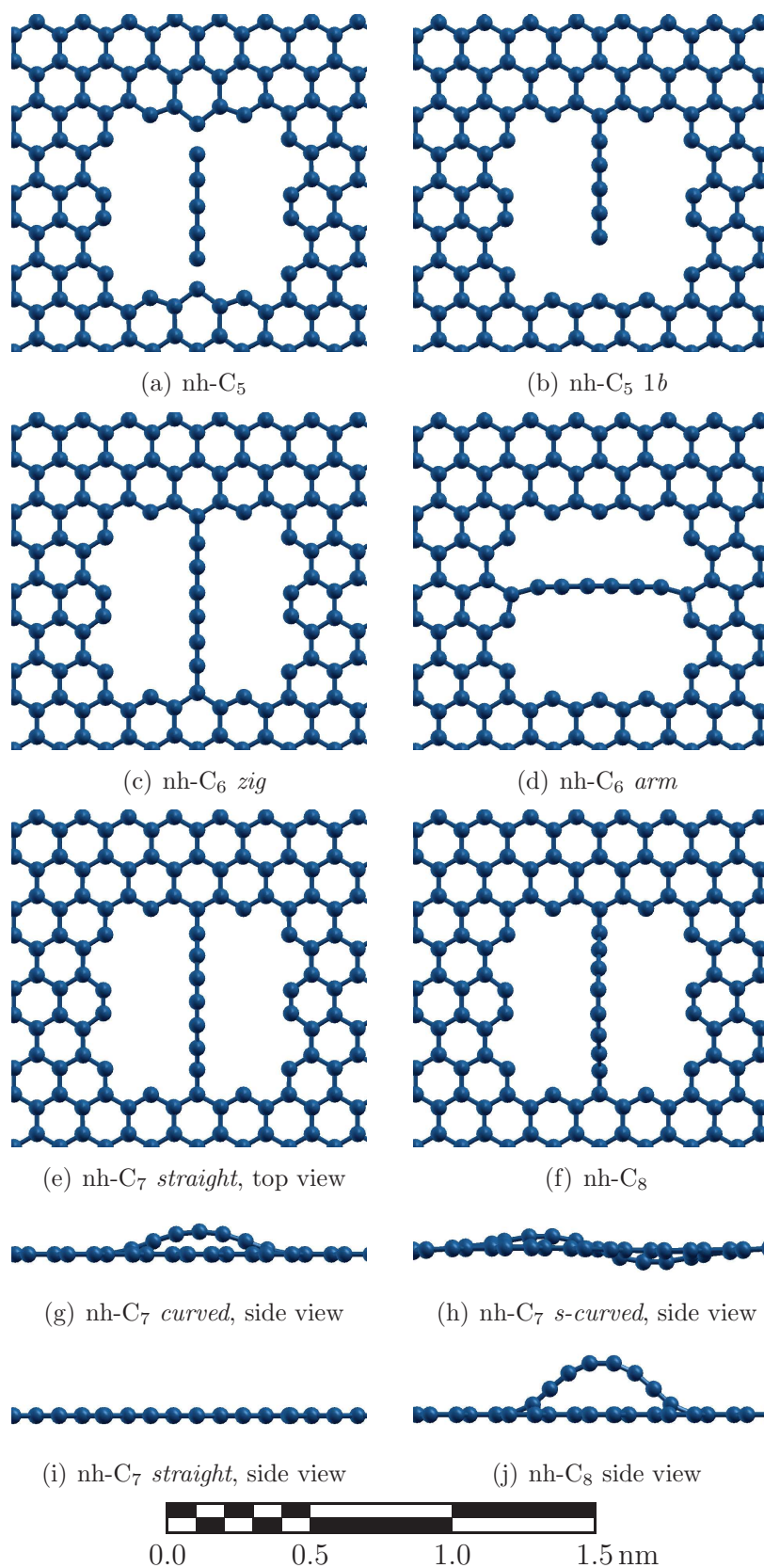


Figure 3.9: Configurations of the structures considered in the present chapter and described in Table 3.1.

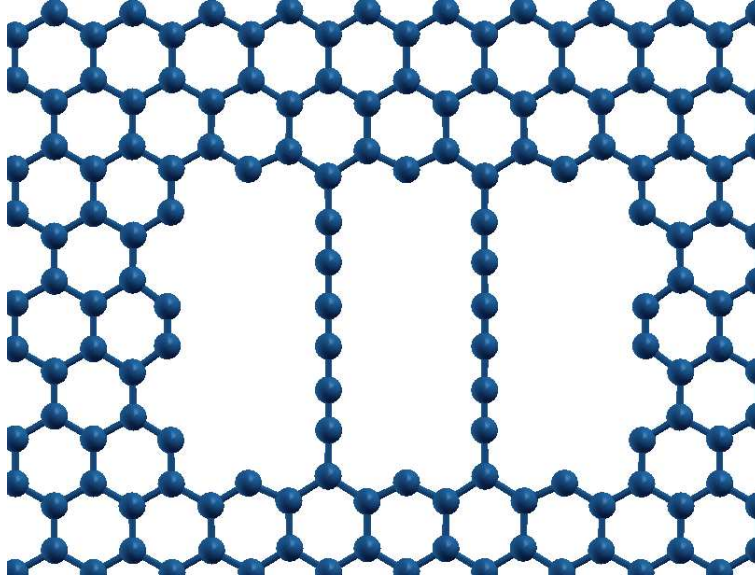


Figure 3.10: Relaxed position of the wider nh with two C_6 carbynes: the hole is wider than those considered in Fig. 3.9 in order to avoid the recombination of the two carbynes. This configuration displays no significant novelty relative to the single carbyne nh- C_6 zig configuration.

BLA reaches 12 pm), while a chain compression leads to a more cumulenic value (e.g. nh- C_7 *straight*, with its BLA $\simeq 2$ pm). No significant variation in BLA is shown for a change in the shape of the carbyne, as shown for nh- C_7 , for which we perform three calculations for the different shapes of the carbyne: the curved and the s-curved geometry and the straight one. For all of them the BLA takes values from 2 to 3 pm. The highly stretched nh- C_5 displays an intermediate polyynic character (BLA $\simeq 7$ pm) despite its odd- n and bonding between the chain and the nh is weak ($E_{bond} = 4$ eV). This configuration is obtained starting with the atoms of the chain in symmetric positions with respect to the edges of the hole, but if at the beginning of the calculation the chain is positioned significantly closer ($\simeq 50$ pm) to one edge than to the other, we obtain an optimized geometry with only one bond between the chain and the nh (nh- C_5 *1b*), and with internal bond lengths that are practically equal those of isolated C_5 . Eventually this single-bond formation is the most stable configuration, with a total energy 2 eV lower than the nh- C_5 geometry, Fig. 3.9(a), which represents a local minimum, i.e. a metastable configuration. Due to the small size of the nh, the C_8 chains can only fit in a curved geometry: the maximum out-of-plane elevation of the chain equals 297 pm. The BLA is intermediate between cumulenic and polyynic chains (BLA $\simeq 6$ pm).

We also consider a wider nh in which one can insert more than one chain: in wnh-2C_6 , the nanohole contains two C_6 carbynes at a distance large enough to keep them separated. The BLA is like the one obtained for the nh-C_6 .

We evaluate the bonding energy of the configurations described here. Due to its stretching, the nh-C_5 has a little value of $E_{\text{bond}} \simeq 4$ eV, while for the nh-C_5 *1b* $E_{\text{bond}} = 6.6$ eV which can be considered the best estimate of the carbyne-graphene edge binding energy. For all other configurations $E_{\text{bond}} \simeq 12$ eV indicative of the formation of two bonds, at the expense of approximately 1 eV elastic energy

In all systems discussed until now we connect the carbyne to the zig-zag edges. A different configuration is obtained binding the chain to the armchair edges (nh-C_6 *arm*): in that case, the BLA takes the value 12 pm, similar to that obtained for the nh-C_6 *zig*, and associated to a tensile strain. The bonding energy is lower ($E_{\text{bond}} \simeq 9$ eV), due to the lower reactivity of the armchair edge relative to the zig-zag one.

The relaxed positions of all structures investigated here are displayed in Figs. 3.9 and 3.10.

3.4. Magnetic Properties

Yu *et al.* [33], studied the magnetic behavior of a nanohole in a supercell geometry similar to ours, but using a rhombus supercell. They built rhombus or hexagonal holes with only zig-zag edges. Zig-zag edges are generally known to be ferrimagnetic [34, 35]. Yu *et al.* [33] investigated the relation of the magnetization of two consecutive zig-zag edges and discovered that the alignment of magnetism is ferromagnetic if the atoms belong to the same graphene sublattice (which happens when the subsequent zig-zag edges are rotated by 0° or 120° (like in a triangular hole). In the opposite case, the magnetization is antiferromagnetic, as happens for zig-zag edges rotated by 60° or 180° (e.g. rhombus and hexagonal hole). The angle between two edges is defined as the angle between two in-plane vectors normal to the edges. The schematic representation of the geometry relationships among graphene edges is shown in Fig. 3.11.

Our nh is quite different because it involves two armchair edges: magnetism with localized-spin moments is possible due to the existence of non-bonding localized states at the zigzag edge, but these states do not occur at the armchair edge [36]. All structures described in Sect. 3.1, show a nonzero absolute magnetization, localized on the zig-zag edges. Also the carbyne carries magnetization in the case of odd-chains, while the even-ones are non-magnetic, as illustrated in Fig. 3.12 for the nh-C_5 and nh-C_8 structures. The ferromagnetic state of Fig. 3.12 is induced by the starting magnetization assumed at the beginning of the self-consistent calculation. Technically, we define two fictitiously different atomic species, both with the same chemical nature, but the first one with initially null magnetization, and the second one with a positive initial magnetization. We place these polarized atoms on the

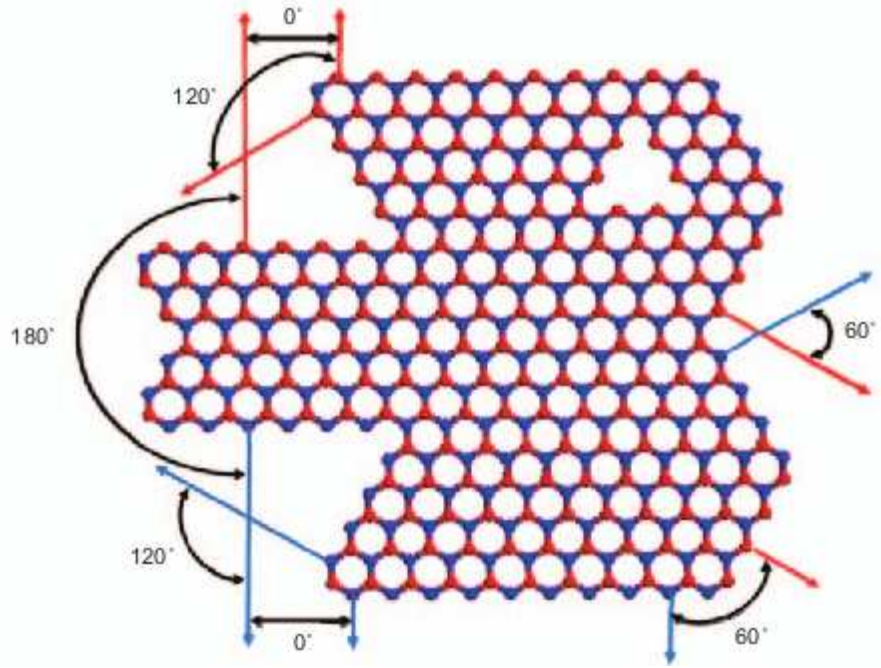


Figure 3.11: Scheme of the geometric relationship between edges in graphene. The edge atoms belong to the same sublattice (in red or in blue) if the zig-zag edges are at an angle of 0° or 120° to each other, but different sublattice if at an angle of 60° or 180° . The angle between edges is defined as the angle between the normal vectors of the edge, from Ref. [32].

zig-zag edges so that the calculation ends up into a ferromagnetic structure. To investigate the possibility of antiferromagnetic or ferrimagnetic structure, we consider three fictitiously different species of carbon, C, CUP, and CDW, with zero, positive, and negative starting magnetization, respectively. Instructed by the computed value of the magnetization of the ferromagnetic case, we take a starting atomic magnetization of $= 1$ Bohr magneton. Figure 3.13 illustrates a possible arrangement of the “bulk”, the C atoms (in blue), and the CUP or the CDW atoms (in red and green) placed along the zig-zag edges.

We perform several self-consistent calculations for the nh-C₆ structure starting from the relaxed positions obtained in the ferromagnetic configuration, but considering different starting magnetizations, as shown in Fig. 3.14. Under each structure, the total and absolute magnetization, M_{tot} and M_{abs} , and the total energy (E_{tot}) are reported. In accordance with the results of Ref. [33], the ground-state configuration, Fig. 3.14(a), has the same magnetization sign for atoms belonging to the same sublattice (there labeled B, C, H, E of Fig. 3.13), while

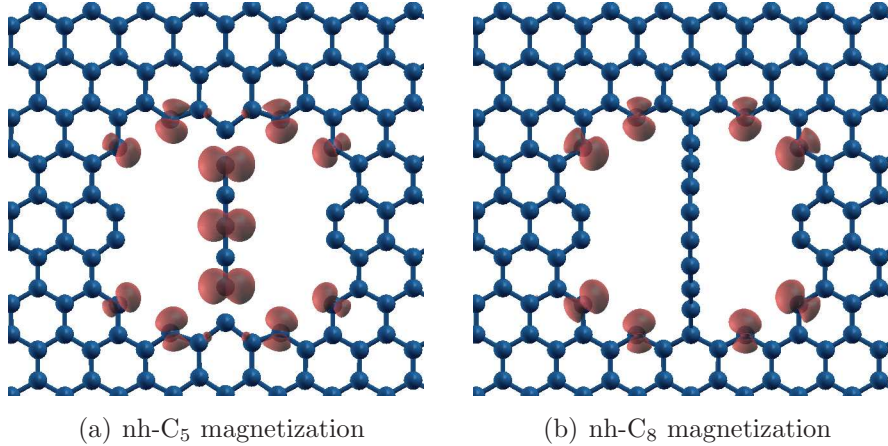


Figure 3.12: Magnetic isosurfaces for the nh-C₅ and the nh-C₈ structures. The value of the isosurfaces equals $0.01 \mu_B/a_0^3$. In this configuration both systems are ferromagnetic.

the sign changes in passing from one sublattice to the other. The edge atoms bonded with the carbyne show little or no magnetism, mainly induced by the ferromagnetic interaction with the other atoms along the zig-zag edge. Low-lying excited states are obtained by changing appropriately the starting magnetizations of selected atoms.

The Ising model can be used to understand how the changes in magnetization translate into energy differences. The model proposed by E. Ising [37] is the simplest model to describe a magnetic structure starting from its elementary constituents; it is defined on a discrete collection of discrete variables (spins). The spins S_i interact in pairs, with energy that acquires one value when the two spins are the same, and a second value when the two spins are different. The energy of the Ising model is defined as:

$$(3) \quad E^{spin} = - \sum_{i \neq j} J_{ij} S_i S_j ,$$

where the sum counts each pair only once and J represents the difference in energy between two different magnetic structures, i.e. the magnetic interaction between two atoms due to spins. According to the values of the absolute magnetization in Fig. 3.14(a), we can assume that each atom has a magnetism equal to 1 Bohr magneton ($M_{abs} \simeq 8$ for 8 atoms that has carry a magnetic moment). For this reason, we must not consider those configurations for which the absolute magnetization happen to be significantly different from 8. It is therefore appropriate to consider a Ising model where spins can take values $1/2$ or $-1/2$. The product $S_i S_j$ is either $1/4$ if the two spins are aligned, or $-1/4$ if they are anti-aligned. For each pair of atoms, if $J_{ij} > 0$, the interaction is ferromagnetic that tends to align spins; if $J_{ij} < 0$,

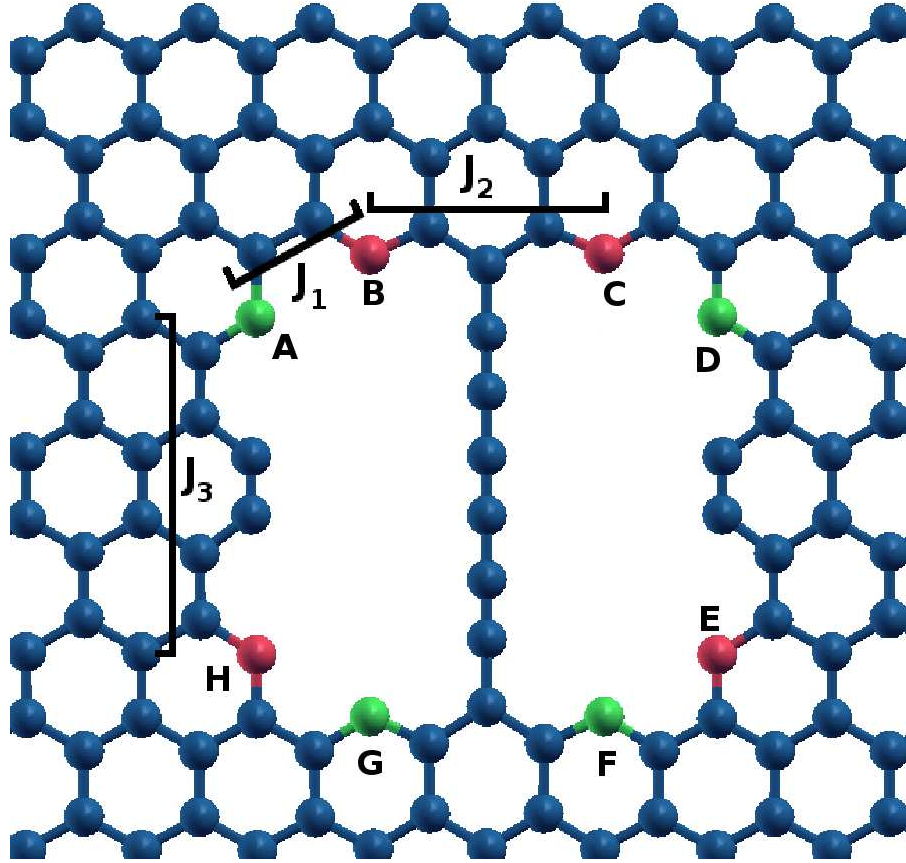
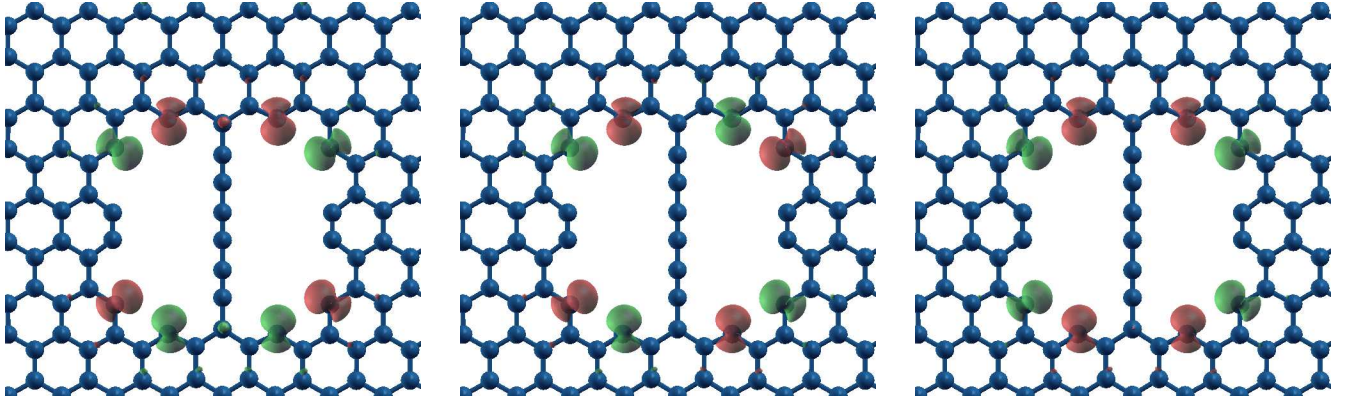


Figure 3.13: In order to obtain magnetic structures different from ferromagnetic one, we consider three fictitious atomic species corresponding to the expected spin polarization: C, CUP, and CDW, with zero, positive and negative starting magnetization, respectively. In our system, the C atoms are in blue, the CUP are red and the CDW are green. The graphs highlight all independent Ising type coupling, J_{ij} , allowed by symmetry and used in Eq. (3), including spin interactions up to first neighbors.

the interaction tends to anti-align the spins (antiferromagnetic interaction). If $J_{ij} = 0$, the spins are non-interacting. We shall assume that spin-spin interactions $J_{ij} = 0$ beyond first neighbors.

We can distinguish 3 different interaction parameters J_{ij} , illustrated in Fig. 3.13: J_1 describes the interactions between spins belonging to atoms of different sublattices ($J_1 = J_{AB} = J_{CD} = J_{EF} = J_{GH}$) rotated by 60° ; J_2 interactions of atoms within the same zig-zag edge ($J_2 = J_{BC} = J_{FG}$), and J_3 interactions across the armchair edge ($J_3 = J_{AH} = J_{DE}$,

(a) *Ground State*

$$E_{tot} = E_{g.s.} = -13947.721 \text{ eV}$$

$$M_{tot} = 0.00$$

$$M_{abs} = 9.00$$

(b) $E_{tot} = E_{g.s.} + 27 \text{ meV}$

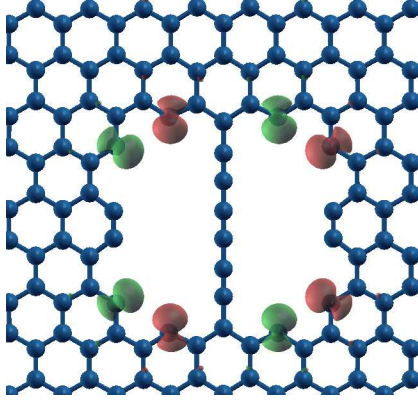
$$M_{tot} = 0.00$$

$$M_{abs} = 7.74$$

(c) $E_{tot} = E_{g.s.} + 36 \text{ meV}$

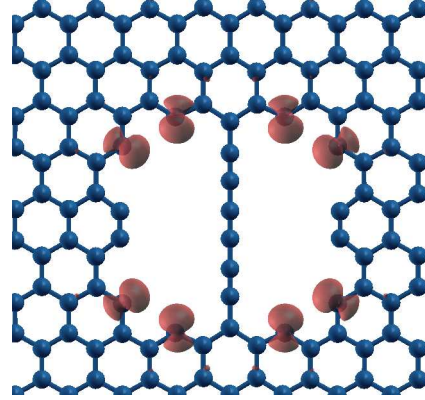
$$M_{tot} = 0.48$$

$$M_{abs} = 7.69$$

(d) $E_{tot} = E_{g.s.} + 36 \text{ meV}$

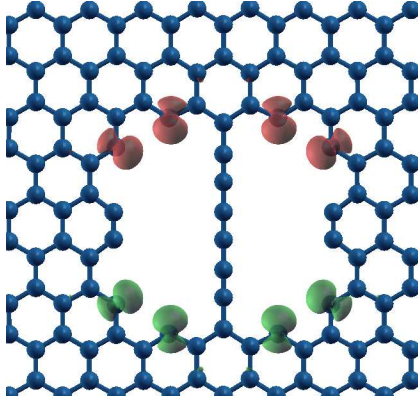
$$M_{tot} = 0.00$$

$$M_{abs} = 7.55$$

(e) $E_{tot} = E_{g.s.} + 595 \text{ meV}$

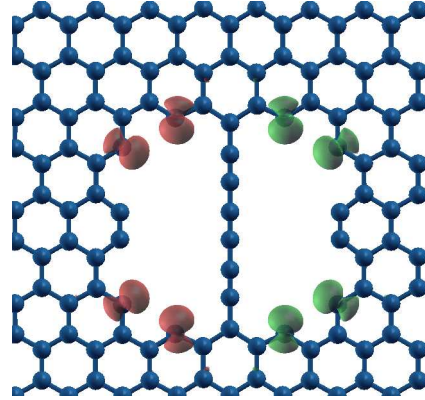
$$M_{tot} = 7.36$$

$$M_{abs} = 7.82$$

(f) $E_{tot} = E_{g.s.} + 692 \text{ meV}$

$$M_{tot} = 0.00$$

$$M_{abs} = 7.57$$

(g) $E_{tot} = E_{g.s.} + 699 \text{ meV}$

$$M_{tot} = 0.00$$

$$M_{abs} = 7.04$$

Figure 3.14: Magnetic isosurfaces of several different nh-C₆ magnetic structures. The ground state is shown in (a), while the others configurations are magnetically excited states. The magnetic isosurfaces are $+0.01 \mu_B/a_0^3$ (red) and $-0.01 \mu_B/a_0^3$ (green).

Parameter	Value [meV]	Standard deviation [meV]
E_0	347	18
J_1	-322	19
J_2	32	35
J_3	11	36

Table 3.2: Summary of the individual parameters of the Ising Model calculated for the nh-C₆ zig configuration.

representing different sublattice rotated by 180°). The energy of a configuration can be written as the sum of the spin energy E^{spin} , Eq. (3), plus E_0 , that represents all other term interactions constructing the total energy. For the nh-C₆ zig structure, we have:

$$\begin{aligned}
 E_{tot} = E_0 + E^{spin} = E_0 & - J_1 (S_A S_B + S_C S_D + S_E S_F + S_G S_H) \\
 & - J_2 (S_B S_C + S_F S_G) \\
 & - J_3 (S_A S_H + S_D S_E) .
 \end{aligned}
 \tag{4}$$

We can evaluate the values of J_{ij} making a linear fit of the energies obtained from Eq. (4). Table 3.2 reports the values of the parameters E_0 and J_{ij} : the value of J_1 indicates that the interaction is antiferromagnetic, while J_2 and J_3 suggest a weakly ferromagnetic interaction. The value of J_1 is one order of magnitude greater than the values of the other J_{ij} . The sign of J_3 disagrees with the prediction of Ref. [33]. As the standard deviation values suggest, due to both the uncertainties in the DFT-LSDA evaluation of the total energy and to the extreme simplification of a model assuming a fixed magnetization amplitude at each site, this method has not sufficient precision to provide a good determination of both J_2 and J_3 . In practice the accuracies of J_2 and J_3 are of the same order of magnitude as the value of the parameters themselves, so that J_2 and J_3 are compatible with zero. in contrast, the values E_0 and J_1 are determined with a sufficient accuracy.

In Fig. 3.15, we compare the energies of the different configurations of Fig. 3.14 obtained by DFT calculation with those obtained using the fitted Ising model. The model can approximate well the effects of the large interaction (J_1), but fails for the fine structure induced by the weaker interactions (J_2 and J_3). Indeed the order of a few levels is inverted passing from DFT to the Ising model. The accuracy bars are the worst prevision of error obtained by the sum of the single parameter's error of Table 3.2. Due to the values of E_0 and J_{ij} calculated using the Ising model, the ground state of the Ising model is different from the one calculated by DFT (and also predicted by Ref. [33]); this indicates that the Ising model eventually fails in considering interactions of the order of 10 meV, while it is successful for

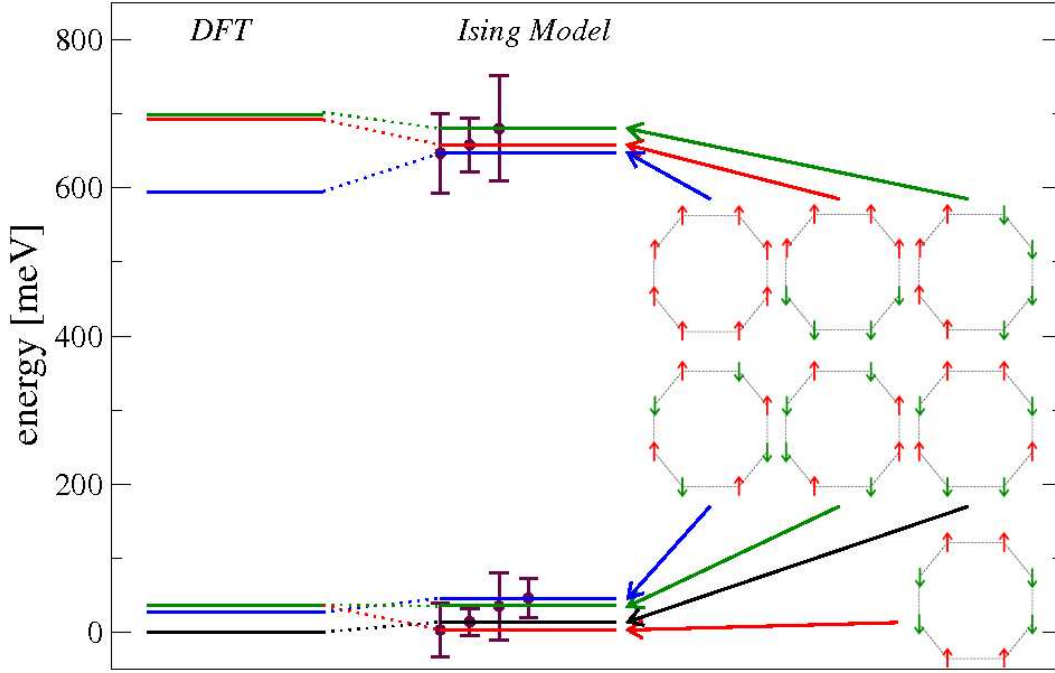


Figure 3.15: Comparison of the energy levels of the magnetic structures of Fig. 3.14 computed using DFT with the values obtained using the Ising model fitted to the DFT values.

interactions of the order of 100 meV. Basically, due to the error bars, the model distinguishes only between two sets of high-lying levels (with parallel J_1 -related spins) and low-lying ones (with antiferro correlations of J_1 -related spins).

A similar analysis could also be done for the odd- n carbynes (e.g. nh-C₅, in Fig. 3.12(a)). Odd- n chains are quite different from the even- n ones, because the former are magnetic. This leads to two consequences: first the number of spin interactions to be considered in a odd-chain is greater, and second the intensities of the spin are different. This would make the possibility to employ an Ising model to understand the data of little significance. Despite these facts, we can search for the magnetic configuration of lower energy. Figure 3.16 shows two different magnetic configuration of the nh-C₇ *straight* structure. The ground state configuration is shown in Fig. 3.16(a). According to Ref. [33], the interaction between the chain and the zig-zag edge (that belong to sublattices rotated by 60°) is antiferromagnetic and is also predominant over J_3 -type one. In this odd- n chain case, the interaction between the *sp*-atoms is ferromagnetic. This is not surprising since all atoms of the chain have magnetization of the same sign. The magnetic energy between the first atom of the carbyne and the nearest atoms of the zig-zag edge is ≈ 70 meV.

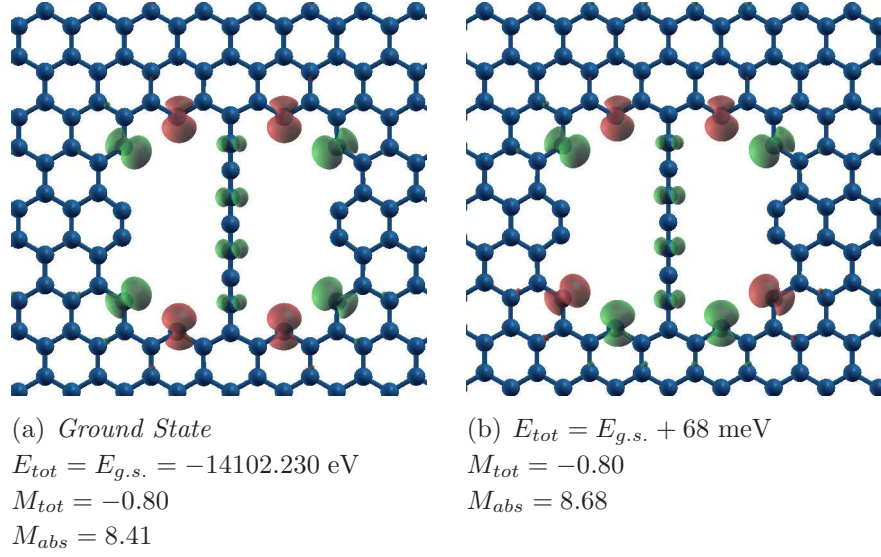


Figure 3.16: Magnetic isosurfaces for the nh-C₇ *straight* structures. The value of isosurfaces is equal to $+0.01 \mu_B/a_0^3$ (red) and $-0.01 \mu_B/a_0^3$ (green).

The empty nanohole displays a behavior similar to that of the even- n carbyne. The atoms involved in the spin interaction, along the zig-zag edges are identified in Fig. 3.17. Like when a even- n chain is present, the atomic magnetization does not change significantly in absolute value from one atom to another and nears $1 \mu_B$. As illustrated in Fig. 3.17, three different first-neighbor interactions need to be considered: two of them represent interaction between two edges belonging to different sublattices (where we expect an anti-ferromagnetic character) and the other describes the interaction between spins of the same sublattice (i.e. ferromagnetic character, according to Ref. [33]). As done above for the nh-C₆ structures, we make a linear fit of all magnetic configurations obtained (shown in Fig. 3.18), to evaluate the values of the J_{ij} and of E_0 . In the Ising model, the total energy is written as:

$$\begin{aligned}
 E_{tot} = E_0 + E^{spin} = E_0 & - J_1 (S_A S_B + S_D S_E + S_F S_G + S_K S_L) \\
 & - J_2 (S_B S_C + S_C S_D + S_G S_H + S_H S_K) \\
 & - J_3 (S_A S_L + S_E S_F) .
 \end{aligned}
 \tag{5}$$

The result of the linear fit is reported in Table 3.3. Like in the nh-C₆, J_1 is one order of magnitude greater than J_2 and J_3 . Also here J_2 and J_3 are compatible with zero. The J_1 interaction is indeed antiferromagnetic and very similar to the one obtained in the calculations with the nh-C₆ structure.

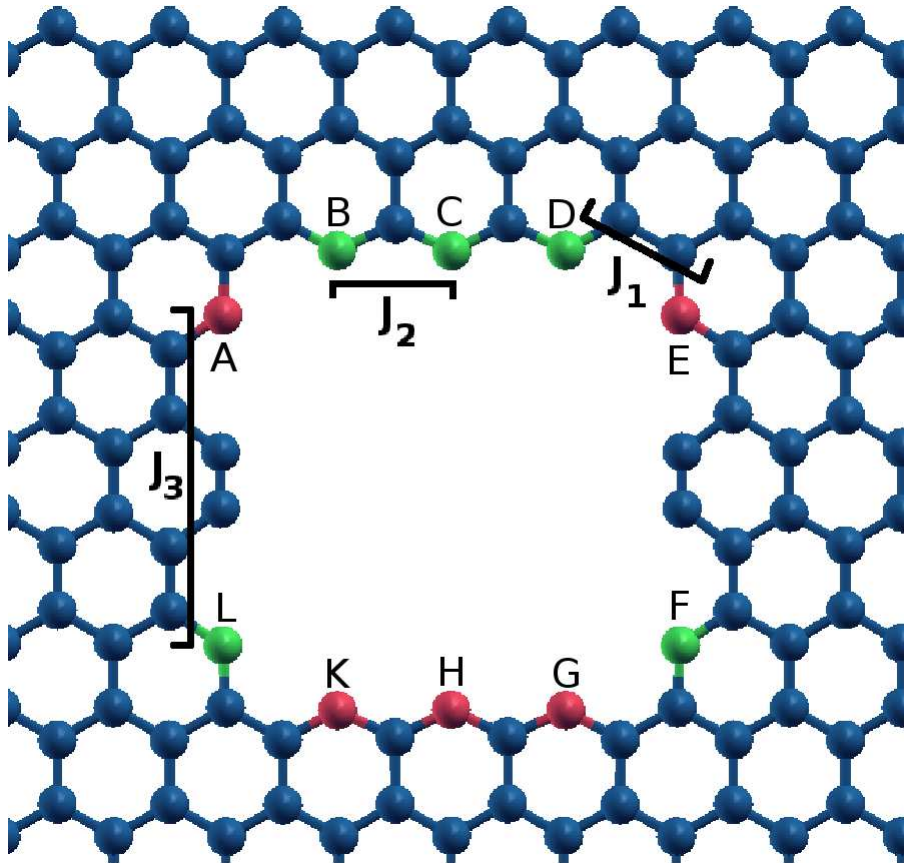
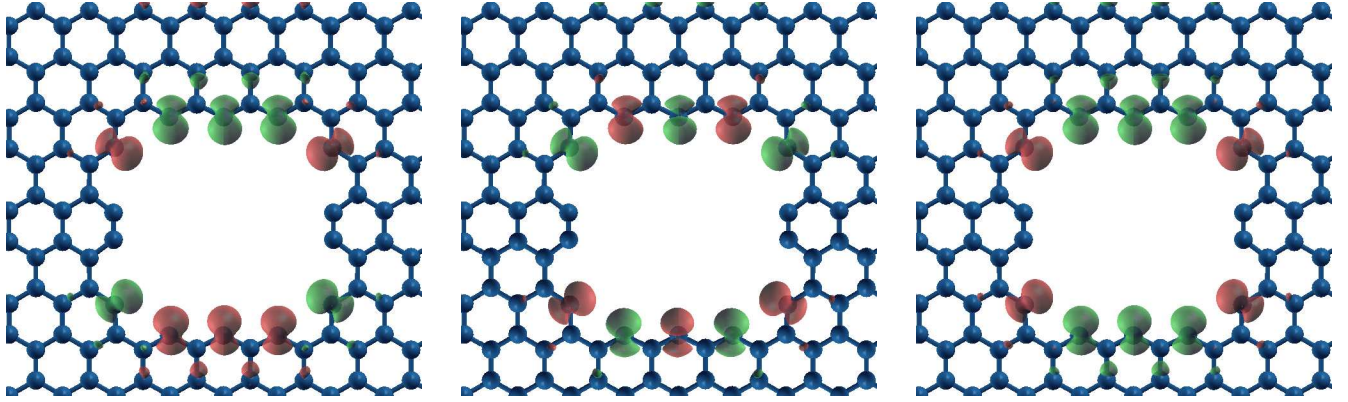


Figure 3.17: Identification of the exchange parameters J_{ij} including interactions up to first neighbors for the unoccupied nh.

Parameter	Value [meV]	Standard deviation [meV]
E_0	307	23
J_1	-270	24
J_2	-12	21
J_3	-30	38

Table 3.3: Summary of the individual parameters of the Ising Model calculated for the nh configuration.

Figure. 3.19 compares the energy levels computed by DFT and those obtained using the fitted Ising model: the same considerations done for the nh-C₆ case apply here.

(a) *Ground State*

$$E_{tot} = E_{g.s.} = -13017.519 \text{ eV}$$

$$M_{tot} = 0.00$$

$$M_{abs} = 11.67$$

(b) $E_{tot} = E_{g.s.} + 46 \text{ meV}$

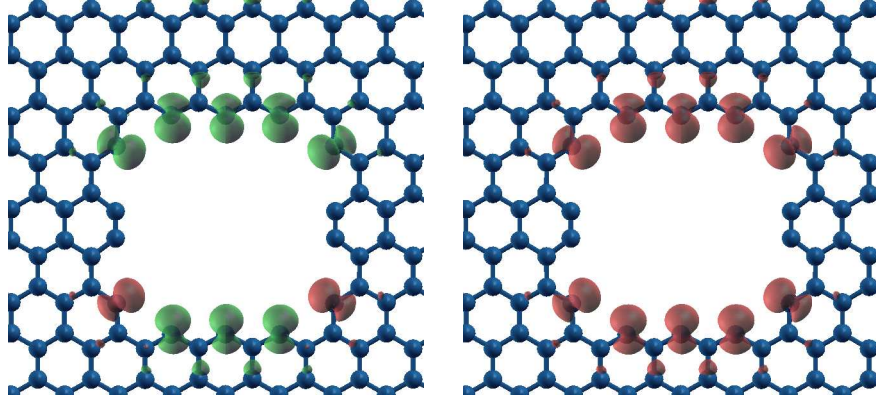
$$M_{tot} = -2.00$$

$$M_{abs} = 10.77$$

(c) $E_{tot} = E_{g.s.} + 82 \text{ meV}$

$$M_{tot} = -2.00$$

$$M_{abs} = 10.71$$

(d) $E_{tot} = E_{g.s.} + 337 \text{ meV}$

$$M_{tot} = -6.00$$

$$M_{abs} = 10.95$$

(e) $E_{tot} = E_{g.s.} + 587 \text{ meV}$

$$M_{tot} = 10.00$$

$$M_{abs} = 10.79$$

Figure 3.18: Magnetic isosurfaces for the nanohole structures. The value of isosurfaces is equal to $+0.01 \mu_B/a_0^3$ (red) and $-0.01 \mu_B/a_0^3$ (green).

3.5. Electronic Properties

In order to investigate the electronic properties of the nanohole-carbyne system, we evaluate the band energies along a path shown in Fig. 3.20(b), starting from Γ , goes in direction perpendicular to the chain towards X and then back to Γ passing from M ; then again parallel to the carbyne until Y and finally back to M . We sample the path in k-space with points at a distance of $1.75 \cdot 10^{-13} \text{ m}^{-1}$.

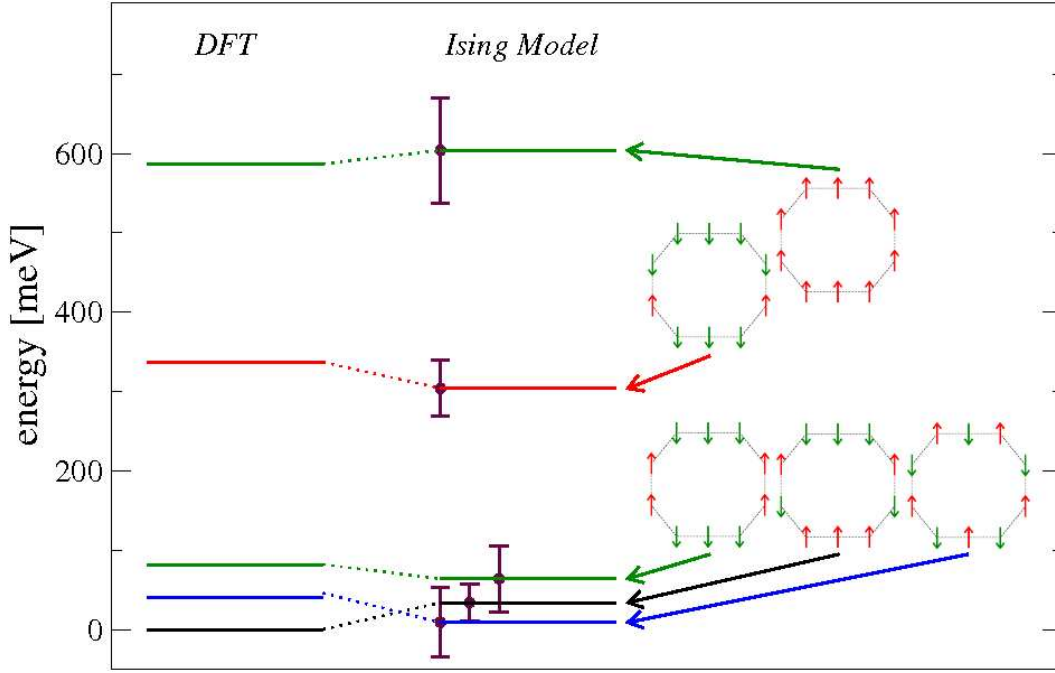


Figure 3.19: Comparison of the energy levels of the structures of Fig. 3.18, as computed using DFT, and as obtained based on the Ising model (Eq. (5)) fitted on the DFT energies of the empty nh.

Figure 3.20(a) shows the band structure for the empty nh superlattice of Fig. 3.7. We have analyzed the spatial distribution of these band states, thus we can identify their character as either

- (1) States localized on the edge of the hole (HB, magenta stars).
- (2) States localized primarily on the bulk-atoms and, due to the reduced dimension of the system, minimally on the edge-atoms (BHB, green squares).

Example of these states are reported in Figs. 3.21(a) and 3.21(b). HB are very flat and dispersionless. Liu *et al.* in Ref. [38], investigating band structures of graphene nanohole, discovered the opening of a band gaps for nanohole with either armchair or zigzag edges. In contrast with that work, we do not find any band gap at Fermi energy (ϵ_F); in fact, we find a metallic band crossing ϵ_F and showing a weakly dispersive pattern approaching the X and Y points.

Figures 3.22, 3.23, 3.24, and 3.25 report the results of analogous bands calculations for the relaxed structures of Figs. 3.9 and 3.10: the magenta stars and the green squares have the same meaning of Fig. 3.20(a). The blue circles indicate states localized mainly on the carbyne atoms (CB, e.g. Fig. 3.21(c)) and the maroon diamonds states localized both on

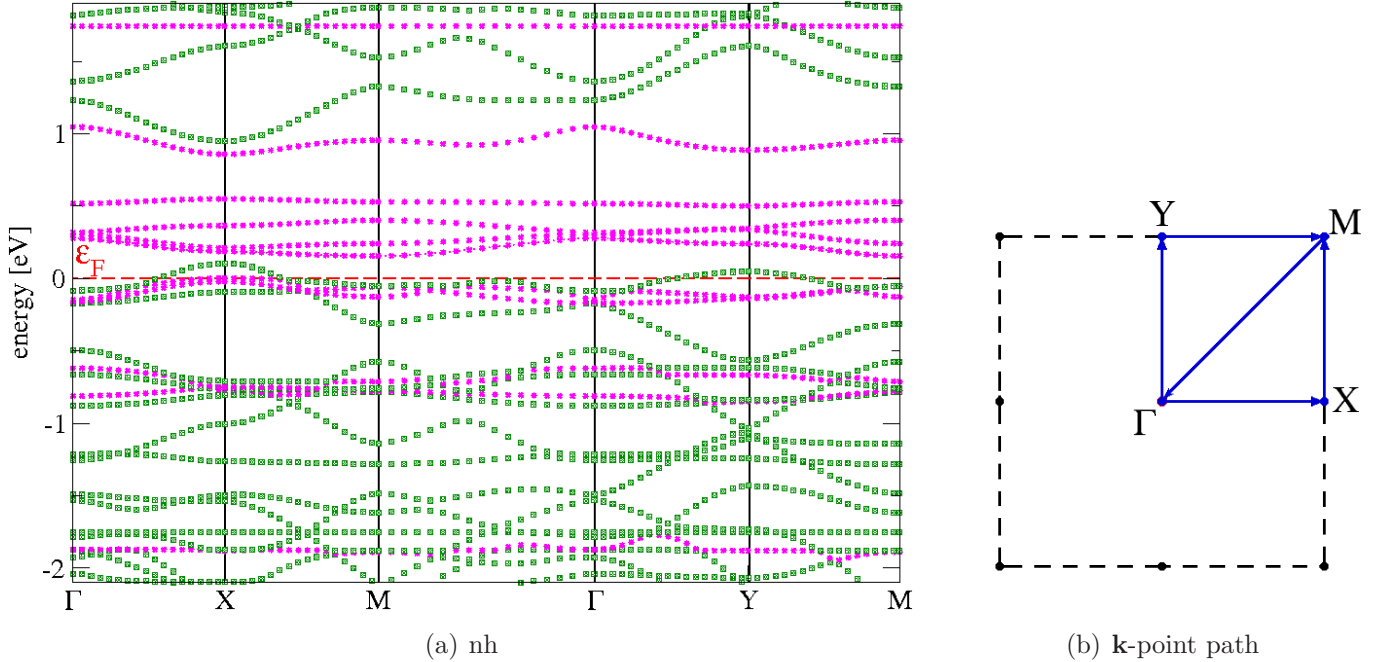


Figure 3.20: (a): Band structure for the majority spin component of the relaxed nh superlattice of Fig. 3.7, in the ferromagnetic configuration of Fig. 3.18(e): magenta stars stand for bands which electronic states are localized on the hole-edge atoms; green squares represent electronic states localized both in the bulk and the edge atoms. The reference energy is taken as the Fermi level (dashed red). (b): \mathbf{k} -point path used in the band structures calculation. This path is followed in all the band-structure calculation of the present section.

the carbyne and on the edge of the hole (CHB, e.g. Fig. 3.21(d)). For all the structures, the HBs are flat, while the other bands show a visible dispersion in energy. Essentially all structures display a metallic behavior due to the CBs that cross the Fermi energy; the nh-C₅ 1*b* has no CB that crosses the Fermi energy due to the fact that the carbyne is bounded to one side only, but the composite system remains metallic thanks to a dispersive band of the graphene. Figures 3.23(a) and 3.23(b) show the band structures of the two spin components of nh-C₆: the deep bands do not display any change neither to the bands for above the Fermi level. The most relevant difference is the upward shift of the HB near ϵ_F by about 0.3 eV.

The only structure that show states localized on the carbyne and on the hole edge is nh-C₆ *arm*. Basically the carbyne, joining the two armchair edges, has insulating character and divides the nh into two smaller ones. Eventually however, even this system is metallic.

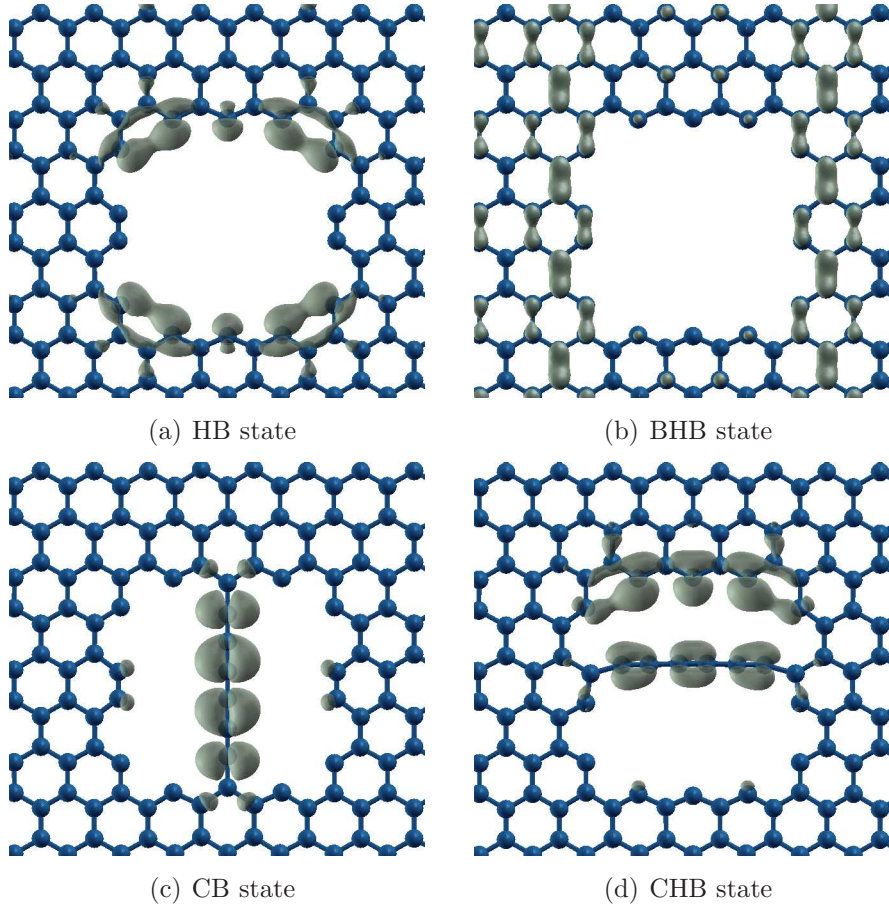


Figure 3.21: Examples of electronic states localized mainly on the edge-atoms (*a*), on the bulk and only weakly on the edge (*b*), mainly on the carbyne (*c*) and partly on the carbyne and on the edge (*d*). For these 4 examples $\mathbf{k} = 0$, and their energy is within ± 2 eV of ϵ_F .

We perform several calculations of the nh-C₇ structure considering different shapes of the carbyne (curved (Fig. 3.9(g)), s-curved (Fig. 3.9(h)), and straight (Fig. 3.9(i))), in fact the length of the hole is only 95% of the length of the isolated chain and this induces different stable shapes of the carbyne: all of them show basically identical band structures (Fig. 3.24(b)), independently from the shape of the chain.

3.6. Vibrational Properties

We perform phonon calculation for some of the relaxed structures of Sect. 3.1. Contrasted to previous vibrational calculations, we use the ultrasoft pseudopotentials which

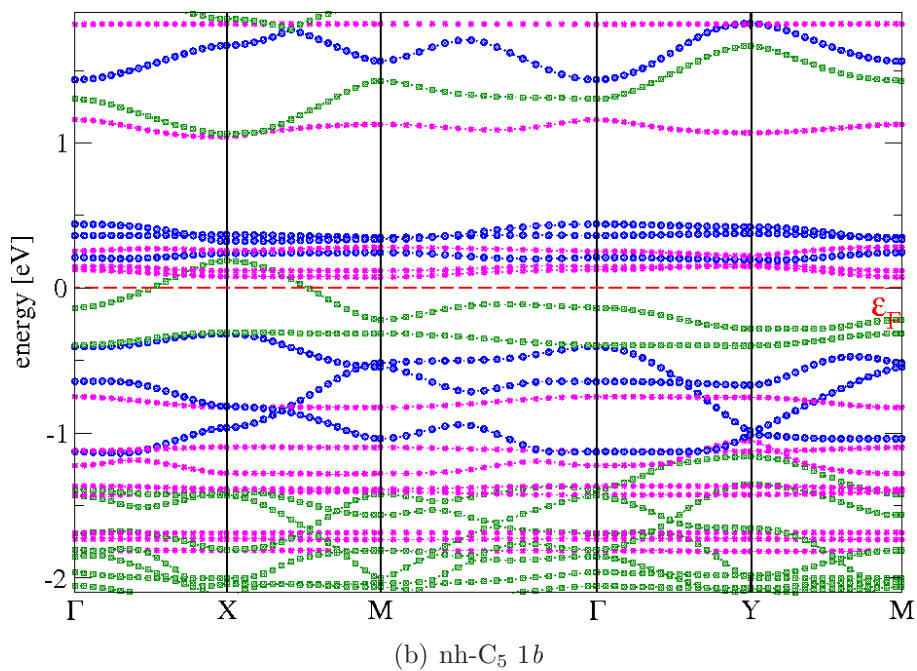
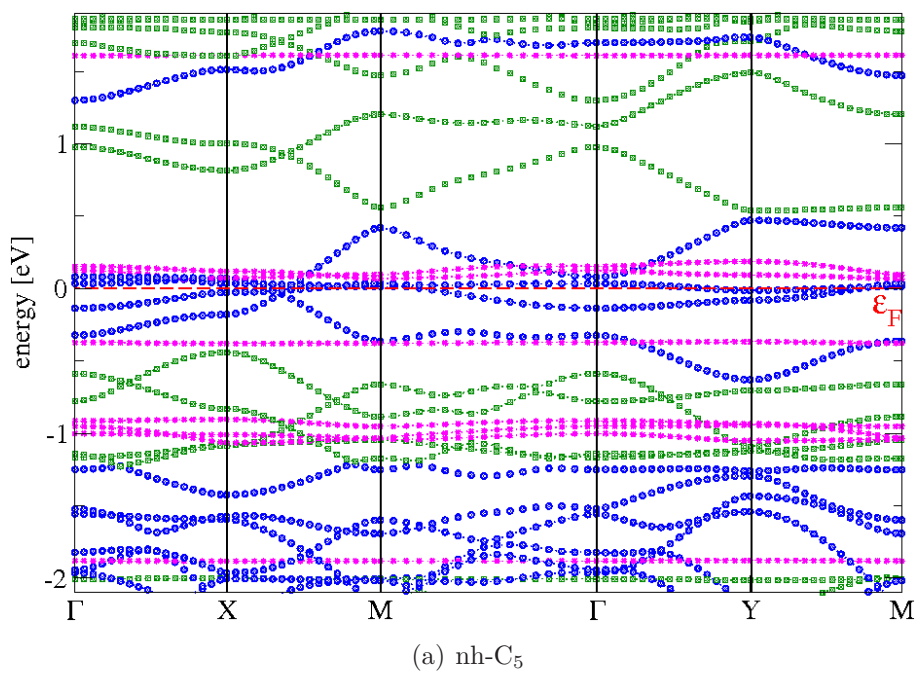


Figure 3.22: Spin-majority band structures of nh-C_5 (Fig. 3.9(a)) and of $\text{nh-C}_5 1b$ (Fig. 3.9(b)).

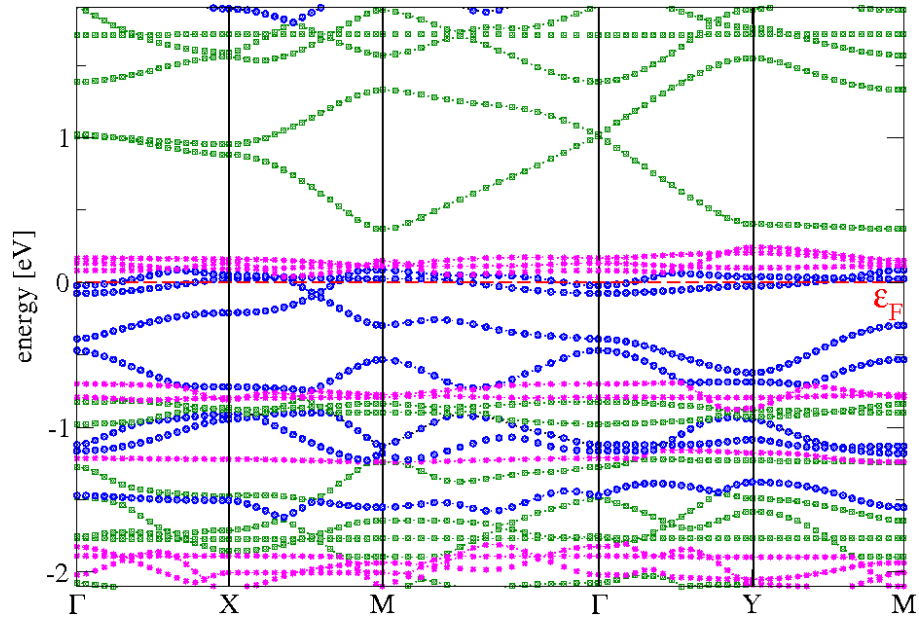
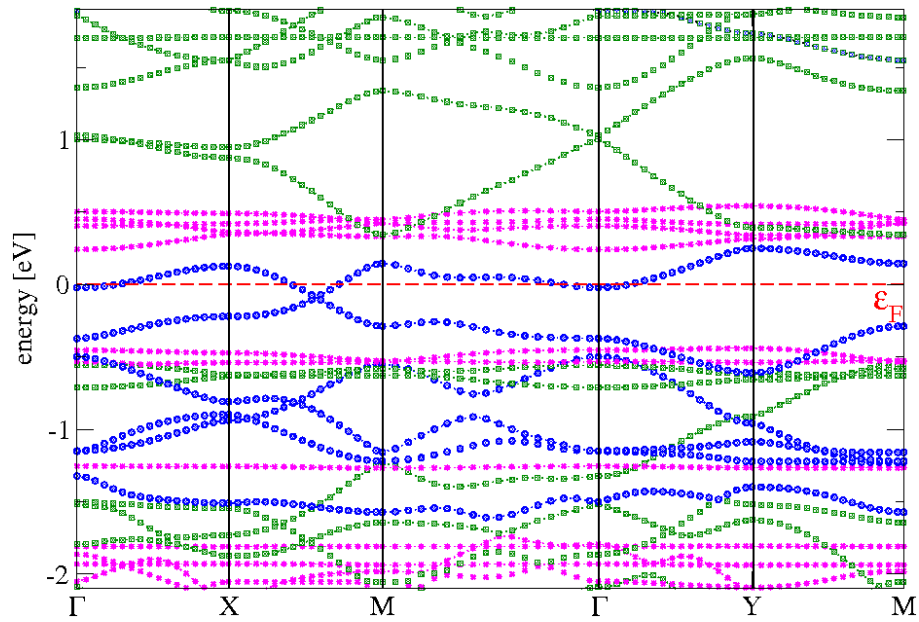
(a) nh-C_6 zig majority spin(b) nh-C_6 zig minority spin

Figure 3.23: Band structures of the majority and minority spin component of nh-C_6 zig (Fig. 3.9(c)).

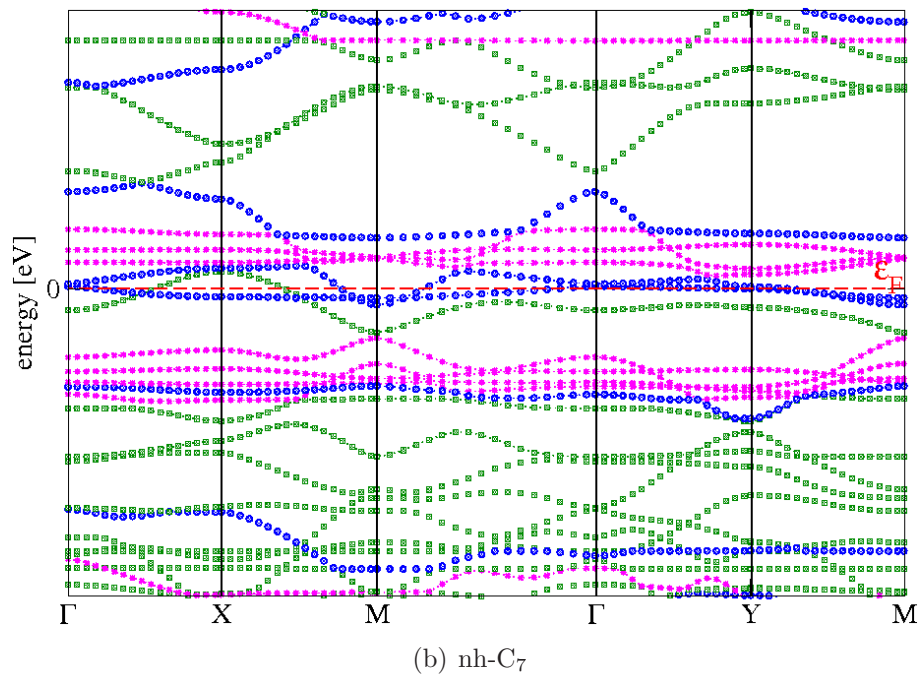
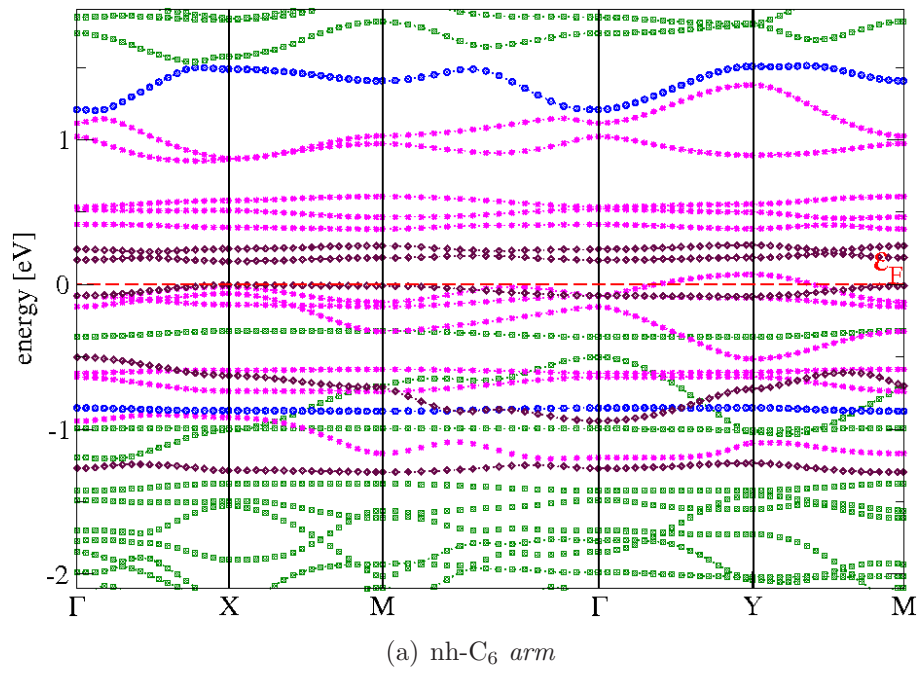


Figure 3.24: Spin-majority band structures of $nh-C_6$ arm (Fig. 3.9(d)) and of $nh-C_7$ (Fig. 3.9(e)).

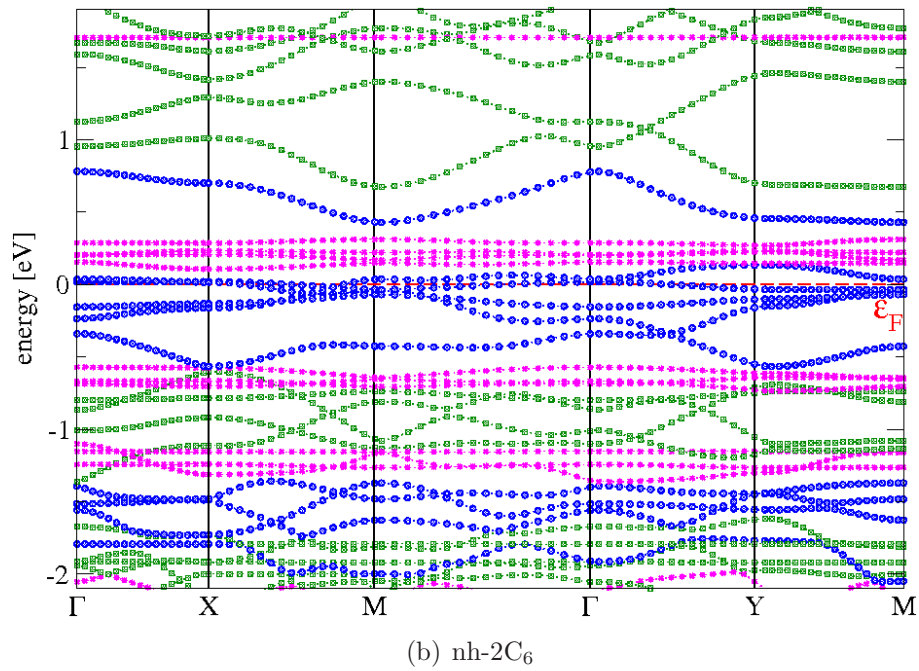
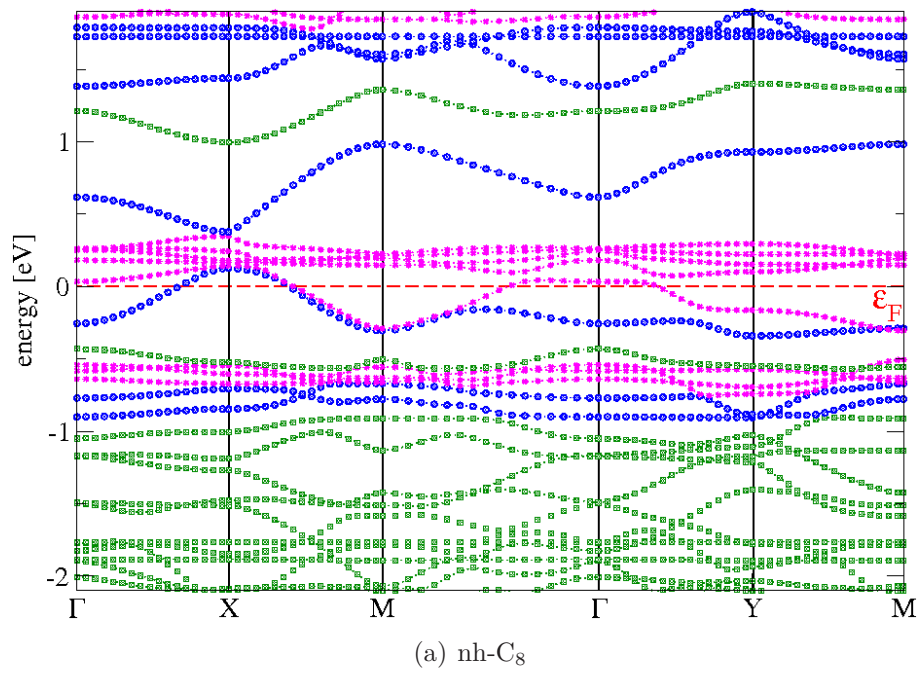


Figure 3.25: Spin-majority band structures of nh-C₈ (Fig. 3.9(f)) and of nh-2C₆ (Fig. 3.10).

Structure name	Raman frequencies [cm^{-1}]	IR frequencies [cm^{-1}]
nh-C ₅	1323, 1368	1332
nh-C ₆ <i>zig</i>	1777, 1878	1939

Table 3.4: Wavenumber of Raman and IR carbyne-frequencies calculated for the nh-C_n structures. The most intense Raman and IR frequencies are in **bold**.

reduces the computational time. For this kind of pseudopotentials the calculation of the Raman tensor is not implemented in adopted code, which means that we could not compute intensities. We include in the construction of the dynamical matrix only a subset of atoms composed of the carbyne and its neighbors up to second. This choice is justified by the results obtained for the Naph₂C₈, and discussed in Sect 2.4.1. Thanks to the characteristic displacement pattern of the most intense Raman and IR frequencies (Fig. 2.15), we can identify them among all the frequencies calculated even without computing the Raman tensor, at least for the even-*n* chain. The calculated frequencies are listed in Table 3.4: the wavenumbers of the frequencies are significantly lower than the characteristic stretching-frequencies of carbyne, whose range is between 1950 and 2300 cm^{-1} . In fact, with respect to a molecule in which the carbyne is free to relax, in a nanohole, the length of the chain is fixed by the distance between the two edges of the hole. In nh-C₅, the length of the chain, including the bonds between the carbyne and the nanohole, is 15% longer than the isolated chain; this elongation leads to frequencies much softer than typical carbyne ones. The length of the chain in nh-C₆ *zig* is only 5% longer than isolated length, and the frequencies are much closer to the typical frequencies of free carbynes.

Unfortunately, we are not able to obtain the values of the different vibrational modes for the curved-carbyne, due to convergency difficulties.

CHAPTER 4

Discussion and Conclusions

The present work collects extensive investigation of the interaction of carbyne chains with sp^2 aromatic or graphitic fragments.

We find that the even- n carbynes terminated with naphthyl groups have a polyynic character, independently from the chain length, with the typical alternation of single/triple bonds. All the chains are fairly stable and the reciprocal orientation of the two ligands does not influence significantly the value of the total energy. The odd- n chains, instead, have a more cumulenic-like character due to frustration of the single/triple bond alternation. The two ligands could be replaced by hydrogens with only a modification of the carbyne energy levels. When the chain is inserted in a nanohole (nh) and binds to zig-zag edge, its polyynic character is somewhat reduced to a value intermediate between cumulenic and polyynic. We predict stabilization energies near 6 eV per bond between each carbyne end and the sp^2 regions.

Odd- n chains exhibit a nonzero magnetization related to a spin triplet state of the π bonds in the molecular state. Magnetism of odd- n chains carries forward to chains inserted in the nh. Even- n chains are instead non-magnetic, and in this context only the magnetic moments of the graphene edge contribute to the magnetism of the nh- C_{2m} .

We compute also the Raman and IR frequencies of even- n chains with special attention to the optical $C\equiv C$ stretching modes which are a characteristic signature of carbynes in the vibrational spectroscopies. The Raman and the IR frequencies have values ranging from 1850 to 2300 cm^{-1} with intensities that increase with the length of the chain, and the frequency of the most intense Raman mode which tends to decrease with n .

The carbynes in the nh display a metallic behavior, with at least one band crossing the Fermi energy.

The possibility of designing graphene-based magnetic nanostructures is particularly intriguing. The capability of arranging the spins inside a carbon structure in a variety of ways, will open the way for the construction of spintronic devices [39]. Possible future applications for the carbynes in interaction with the graphene-type system could be the construction of microchips with ferromagnetic or antiferromagnetic character that can be controlled by nanomanipulation and read out by nanocurrents.

Possible future developments of the present work include extension to a more realistic systems composed by several graphene layers and a nh, and refinement of the magnetic model

for the edge spins using at least second-order neighbors. We should also consider different reciprocal orientation of the carbyne with respect to the nh or different type of chains. A more complete study of the stability, dynamics, configuration charge, etc. of the carbynes should include the analysis of the phononic dynamics outside the linear-response regime, for example by means of Car-Parrinello dynamics. On the molecular side we will study the properties of a carbyne bonded to other sp^2 -fragment terminations.

APPENDIX A

Theory and Implementation

In this chapter, we give an overview of the theory at the base of density functional theory (DFT) [40] and of the computational method used in the present work.

A.1. The Density Functional Theory

Density Functional Theory (DFT) is a ground-state theory in which the relevant physical quantity is the charge density. DFT is highly successful in describing structural and electronic properties in a vast class of materials, from atoms and molecules to crystals and complex systems. Due to its computational simplicity, DFT has become a common tool in first-principles calculations in order to describe properties of molecular and condensed matter systems.

A.1.1. The Hohenberg-Kohn Theorem. Consider a system of N interacting electrons in an external potential $V(\mathbf{r})$, usually the Coulomb potential of nuclei. If the system has a non-degenerate ground state, there is only one ground-state charge density $\rho(\mathbf{r})$ that correspond to a given $V(\mathbf{r})$. In 1964 Hohenberg and Kohn [41] demonstrated that there is only one external potential $V(\mathbf{r})$ that yields a given ground-state charge density $n(\mathbf{r})$.

(i) First HK Theorem: Given an interaction between electrons U_{ee} , the external potential $V_{ext}(\mathbf{r})$, and hence the total energy, is a unique functional of the electron density $\rho(\mathbf{r})$. The electronic density determines all ground-state (GS) properties, like the kinetic energy $T[\rho(\mathbf{r})]$, the potential energy $V[\rho(\mathbf{r})] = U_{ee}[\rho(\mathbf{r})] + V_{ext}[\rho(\mathbf{r})]$, and the total energy:

$$(6) \quad E[\rho(\mathbf{r})] = V_{ext}[\rho(\mathbf{r})] + T[\rho(\mathbf{r})] + U_{ee}[\rho(\mathbf{r})] = \int \rho(\mathbf{r}) V_{ext}(\mathbf{r}) d\mathbf{r} + F_{HK}[\rho(\mathbf{r})] ,$$

where $F_{HK}[\rho(\mathbf{r})]$ is a universal functional, called Hohenberg-Kohn functional, which depends only on the density and which form is not dependent on the particular system considered.

(ii) Second HK Theorem: The GS energy is minimized by the GS charge density. Accordingly, DFT reduces the N -body problem to the determination of a 3-dimensional function $\rho(\mathbf{r})$ which minimizes the functional $E[\rho(\mathbf{r})]$. Unfortunately, the $F_{HK}[\rho(\mathbf{r})]$ part of the functional is unknown in its exact form.

A.1.2. The Kohn-Sham Equations. In 1965, Kohn and Sham (KS) reformulated the problem and opened the way to practical applications of DFT. They solve the problem

by considering a system of interacting electrons mapped on to an auxiliary system of non-interacting electrons having the same GS charge density $\rho(\mathbf{r})$. The kinetic energy of the non-interacting system does not differ too much from the kinetic energy of the interacting system. For a system of non-interacting electrons, the GS charge density is representable as a sum over one-electron orbitals (the KS orbitals) $\psi_i(\mathbf{r})$

$$(7) \quad \rho(\mathbf{r}) = 2 \sum_i |\psi_i(\mathbf{r})|^2 ,$$

where i runs from 1 to $N/2$ if we assume double occupancy of all states, and the kinetic energy is simply given by

$$(8) \quad T_s[\rho(\mathbf{r})] = -\frac{\hbar^2}{2m} 2 \sum_i \int \psi_i^*(\mathbf{r}) \nabla^2 \psi_i(\mathbf{r}) d\mathbf{r} .$$

The KS orbitals are the solutions of the Schrödinger equation

$$(9) \quad \left(-\frac{\hbar^2}{2m} \nabla^2 + V_{KS}(\mathbf{r}) \right) \psi_i(\mathbf{r}) = \epsilon_i \psi_i(\mathbf{r}) ,$$

where m is the mass of the electron and they obey to the orthonormality constraint:

$$(10) \quad \int \psi_i^*(\mathbf{r}) \psi_j(\mathbf{r}) d\mathbf{r} = \delta_{ij} .$$

The existence of a unique potential $V_{KS}(\mathbf{r})$ with $\rho(\mathbf{r})$ as its GS charge density is a consequence of the HK theorem, which holds independently of the form of the electron-electron interaction U_{ee} .

The problem of determining $V_{KS}(\mathbf{r})$ for a given $\rho(\mathbf{r})$ is solved by considering the variational property of the energy (second HK theorem). The functional derivative with respect to ψ_i^* of the functional

$$(11) \quad E' = E - \sum_{ij} \lambda_{ij} \left(\int \psi_i^*(\mathbf{r}) \psi_j(\mathbf{r}) d\mathbf{r} - \delta_{ij} \right) ,$$

where λ_{ij} are Lagrange multipliers, must vanish:

$$(12) \quad \frac{\delta E'}{\delta \psi_i^*(\mathbf{r})} = \frac{\delta E'}{\delta \psi_i(\mathbf{r})} = 0 .$$

The energy functional can be written as follows:

$$(13) \quad E = T_s[\rho(\mathbf{r})] + E_H[\rho(\mathbf{r})] + E_{xc}[\rho(\mathbf{r})] + \int \rho(\mathbf{r}) V(\mathbf{r}) d\mathbf{r} ,$$

where the first term is the kinetic energy of non-interacting electrons (Eq. (8)); the second term is the so called Hartree energy, that describes the mean-field electrostatic interaction

between the electronic cloud of charge and itself:

$$(14) \quad E_H [\rho(\mathbf{r})] = \frac{e^2}{2} \int \frac{\rho(\mathbf{r}) \rho(\mathbf{r}')}{|\mathbf{r} - \mathbf{r}'|} d\mathbf{r} d\mathbf{r}' ;$$

the third term, the exchange-correlation energy, contains all remaining terms, whose precise form is presently unknown. Taking into account that

$$(15) \quad \frac{\delta \rho(\mathbf{r})}{\delta \psi_i^*(\mathbf{r}')} = \psi_i(\mathbf{r}) \delta(\mathbf{r} - \mathbf{r}') ,$$

we can compute the functional derivatives of each term appearing in the energy functional (Eq. 13), finding:

$$(16) \quad \frac{\delta T_s}{\delta \psi_i^*(\mathbf{r})} = -\frac{\hbar^2}{2m} 2 \sum_i \nabla^2 \psi_i(\mathbf{r}) ,$$

$$(17) \quad \frac{\delta E_H}{\delta \psi_i^*(\mathbf{r})} = e^2 \int \frac{\rho(\mathbf{r}')}{|\mathbf{r} - \mathbf{r}'|} \psi_i(\mathbf{r}) d\mathbf{r}' ,$$

and

$$(18) \quad \left(-\frac{\hbar^2}{2m} \nabla^2 + V_H(\mathbf{r}) + V_{xc}[\rho(\mathbf{r})] + V(\mathbf{r}) \right) \psi_i(\mathbf{r}) = \sum_j \lambda_{ij} \psi_j(\mathbf{r}) ,$$

where

$$(19) \quad V_H(\mathbf{r}) = e^2 \int \frac{\rho(\mathbf{r}')}{|\mathbf{r} - \mathbf{r}'|} d\mathbf{r}' \quad \text{and}$$

$$(20) \quad V_{xc}[\rho(\mathbf{r})] = \frac{\delta E_{xc}}{\delta \rho(\mathbf{r})}$$

are the Hartree and the exchange-correlation potentials, respectively.

After a little math, the KS equations take the form:

$$(21) \quad (H_{KS} - \epsilon_i) \psi_i(\mathbf{r}) = 0 ,$$

where $\lambda_{ij} = \delta_{ij} \epsilon_j$ and the KS Hamiltonian, H_{KS} , is defined as

$$(22) \quad H_{KS} = -\frac{\hbar^2}{2m} \nabla^2 + V_H(\mathbf{r}) + V_{xc}(\mathbf{r}) + V(\mathbf{r}) \equiv -\frac{\hbar^2}{2m} \nabla^2 + V_{KS}(\mathbf{r})$$

and is related to the functional derivative of energy:

$$(23) \quad \frac{\delta E}{\delta \psi_i^*(\mathbf{r})} = H_{KS} \psi_i(\mathbf{r}) .$$

A.1.3. The Local Density Approximation. The KS equations are very similar to the Hartree-Fock (HF) ones. In fact, both are derived from a variational principle: the minimization of the DFT energy functional for the former, of the average energy for a single Slater determinant wave-function for the latter. While the HF equations are derived starting from an approximation (that is taking the total electron wave-function as a Slater determinant), until now we made no assumption in the KS derivation.

One of the most used approximations for the exchange-correlation potential, introduced by Kohn and Sham, is the Local Density Approximation (LDA). They approximate the functional for exchange-correlation energy, $E_{xc}[\rho(\mathbf{r})]$, with a function of the local density $\rho(\mathbf{r})$:

$$(24) \quad E_{xc}[\rho(\mathbf{r})] = \int \epsilon_{xc}(\rho(\mathbf{r})) \rho(\mathbf{r}) d\mathbf{r} ,$$

with

$$(25) \quad \frac{\delta E_{xc}}{\delta \rho(\mathbf{r})} = \mu_{xc}(\rho(\mathbf{r})) = \left(\epsilon_{xc}(\rho) + \frac{d\epsilon_{xc}}{d\rho} \right)_{\rho=\rho(\mathbf{r})} ,$$

and for $\epsilon_{xc}(\rho)$ is used the same dependence on the density as for the homogeneous electron gas (jellium model) for which $\rho(\mathbf{r})$ is constant.

A.1.4. The Local Spin Density Approximation. Up to now the KS equations has been considered independent of spin. DFT can be extended to calculate GS properties of spin-polarized system: the electronic density is split into two parts polarized in opposite way, $\rho = \rho_{\uparrow} + \rho_{\downarrow}$, and the energy is a functional of both these components, $E = E(\rho_{\uparrow}, \rho_{\downarrow})$. We study collinear system and perturbations with magnetic fields oriented only along the z -axis, thus we consider only the diagonal terms of the spin-density matrix. In Local Spin Density Approximation (LSDA), the exchange-correlation potential can be written

$$(26) \quad V_{xc}^{LSDA} = \int \rho(\mathbf{r}) \epsilon_{xc}[\rho_{\uparrow}(\mathbf{r}), \rho_{\downarrow}(\mathbf{r})] d\mathbf{r} ,$$

where ϵ_{xc} is the exchange and correlation energy of the homogeneous electron gas at density $(\rho_{\uparrow}, \rho_{\downarrow})$. The relative polarization can be defined as:

$$(27) \quad \zeta = \frac{\rho_{\uparrow} - \rho_{\downarrow}}{\rho} ;$$

if $\zeta = 1$, all spins are oriented along the same direction and the system is completely polarized; if $\zeta = 0$, the spins are equally oriented along up and down directions and the system is non-magnetic.

A.1.5. The Plane-Wave Basis Set. The KS equations are solved in a self-consistent way: starting from an input density, the KS Hamiltonian is generated, and the KS equations are solved. The cycle stops if the eigen-energies and the eigen-values satisfy some convergence criteria, otherwise the outputs are considered as inputs for a new cycle, and the procedure is repeated until convergence is achieved. We need to represent in some way the KS orbitals. For example, (i) one can represent them on a real space grid or (ii) by expansion on a basis set. In the latter case, atomic-centered functions (e.g. Gaussian or atomic orbitals) have been tried, but functions that are independent of the atomic positions (e.g. plane waves, as we are going to describe here) have a few advantages, in particular that the Hilbert space span by the basis is independent of the atomic positions.

The plane-wave basis is especially suited in a periodic context, like a crystalline solid. It is less apt to describe molecules and clusters, but this can be done in a repeated-supercell geometry, by placing sufficient vacuum around the finite object. Thanks to Bloch's theorem, independent electron states in a periodic system can be written as the product of a periodic function times a plane wave:

$$(28) \quad \psi_{\mathbf{k}}(\mathbf{r}) = e^{i\mathbf{k}\cdot\mathbf{r}} u_{\mathbf{k}}(\mathbf{r}) ,$$

where $u_{\mathbf{k}}(\mathbf{r} + \mathbf{R}) = u_{\mathbf{k}}(\mathbf{r})$, if \mathbf{R} is a direct lattice vector. Since every $e^{i\mathbf{G}\cdot\mathbf{r}}$ has the lattice periodicity (\mathbf{G} is a reciprocal lattice vector), the vector \mathbf{k} in the reciprocal space can be defined modulus the closest \mathbf{G} vector, and it can be confined to the first Brillouin zone of the system. The KS equation for a given electronic state j are:

$$(29) \quad \hat{H}_{KS} \psi_{\mathbf{k}}(\mathbf{r}) = \left[-\frac{\hbar^2}{2m} \nabla^2 + V_{KS}(\mathbf{r}) \right] e^{i\mathbf{k}\cdot\mathbf{r}} u_{\mathbf{k}}(\mathbf{r}) = \epsilon_{\mathbf{K}} e^{i\mathbf{k}\cdot\mathbf{r}} u_{\mathbf{k}}(\mathbf{r}) .$$

For every \mathbf{k} , there is a complete set of functions $u_{\mathbf{k}}$; the dependence of $\epsilon_{\mathbf{K}}$ on \mathbf{k} defines the electron bands of the system. We can expand the functions $u_{\mathbf{k}}$ on a plane waves basis set $\phi_{\mathbf{k}}$:

$$(30) \quad \phi_{\mathbf{k}} = \frac{1}{\sqrt{\Omega}} e^{i\mathbf{G}\cdot\mathbf{r}} , \quad \langle \phi_{\mathbf{G}} | \phi_{\mathbf{G}'} \rangle = \delta_{\mathbf{G}\mathbf{G}'}$$

$$(31) \quad \psi_{\mathbf{k}}(\mathbf{r}) = \frac{e^{i\mathbf{k}\cdot\mathbf{r}}}{\sqrt{\Omega}} \sum_{\mathbf{G}} c_{\mathbf{k},\mathbf{G}} e^{i\mathbf{G}\cdot\mathbf{r}} ,$$

where the $c_{\mathbf{k},\mathbf{G}}$ are the plane-wave coefficients. The kinetic energy and the potential can be written:

$$(32) \quad T_{\mathbf{G},\mathbf{G}'}^{\mathbf{k}} = -\frac{\hbar^2}{2m} \langle \phi_{\mathbf{G}} | \phi_{\mathbf{G}'} \rangle = \frac{\hbar^2}{2m} |\mathbf{k} + \mathbf{G}| \delta_{\mathbf{G}\mathbf{G}'} \quad \text{and}$$

$$(33) \quad \langle \phi_{\mathbf{G}} | V_{KS}(\mathbf{r}) | \phi_{\mathbf{G}'} \rangle = \frac{1}{\Omega} \int V_{KS}(\mathbf{r}) e^{i(\mathbf{G}-\mathbf{G}')\cdot\mathbf{r}} d\mathbf{r} = \tilde{V}_{KS}(\mathbf{G} - \mathbf{G}') ,$$

where $\tilde{V}_{KS}(\mathbf{G} - \mathbf{G}')$ is the Fourier transform of the potential $V_{KS}(\mathbf{r})$. The KS equations reduce to the eigen-value problem:

$$(34) \quad \sum_{\mathbf{G}'} \left[\frac{\hbar^2}{2m} |\mathbf{k} + \mathbf{G}| \delta_{\mathbf{G}\mathbf{G}'} + \tilde{V}_{KS}(\mathbf{G} - \mathbf{G}') \right] c_{n\mathbf{k},\mathbf{G}^{\text{prime}}} = \epsilon_{n\mathbf{k}} c_{n\mathbf{k}} ,$$

where n is the band index. In the calculations, the sum over \mathbf{G} has to be truncated up to a given cutoff:

$$(35) \quad \frac{\hbar^2}{2m} |\mathbf{k} + \mathbf{G}|^2 \leq E_{cut} ,$$

where E_{cut} is the kinetic-energy cutoff.

A.1.6. The Pseudopotentials. The pseudopotentials (PPs) is an effective potential constructed to replace the singular atomic all-electron potential. Core states do not contribute in a significant manner to chemical bonding and to solid-state properties. Only outer (valence) electrons do, while core electron are frozen in their atomic state. For many purposes one can safely ignore changes in core states (frozen core approximation). PPs have been widely used in solid state physics starting from the 1960s. Modern PPs are called norm-conserving. These are atomic potentials which are devised so as to mimic the scattering properties of the true atom. For a given reference atomic configuration, a norm-conserving PP must fulfill the following condition: (i) all-electron and pseudo-wavefunctions must have the same energy; (ii) they must be the same beyond a given core radius r_c , which is usually located around the outermost maximum of the atomic wave function; (iii) the pseudo-charge and the true charge contained in the region $r < r_c$ must be the same. Norm-conserving PPs are relatively smooth functions, whose long-range tail goes like $Z_v e^2 / r$ where Z_v is the number of valence electrons. They are nonlocal because it is usually impossible to mimic the effect of orthogonalization to core states on different angular momenta l with a single function. PPs are equivalent to the frozen core approximation: PP and all-electron calculations on the same systems yield almost indistinguishable results (except for those cases in which core states are not sufficiently frozen).

A.1.7. The Success and Failures of DFT. DFT-LDA is computationally much simpler than HF. The best results are obtained for solids, whose structural and vibrational properties are well described [42, 43]: the correct crystal structure is usually found to have the lower energy; bond length, phonon frequencies are accurate within a few percent. The accuracy of LDA is considered satisfactory in condensed-matter system, but it is much less so in atomic and molecular physics (highly inhomogeneous systems for which an approximation based on the homogeneous electron gas would hardly be appropriate) LDA overestimates (up to $\approx 20\%$ and more) cohesive energies and bond strengths in molecule and solids, and as a consequence bond lengths are often underestimated [44, 45]. These problems are sometimes

corrected by the introduction of gradient approximations [46]: the exchange-correlation functional is written as a function of the local density and of the local gradient of the density. This is the simplest extension of LDA to inhomogeneous systems. Generalized Gradient Approximations (GGA) functionals yield much better atomic energies and binding energies than LDA, at a modest computational cost; in particular they yield a good description of the Hydrogen bond.

Since the LDA has functionals based on the local density and on its local derivative, the weak Van der Waals (VdW) interactions are absent by construction, due to their non-local character. VdW-bonded systems can be better studied with classical molecular dynamics and interatomic potentials. To solve this problem, there are two kinds of approaches: adding semi-empirical VdW interactions, or using a nonlocal exchange-correlation functional accounting for VdW interactions [47, 48]. The former is computationally much heavier, but it may become soon a viable option.

Simple DFT approximations often fail in strongly correlated materials, whose contain localized, atomic-like electron states, typically originating from d or f atomic states, together with delocalized, band-like states originating from s and p orbitals: LDA and GGA may produce an incorrect occupancy of the localized states (less localized), leading to an incorrect description of the properties of the material under study. The solutions can be to add a Coulomb repulsion term, U , responsible for the behavior of highly correlated materials, to a DFT-LDA calculation (LDA+U) [49] or the use of hybrid functionals, containing a mixture of HF exchange. The former approach is computationally cheap but not rigorous, the latter is expensive in solids.

Some errors in simple DFT comes from self-interaction (the interaction of an electron with the field it generates) [50, 51]. Self-interaction cancels by construction in HF; in DFT, self-interaction affects finite systems, or systems containing localized electrons, while its effects vanishes for delocalized electron states in solids.

Due to the failure of KS band gaps (energies difference between HOMO and LUMO states) to reproduce carefully the true band gap in solids, gaps in DFT are significantly underestimate (up to 50%) [52]. In finite systems ionization potentials and electron affinities can be calculated as energy difference between the ground state and a state with one electron added or removed; in extended systems this is not possible. The reason for this problem lies in the dependence of the exact energy functional upon the number of electrons and in the inability of approximate functionals to reproduce it.

A.2. The Application DFT in the Present Work

To study our carbon compounds, we use the QUANTUM ESPRESSO package [53], in particular to compute relaxed structures, band structures or molecular levels, and vibrational properties. To depict the optimized atomic structures we use the XCRYSDEN package [54].

A.2.1. The Naphthyl Termination. In this Section, we describe the computational method used for study the properties of the naphthyl group bonded to a carbyne. We compute relaxed geometries, using the adiabatic potential based on ultrasoft pseudopotentials (RRKJUSpp, C.pz-rrkjus.UPF and H.pz-rrkjus.UPF for carbon and hydrogen, respectively [53]), for which a relatively low cutoff for the wave function/charge density of 30/240 Ry is sufficient. We also use numerically more expensive norm-conserving pseudopotentials (VBCpp, C.pz-vbc.UPF and H.pz-vbc.UPF [53], with a wave function/charge cutoff of 60/240 Ry) to compute the matrix of Raman coefficients, using second order response [55] from phonons [56, 57], because the Quantum Espresso implementation for ultrasoft pseudopotentials is still missing.

For all these isolated-molecule calculations, we consider a single \mathbf{k} -point placed at Γ . We relax all atomic positions until the forces and energy difference drop below 10^{-4} Ry/ a_0 and 10^{-5} Ry, respectively; the self-consistent cycle used to compute the electronic structure stops after the total adiabatic energy is converged to better than 10^{-9} Ry. To prevent convergence problems for the molecular geometries where the HOMO-LUMO gap becomes small or vanishes, we occupy the molecular orbitals (MO) using a Gaussian smearing of the occupancies of 3 meV, which is completely irrelevant in the common situation of a molecular gap exceeding 0.1 eV. Periodic boundary conditions are implied in a plane-waves geometry. Accordingly, we study isolated molecule in a repeated-cell geometry, making sure that at least 1 nm of vacuum separate periodic images in each direction, in order to make the reciprocal interaction between the periodic images negligible. Numerical details are similar to those validated and used, e.g., in Ref. [21].

According to the general rule of leaving 1 nm of vacuum around the molecule, we consider different sizes of the cell containing the molecule. The cell size has no effect on structural and electronic properties, but it could influence the determination of the frequencies of vibrational modes and their intensity. To solve this question, we consider a simpler molecule, such as C_2H_4 , Fig. A.1. We consider three different sizes of the box, with increasing vacuum space between the molecule and its periodic image from 1 nm to 2 nm. Figure A.2 shows the wavenumbers and the related intensities for both the Raman and the Infrared (IR) frequency of C_2H_4 : no evidence of significant shift of frequency or modification in its intensity is seen while changing the size of the supercell. These results permit us to compare the vibrational frequencies and intensities of the dinaphthyl-polyynes molecules (Sect. 2.4) of different length, thus simulated in supercells of different size using the 1 nm rule as the only recipe for the choice of the all size.

A.2.2. The Graphene Termination. All DFT-LDA calculations, presented in Chap. 3, use an energy cutoff of 240 Ry for charge density and potential and of 30 Ry for wavefunctions and a $5 \times 5 \times 1$ Γ -centered \mathbf{k} -point mesh to span the electron bands in the graphene

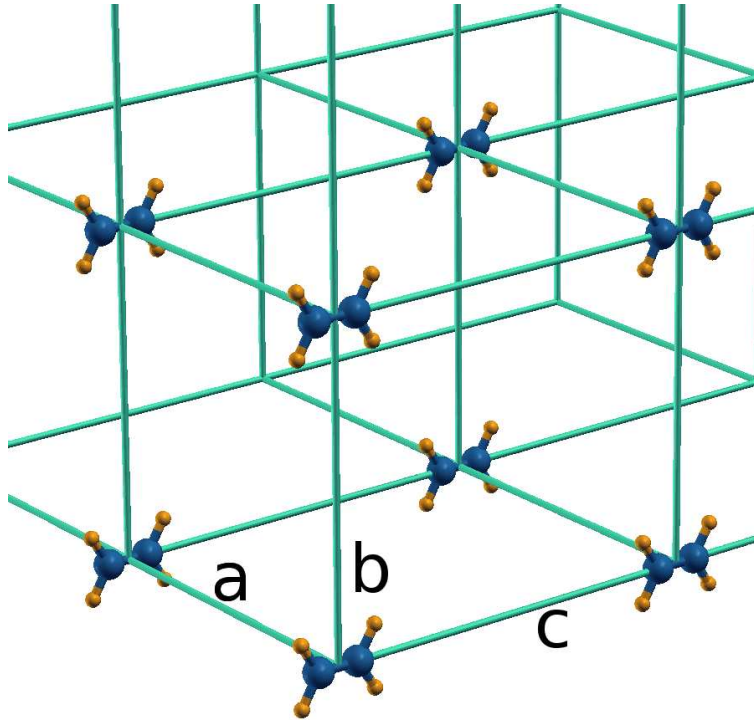


Figure A.1: Repeated-cell geometry, illustrated for calculations of molecule of C_2H_4 .

plane. BZ integrations in these metallic systems are performed using a $2 \cdot 10^{-4}$ Ry wide Gaussian smearing of the occupations. We relax all atomic positions until the residual-forces drop below 10^{-4} Ry/ a_0 . Each self-consistent electronic-structure calculation stops when the total energy changes by less than 10^{-8} Ry. We perform all the calculations using the adiabatic potential based on ultrasoft pseudopotentials (RRKJUSpp). Periodic boundary conditions are implemented in all directions in the Quantum Espresso package: like for the molecules the slab supercell considered has 1 nm of vacuum along the z -axis in order to ensure that the interaction between periodic images of the graphene sheet is negligible. A complete graphene plane supercell consist of 7×4 rectangular conventional unit cells of four carbon atoms, as shown in Fig. A.3. In total each complete graphene layer within one supercell consist of 112 atoms. We have selected this cell size as a fair compromise insuring fairly small interaction between the copies of the nanohole in the supercell repetitions, with reasonable computer time.

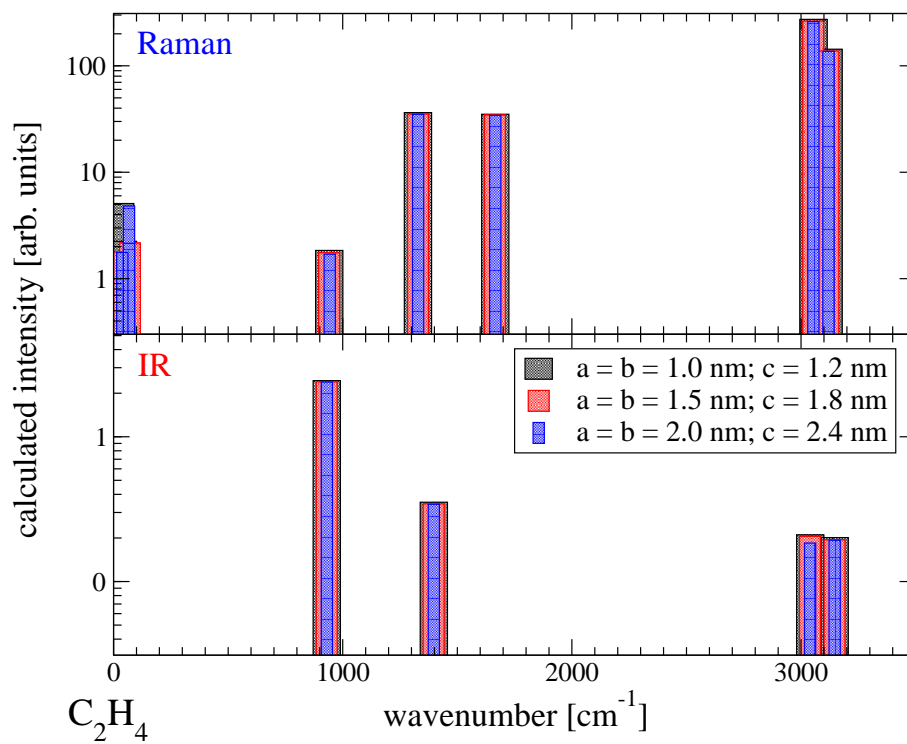


Figure A.2: Calculated intensity of Raman and IR frequencies for the C_2H_4 molecule. The intensities are calculated for different sizes of supercell; a , b , and c are the lengths of each side of the supercell as shown in Fig. A.1.

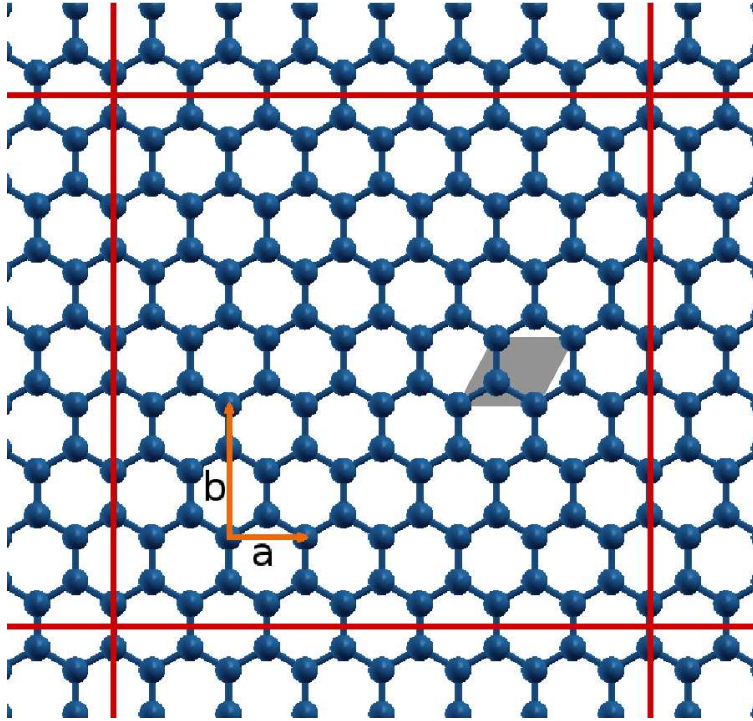


Figure A.3: The adopted slab supercell of graphene composed of 7×4 rectangular unit cells of four atoms corresponding to 56 2-atom primitive cells of graphene. In solid orange the unit vectors of the rectangular unit cell: $a = 244$ pm and $b = 422$ pm. The size of the supercell (highlighted in solid red) in the $x - y$ plane is 1714 pm \times 1690 pm. One primitive cell is in grey.

APPENDIX B

The Magnetization of Carbynes with Other Terminations

The simplest termination for a carbyne is hydrogen. The BLA for C_6H_2 is equal to 12 pm, typical of polyynic carbyne with complete single/triple bonds alternation. The C_7H_2

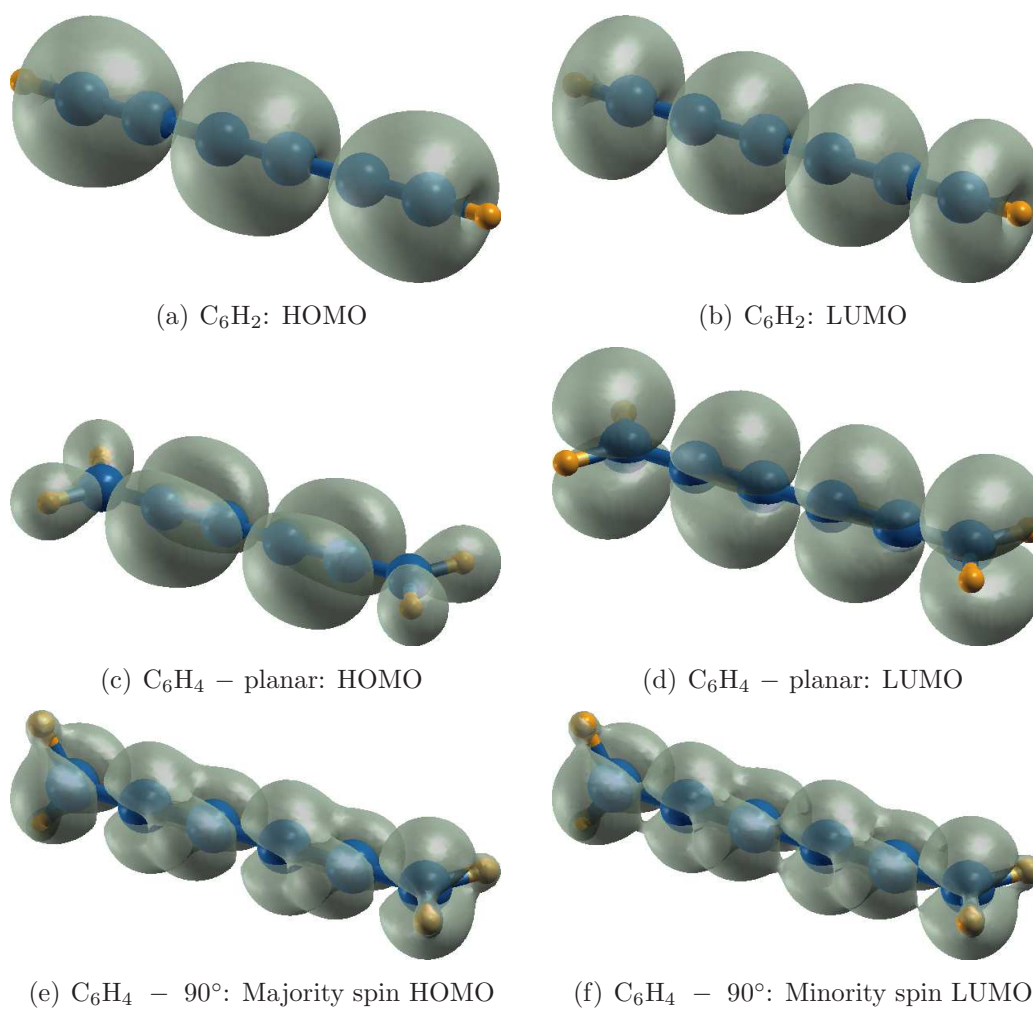


Figure B.1: HOMO and LUMO for the $n = 6$ polyynic (*a,b*) and cumulenic (*c – f*) chains in the contexts listed in Table B.1.

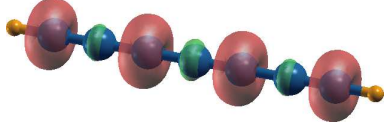
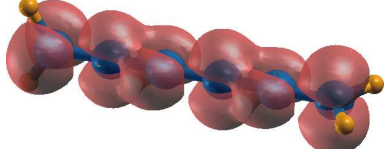
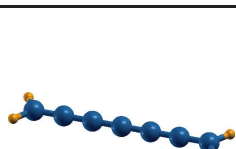
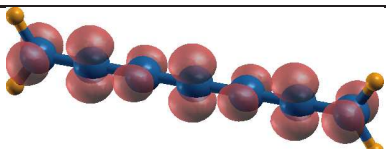
Structure	Name	E_{Tot} [eV]	M_{Tot} [μ_B]	M_{Abs} [μ_B]	Magn. structure
	C_6H_2	0.0	0.0	0.00	—
	C_7H_2	0.0	2.0	2.57	
	C_6H_4 planar	0.0	0.0	0.00	—
	C_6H_4 90°	1.2	2.0	2.04	
	C_7H_4 90°	0.0	0.0	0.00	—
	C_7H_4 planar	1.1	2.0	2.04	

Table B.1: Structure and magnetic properties of carbynes terminated with H and H_2 . The total magnetization is the integral of the magnetization in the cell: $M_{tot} = \int (n_\uparrow - n_\downarrow) d^3r$; the absolute magnetization is the integral of the absolute value of the magnetization in the cell: $M_{abs} = \int |n_\uparrow - n_\downarrow| d^3r$. The odd- n polyynic chain (e.g. C_7H_2), the even- n cumulenenic twisted (e.g. $C_6H_4 - 90^\circ$) and the odd- n cumulenenic planar carbynes ($C_7H_4 - \text{planar}$) are $S = 1$ magnetic, while the other cases are not. For those geometries which are unstable saddle points, we report the excess total energy.

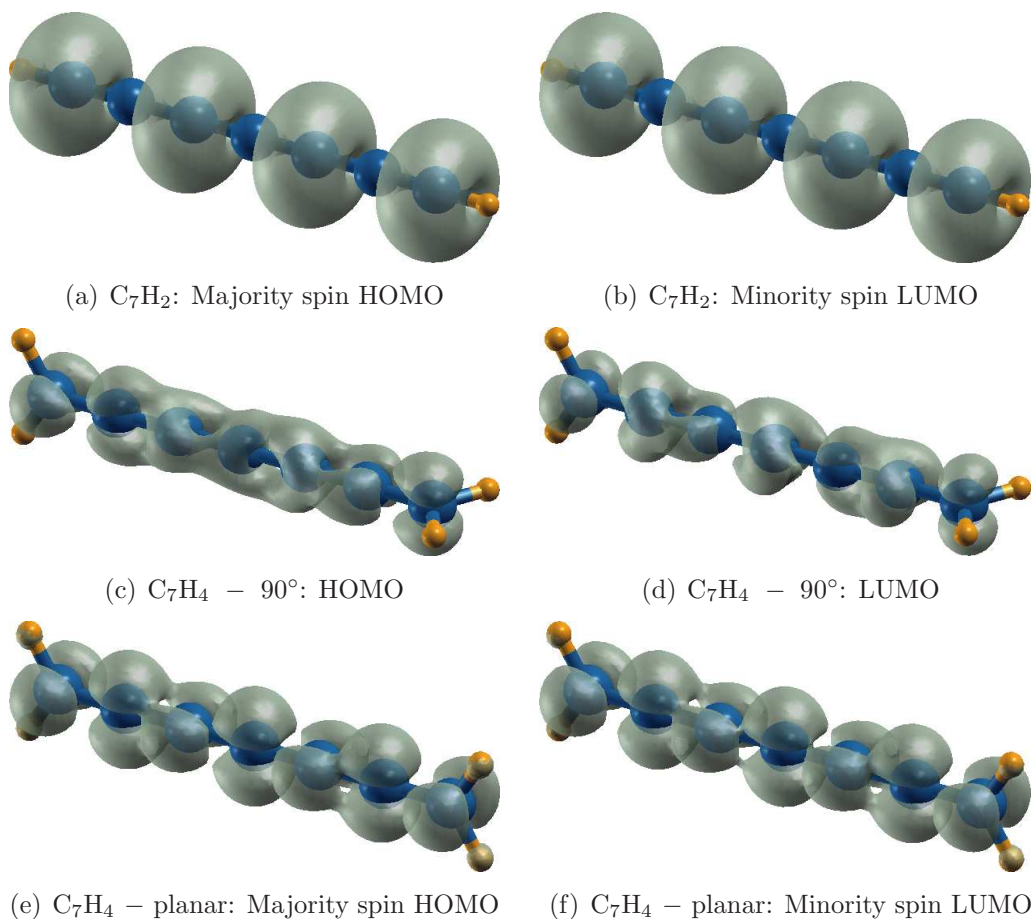


Figure B.2: HOMO and LUMO for a odd- n chain in the context listed in Table B.1. These states are all twofold degenerate or quasi-degenerate.

molecule has a BLA more characteristic of cumulenic-like chain (equals 6 pm): the bonds at the middle of the chain are double leaving two electrons free to move in a degenerate π orbital delocalized along the chain; according to Table B.1, the positive magnetization is localized mainly around the odd-index atoms, while we find a weak negative magnetism around the even-position atoms. The majority-spin HOMO and the minority-spin LUMO of C_7H_2 (Figs. B.2(a) and B.2(b)) are equal and the isovalues correspond to the place where the magnetization concentrates. The HOMO and LUMO of non-magnetic C_6H_2 (Figs. B.1(a) and B.1(b)) are placed on the triple and on the single bonds, respectively.

Consider, for comparison, a termination composed of two hydrogens: these chains have cumulenic behavior ($BLA \leq 4$ pm). In the even- n chains, when the equilibrium terminations

are co-planar, the HOMO electronic levels are in the same plane of the molecule in correspondence of triple bonds (Fig. B.1(c)), while the LUMO ones are in the orthogonal plane in correspondence of single bonds (Fig. B.1(d)); the number of levels occupied is the same for both spin components, and this leads to the non magnetic character of the molecule. The same molecule, but 90° twisted, has an energy greater of about 1.2 eV with respect to the ground-state (GS) planar configuration [21]. The spin components levels disaligned and the spin majority HOMO is orbitally essentially the same wavefunctions the minority LUMO. The charge density of these levels localizes near the atoms of the chain in alternating planes perpendicular to the chain direction (like the magnetization shown in Table B.1). The odd- n chain relaxes in the twisted configuration (the total energy difference between the twisted and planar configurations equals 1.1 eV): the electronic levels are in alternating planes perpendicular to the chain direction either in the twisted configuration (that is non-magnetic, Figs. B.2(c) and B.2(d)) or in the planar one (that is magnetic, Figs. B.2(e) and B.2(f)). The GS has the levels of both spin components occupied in the same way, while we find two degenerate or quasi-degenerate extra orbitals occupied only by the majority-spin components in the planar configuration which is then an $S = 1$ state.

We consider also even- n and odd- n carbynes terminated by a phenyl group (Ph) and by a protonated phenyl in order to break the aromatic ring (PPh). According to Sect. 2.1, the nature of a carbyne (cumulene or polyynes) depends on the bond order and length between the carbyne and the termination (BL0). For the diphenyl-carbynes, BL0 equals 139 pm, typical of a single bond: the carbyne shows a polyynic behavior. The chain has properties close to those of the hydrogen terminated chain (Table B.1): the even- n chain is non-magnetic, while the odd- n chain is magnetic independently of the reciprocal orientation of the two phenyl groups.

We conclude that a fully aromatic group behaves essentially as a H, and only forms a single bond to the carbyne. To check this we break the aromaticity of the phenyl circle by adding an extra hydrogen on the third carbon: the carbyne now shows a cumulenic behavior and acts as if the terminations had been replaced by two hydrogens at each end of the chain. Double bonds form. Thus, as shown in Table B.1, an even-planar molecule is non-magnetic, as well as an odd-torched ones; an even-twisted molecule and an odd-planar ones are magnetic.

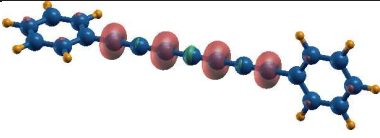
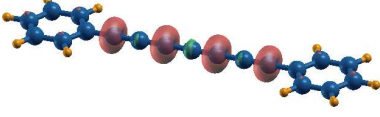
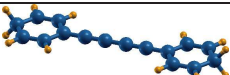
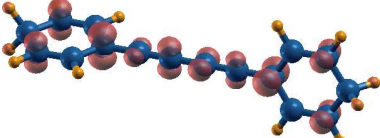
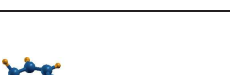
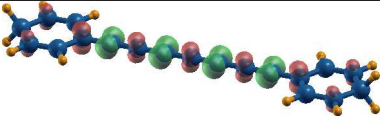
Structure	Name	E_{Tot} [eV]	M_{Tot} [μ_B]	M_{Abs} [μ_B]	Magn. structure
	C ₄ Ph planar	0.0	0.0	0.00	—
	C ₄ Ph 90°	0.01	0.0	0.00	—
	C ₇ Ph 90°	0.0	2.0	2.64	
	C ₇ Ph planar	0.006	2.0	2.62	
	C ₄ PPh planar	0.0	0.0	0.00	—
	C ₄ PPh 90°	0.8	2.0	2.27	
	C ₇ PPh 90°	0.0	0.0	0.00	—
	C ₇ PPh planar	0.6	0.0	2.70	

Table B.2: Structure and magnetic properties of carbynes terminated by a phenyl group (Ph) and by a protonated phenylic group (PPh). All magnetic configurations are spin triplets. For those geometries which are unstable saddle points we report the excess total energy. Due to the aromatic properties of the termination, the diphenyl-carbyne, like the dinaphthyl-carbyne, is a polyyne and its properties are similar to those of the H-terminated carbyne. Adding an hydrogen to the phenyl ring, the aromaticity breaks and the termination acts more like an H₂.

Bibliography

- [1] Y. Ralchenko, A. E. Kramida, J. Reader, and NIST ASD Team (2008), *NIST Atomic Spectra Database*. <http://physics.nist.gov/asd3>. National Institute of Standards and Technology, Gaithersburg, MD.
- [2] A. El Goresy and G. Donnay, *Science* **161**, 363 (1968).
- [3] F. P. Bundy, W. A. Bassett, M. S. Weathers, R. J. Hemley, H. K. Mao, and A. F. Goncharov, *Carbon* **34**, 141 (1996).
- [4] H. Kroto, *Carbon* **30**, 1139 (1992).
- [5] W. W. Duley, and A. Hu, *The Astrophysical Journal* **698**, 808 (2009).
- [6] F. Cataldo, *Tetrahedron Lett.* **45**, 141 (2004).
- [7] C. Jin, H. Lan, L. Peng, K. Suenaga, and S. Iijima, *Phys. Rev. Lett.* **102**, 205501 (2009).
- [8] H. Matsuda, H. Nakanishi, and M. Kato, *J. Polym. Lett. Ed.* **22**, 107 (1984).
- [9] Y. P. Kudryavtsev, *Progress of Polymer Chemistry*, 87, Nauka (Moscow, 1969).
- [10] F. Cataldo, D. Capitani, *Materials Chem. Phys.* **59**, 225 (1999).
- [11] M. Tsuji, S. Kuboyama, T. Matsuzaki, and T. Tsuji, *Carbon* **41**, 2141 (2003).
- [12] K. Yamada, H. Kunishige, and A. B. Sawaoka, *Naturwiss* **78**, 450 (1991).
- [13] R. B. Heimann, *et al.*, *Carbyne and Carbynoid Structures*, Kluwer Academic Publishers (Dordrecht, Boston, London, 1999).
- [14] L. Ravagnan, F. Siviero, C. Lenardi, P. Piseri, E. Barborini, and P. Milani, *Phys. Rev. Lett.* **89**, 285506 (2002).
- [15] F. Cataldo, *Polyynes: Synthesis, Properties, and Applications*, Taylor and Francis Group, (Boca Raton, 2006).
- [16] M. Kijima, T. Toyabe, and H. Shirakawa, *Chem. Commun.*, 2273 (1996).
- [17] K. Ohmura, M. Kijima, and H. Shirakawa, *Synth. Metals* **84**, 417 (1997).
- [18] M. Kijima, *Recent Res. Devel. Pure Appl. Chem.* **1**, 27 (1997).
- [19] W. E. Pickett, *Comput. Phys. Rep.* **9**, 115 (1989).
- [20] M. J. Rice, A. R. Bishop, and D. K. Campbell, *Phys. Rev. Lett.* **51**, 2136 (1983).
- [21] L. Ravagnan, N. Manini, E. Cinquanta, G. Onida, D. Sangalli, C. Motta, M. Devetta, A. Bordoni, P. Piseri, and P. Milani, *Phys. Rev. Lett.* **102**, 245502 (2009).
- [22] M. Weimer, W. Hieringer, F. Della Sala, and A. Gorling, *Chem. Phys.* **309**, 77 (2005).
- [23] W. A. Chalifoux, R. R. Tykwinski, *C. R. Chimie* **12**, 341 (2009).
- [24] F. Cataldo, Private communication.
- [25] L. Ravagnan, P. Piseri, M. Bruzzi, S. Miglio, G. Bongiorno, A. Baserga, C. S. Casari, A. Li Bassi, C. Lenardi, Y. Yamaguchi, T. Wakabayashi, C. E. Bottani, and P. Milani, *Phys. Rev. Lett.* **98**, 216103 (2007).
- [26] A. C. Ferrari, J. Robertson, *Phys. Rev. B* **61**, 14095 (2000).
- [27] V. V. Berdyugin, Yu. P. Kudryavtsev, S. E. Evsyukov, Yu. V. Korshak, P. P. Shorygin, and V. V. Korshak., *Dokl. Akad. Nauk SSSR* **305**, 362 (1989).

- [28] K. Akagi, Y. Furukawa, I. Harada, M. Nishiguchi, and H. Shirakawa, *Synth. Met.* **17**, 557 (1987).
- [29] I. Kinoshita, M. Kijima, and H. Shirakawa, *Macromol. Rapid Commun.* **21**, 1205 (2000).
- [30] H. Tabata, M. Fujii, S. Hayashi, T. Doi, and T. Wakabayashi, *Carbon* **44**, 3168 (2006).
- [31] X. F. Fan, L. Liu, J. Y. Lin, Z. X. Shen, and J. L. Kuo, *ACS Nano* **3**, 3788 (2009).
- [32] D. Yu, E. M. Lupton, M. Liu, W. Liu, and F. Liu, *Nano Res.* **1**, 56 (2008). Online supplementary.
- [33] D. Yu, E. M. Lupton, M. Liu, W. Liu, and F. Liu, *Nano Res.* **1**, 56 (2008).
- [34] M. Fujita, K. Wakabayashi, K. Nakada, and K. Kusakabe, *J. Phys. Soc. Jpn.* **65**, 1920 (1996).
- [35] O. V. Yazyev, and M. I. Katsnelson, *Phys. Rev. Lett.* **100**, 047209 (2008).
- [36] K. Kusakabe and M. Maruyama, *Phys. Rev. B* **67**, 092406 (2003).
- [37] G. Grosso and G. Pastori Parravicini, *Solid State Physics*, Academic Press (San Diego, London, 2003).
- [38] W. Liu, Z. F. Wang, Q. W. Shi, J. Yang, and F. Liu, *Phys. Rev. B* **80**, 233405 (2009).
- [39] S. Das Sarma, *American Scientist* **89**, 516, November-December 2001.
- [40] P. Giannozzi, *Metodi Numerici in Struttura Elettronica*, Lecture Notes.
- [41] P. Hohenberg and W. Kohn, *Phys. Rev. B* **136**, 864 (1964).
- [42] G. Seifert, D. Porezag, and Th. Frauenheim, *Int. J. of Quantum Chemistry* **58**, 185 (1995).
- [43] A. J. Cohen, *et al.*, *Science* **321**, 792 (2008).
- [44] P. Mori-Sánchez, A. J. Cohen, and W. Yang, *Phys. Rev. Lett.* **100**, 146401 (2008).
- [45] A. J. Cohen, P. Mori-Sánchez, and W. Yang, *Phys. Rev. B* **77**, 115123 (2008).
- [46] J. P. Perdew, K. Burke, and M. Ernzerhof, *Phys. Rev. Lett.* **77**, 3865 (1996).
- [47] W. Kohn, Y. Meir, and D. E. Makarov, *Phys. Rev. Lett* **80**, 4153 (1998).
- [48] M. Kamiya, T. Tsuneda, and K. Hirao, *J. Chem. Phys.* **117**, 6010 (2002).
- [49] V. I. Anisimov, F. Aryasetiawan, and A. I. Lichtenstein, *J. Phys.: Condens. Matter* **9**, 767 (1997).
- [50] J. P. Perdew, and A. Zunger, *Phys. Rev. B* **23**, 5048 (1981).
- [51] Y. Zhang, and W. Yang, *J. Chem. Phys.* **109**, 2604 (1998).
- [52] A. Seidl, A. Görling, P. Vogl, J. A. Majewski, and M. Levy, *Phys. Rev. B* **53**, 3764 (1996).
- [53] P. Giannozzi *et al.*, <http://www.quantum-espresso.org>.
- [54] A. Kokalj, *Comp. Mater. Sci.* **28**, 155 (2003). <http://www.xcrysden.org/>.
- [55] M. Lazzeri and F. Mauri, *Phys. Rev. Lett.* **90**, 036401 (2003).
- [56] D. Porezag and M. R. Pederson, *Phys. Rev. B* **54**, 7830 (1996).
- [57] A. Dal Corso, *Phys. Rev. B* **64**, 235118 (2001).

Ringraziamenti

Ringrazio il Dott. Nicola Manini per il suo aiuto, i suoi insegnamenti, le opportunità che mi ha offerto e la pazienza dimostrata durante il periodo che ho trascorso sotto la sua guida.

Ringrazio il Prof. Giovanni Onida per l'interesse espresso verso il mio progetto e per gli utili consigli.

Grazie ai Dott. Luca Ravagnan ed Eugenio Cinquanta per il tempo che mi hanno dedicato, per i preziosi suggerimenti ed il sostegno che hanno saputo darmi durante l'ultimo anno.

Grazie ai miei genitori, Ornella e Pietro, per il continuo supporto e sostegno in tutti questi anni di studio. Li ringrazio per essere sempre stati presenti, per aver sempre creduto in me e nelle mie scelte.

Grazie a mia sorella, Martina, per la sua presenza quotidiana, per la pazienza e per altre mille ragioni che un fratello maggiore non può elencare.

Grazie a tutti i parenti, partendo da nonna, zii e cugini, per l'affetto dimostrato nei miei confronti.

Grazie agli amici di lunga data, Cristina, Filippo, Roberto, Silvia e Sonia, per avermi saputo ascoltare, per il sostegno e per la loro amicizia.

Grazie ai miei compagni di allenamento, Andrea e Anisia, per la compagnia quasi quotidiana sulla pista saronnese.

Grazie ai compagni di corso, Carlotta, Daniele, Lorenzo, Nicola, e tutti gli altri che hanno condiviso con me questi ultimi anni.

Grazie a Olga, perchè aspetta sempre il tempo che ho da dedicarle.